

THIOKOL CHEMICAL CORPORATION
Huntsville Division
Huntsville, Alabama

FINAL REPORT

AN ANALYTICAL STUDY OF THE EFFECTS OF RADIAL ACCELERATION
UPON THE COMBUSTION MECHANISM OF SOLID PROPELLANT

Contract NAS7-406

Prepared For
Langley Research Center
National Aeronautics and Space Administration
Hampton, Virginia

Prepared By:

Robert L. Glick

R. L. Glick
Principal Investigator

Approved By:

G. F. Mangum

G. F. Mangum
Project Manager

B. D. Herbert

B. D. Herbert
Director
Project Management

Distribution of this report is provided in the interest of information exchange. Responsibility for the contents resides in the author or organization that prepared it.

Published
December 1966

TABLE OF CONTENTS

	<u>Page</u>
LIST OF FIGURES	iv
LIST OF TABLES	v
NOMENCLATURE	vi
SUMMARY	xiii
INTRODUCTION	1
ANALYSIS	5
Phase I - Internal Gas Dynamics	5
General	5
Swirling Flow in the Port of an Axisymmetric Grain	5
Swirling Flow in Converging-Diverging Nozzles	21
Equilibrium Ballistics at Fixed Time Computer Program	24
Phase II - Effect of Acceleration on Burning Rate	27
General	27
Metallized Propellants	27
Nonmetallized Propellants	33
RESULTS AND DISCUSSION	54
Phase I - Internal Gas Dynamics	54
Phase II - Effect of Acceleration on Burning Rate	54
Review of the Literature	54
Metallized Propellants	58
Nonmetallized Propellants	65
Comparison of Theory and Experiment	74
Metallized Propellants	74
Nonmetallized Propellants	78
CONCLUSIONS	85
RECOMMENDATIONS	87
LIST OF REFERENCES	88
APPENDIX A - EXPRESSIONS FOR $d\psi/\psi$ and $d\phi/\phi$	A-1
APPENDIX B - FLOW IN A CONICAL PIT	B-1
APPENDIX C - TYPICAL PROPERTIES OF NONMETALLIZED COMPOSITE PROPELLANTS	C-1

LIST OF FIGURES

<u>Figure</u>		<u>Page</u>
1	Effect of Spin on the Pressure-Time History of a Solid Propellant Rocket Motor (Reference 1)	2
2	Schematic Diagram Illustrating System	6
3	Schematic Diagram Illustrating Systems for Nozzle Analysis	22
4	Flow Diagram	26
5	Analytical Model for Particle Burning	31
6	Schematic Diagram Illustrating the Granular Diffusion Flame Model	35
7	Sketch Illustrating System Employed for Estimating the Pressure Difference Across the Gas Phase Reaction Zone	38
8	Sketch Illustrating the Deformation of a Spherical Fuel Vapor Pocket by a Velocity Gradient	43
9	Analytical Model for Fuel Vapor Pocket Deformation	45
10	Schematic Diagram of the Analytical Model	48
11	Assumed Effect of Acceleration on Burning Rate	55
12	Effect of Spin on Head End Pressure When $\pi r_0^2 \approx A^*$	56
13	Effect of Spin on Head End Pressure When $\pi r_0^2 \gg A^*$	57
14	Effect of Acceleration on the Burning Rate of Aluminized and Nonaluminized Composite Propellants (Reference 28)	59
15	Effects of Acceleration on the Burning Rate Constant and Pressure Exponent (Reference 31)	60
16	Effect of Normal Acceleration on Median Residue Size (Reference 31)	62
17	Residue Size Distribution (Data Reference 31)	63
18	Effect of Acceleration on the Burning Rate of a Metallized Composite Propellant (Reference 37)	64
19	Effect of Acceleration on the Burning Rate of a Polyurethane Propellant at 1000 psia (Reference 37)	67
20	Effect of Acceleration on the Burning Rate of a Polyurethane Propellant at 1500 psia (Reference 37)	68
21	Effect of Acceleration on the Burning Rate of PBAN Propellant at 500 psia (Reference 37)	69
22	Effect of Acceleration on the Burning Rate of PBAN Propellant at 1000 psia (Reference 37)	70
23	Effect of Acceleration on the Burning Rate of PBAN Propellant at 1500 psia (Reference 37)	71
24	Comparison of Burning Rate Data at 500, 1000, and 1500 psia (Reference 37)	72
25	Theoretical Results	74
26	Effect of β and Π on the Theoretical Results	76
27	Effect of Acceleration on the Burning Rate Coefficient and the Pressure Exponent	77
28	Effect of the Direction of Acceleration Force on the Maximum Burning Rate Ratio	79
29	Variation of Critical Angle with Maximum Burning Rate Ratio	80

LIST OF FIGURES (Continued)

<u>Figure</u>		<u>Page</u>
30	Comparison of Theory and Experiment for Nonmetallized Composite Propellant (Reference 37)	84
B-1	Schematic Diagram Illustrating Cone and Coordinate System	B-2
C-1	Thermodynamic Properties of the Products of Combustion of a Typical Propellant at 1000 psia	C-2
C-2	Thermodynamic Properties of Typical Fuel Vapors at 1000 psia	C-3
C-3	Thermodynamic Properties of Oxidizer Vapors at 1000 psia	C-4

LIST OF TABLES

<u>Table</u>		<u>Page</u>
I	Influence Coefficients for Swirling Flow	18
II	Influence Coefficients for One-Dimensional Flow	19
C-I	Typical Values for Thermophysical Properties	C-6

NOMENCLATURE

Latin Symbols

a	Acceleration
a_{cf}	Acceleration at which cellular flow is initiated between parallel plates
a_c	Acceleration that just retains a particle of mass median size on the burning surface
A	Area or frequency factor
A_i	Interaction area defined by Eq. (71) (Figure 5)
A_o	Cross-sectional area of the port of a solid propellant rocket motor
A_s	Area swept by a pit on the burning surface (Figure 5) and defined by Eq. (73)
A_{sm}	Area projected by the intersection of a pit and the mean burning surface (Figure 5)
c	Acoustic speed
c_p	Specific heat at constant pressure
c_0, c_1, \dots	Constants
C	Circumference of the port of a solid propellant rocket motor
C^*	Characteristic velocity
C_1, C_2, \dots	Constants
C_d	Drag coefficient
ΔC_v	Concentration difference
d_e	Nozzle exit diameter
d_{fv}	Characteristic dimension of a pocket of fuel vapor
d_{ox}	Mean diameter of oxidizer particles
d^*	Nozzle throat diameter
D	Diffusion coefficient

E	Activation energy
\dot{E}_r	Energy required to increase the burning rate above the base rate
\dot{E}_s	Energy supplied to the burning surface by metal combustion
f	Fraction of the metal additive that is burned at the surface; defined by Eq. (66)
F	Thrust
F_{1-D}	Thrust without swirl
G	Fraction of the metal additive on the sides of a pit that is agglomerated and burned; defined by Eq. (80)
G_{ij}	Influence coefficients
Gr_δ	Grashof number $a (\rho_s - \rho_f) \rho_g \delta_r^3 / \mu_g^2$
Gr_d	Grashof number $a \Delta \rho_g d_{fv}^3 / \mu_g^2$
h_D	Surface coefficient of mass transfer
h_v	Energy required to heat up and gasify the propellant
H	Total enthalpy
k_1, k_2	Constants
K	Swirl factor defined by Eq. (21a)
L	Length of the grain
m	Mass of a pocket of fuel vapor
\dot{m}	Mean rate of mass transfer from the pocket of fuel vapor to the oxidizer vapors or mass rate of flow
\dot{m}_{1-D}	Mass flow rate without swirl
M	Molecular weight
(MM)	Moment-of-Momentum
M_θ	Tangential Mach number V_θ / c_o
M_{rel}	Relative Mach number defined by Eq. (47)
M_z	Axial Mach number U / c_o

n	Pressure exponent of burning rate
N_s	Number of pits per unit area of the mean burning surface
p	Pressure
Pr	Prandtl number $c_p \mu / \lambda$
q_s''	Rate of heat transfer from the reacted gases to the burning surface
Q_M	Energy released to the burning surface by the combustion of a unit mass of metal
Q_s	Net heat release for gasification of the propellant
r	Radius
r_b	Burning rate
$(r_b)_{a=0}$	Burning rate when $a = 0$
r_{ba}	Rate of descent of an agglomerated metal particle through the propellant
r_c	Radius where $\rho = p = 0$
r_{cl}	Radial distance from the centerline of the motor to the centerline of a multiple nozzle (Figure 3)
r_o	Radius of the burning surface
R	Gas constant R_u/M
R_u	Universal gas constant
Re	Reynolds number $\rho_f V D / \mu_f$
Re_r	Radial Reynolds number $\rho V_r r / \mu$
Re_{rel}	Reynolds number $\rho_g V_{rel} d_{fv} / \mu_g$
Re_o	Reynolds number $\rho_p (r_b)_{a=0} d_{fv} / \mu_g$
Re_δ	Reynolds number $r_b \rho_p \delta_r / \mu_g$
s	Distance from the head end of the grain measured along the propellant surface
S	Relative horizontal displacement of idealized fuel vapor pocket

Sh	Sherwood number $h_D d_{fv}/D_g$
Sh ₀	Sherwood number when $a = 0$
Sc	Schmidt number $\mu/(\rho D)$
t	Temperature
T _f	Adiabatic flame temperature
u	Velocity component parallel to the burning surface
u'	Axial velocity perturbation because of end wall boundary layer effects
U	Uniform axial velocity
v	Velocity component normal to the burning surface
V	Free stream velocity
V _r	Radial velocity
V _{rel}	Relative velocity between the pocket of fuel vapor and the oxidizer vapors or relative velocity between the flow and the burning surface
V _θ	Tangential velocity
V _z	Axial velocity
V'	Axial velocity component of the injected gas
w _M	Mass fraction of metal additive in the propellant
x	Distance along the burning surface
X	Grain complexity factor $C/(4\pi A_c)$
y	Distance above the burning surface
z	Axial distance from the head end of the grain
z ₁ , z ₂	Constants

Greek Symbols

α	Burning rate coefficient
$(\alpha)_{a=0}$	Burning rate coefficient at static conditions
α^*	Swirl parameter defined by Eq. (53)

x

β	$(N_s \pi \xi_a^2)^{-1} \cos \Phi$
γ	Specific heat ratio
Γ_H	Function defined by Eq. (6)
δ_r	Thickness of gas phase reaction zone
δ_r'	Thickness of gas phase reaction zone in the low pressure limit
δ_r''	Thickness of the gas phase reaction zone in the high pressure limit
ϵ	Percent fuel vapor reacted or nozzle expansion ratio $(d_e/d^*)^2$
ζ	$\psi \gamma / \varphi - (\gamma - 1) (1 + g_\psi - g\varphi)$
η	Dimensionless distance from the burning surface y/δ_r and radius ratio $(r/r_o)^2$
η_c	$(r_c/r_o)^2$
θ_c	Semi-vertex angle of a conical pit in the burning surface
λ	Thermal conductivity
Λ	Volume of a fuel vapor pocket
μ	Dynamic viscosity
ξ	Length of idealized fuel vapor pocket (Figure 9)
ξ_a	Radius of the agglomerated metal particle
ξ_M'	Radius of a metal additive particle that is just retained on the burning surface by an acceleration a
ξ_{Mm}	Mass median radius of the metal additive particles
Ξ	Height of idealized fuel vapor pocket (Figure 9)
Π	$w_M \Delta H_c / (2 h_v)$
ρ	Density
$\Delta\rho$	Characteristic density difference between the fuel and oxidizer vapors
σ	Variance in a log-normal distribution
Σ	Minimum dimension of idealized fuel vapor pocket (Figure 9)

τ_{fv}	Lifetime of a pocket of fuel vapor
τ	Shear stress or time
ϕ	Function defined by Eq. (27)
Φ	Angle between the acceleration vector and the normal to the burning surface (Figure 5)
Φ_c	Angle at which $r_b / (r_b)_a = 0 = 1$
ψ	Function defined by Eq. (25)
ω	Rotation of idealized fuel vapor pocket (Figure 9)
Ω	Spin rate

Subscripts

f	Refers to the completely reacted gases
fv	Refers to the pocket of fuel vapor
i	Refers to initial conditions in the solid propellant or an index
j	An index
g	Refers to mean conditions in the gas phase reaction zone
M	Refers to the metal additive
o	Refers to conditions in the inviscid flow at $r = r_o$
p	Refers to the solid propellant or the agglomerated particle
s	Refers to the burning surface
t	Denotes stagnation conditions

Superscripts

+	Denotes a dimensionless quantity
*	Denotes conditions at the throat of the nozzle
\rightarrow	Denotes a vector

Special Symbols

O Denotes order of magnitude

Δ Denotes a small increment

dH $(H_s - H) d\dot{m}/\dot{m}$

dV_θ $(V_{\theta s} - V_{\theta o}) d\dot{m}/\dot{m}$

SUMMARY

Theoretical studies were made of the effect of spin on the internal ballistics at fixed time of rocket motors with axisymmetric grains and the effect of acceleration on the burning rate of metallized and nonmetallized composite propellants. In addition, the unclassified literature concerning the effects of acceleration on the burning rate of metallized and nonmetallized propellants was reviewed. In the internal ballistics studies a relatively general internal ballistics at fixed time computer program was written and the effects of spin on a single nozzle motor with a CP grain possessing inhibited ends were computed. The internal ballistics at fixed time computer program was based on the numerical integration along the port of influence coefficient equations for one-dimensional vortex flow developed in the study and an adaptation of Mager's results for swirling flow in nozzles. The numerical study showed that the major spin induced effects in single nozzle motors with CP grains possessing inhibited ends are attributable to acceleration induced burning rate changes and nozzle effects due to the swirling flow. In the burning rate studies a theoretical model based on particle burning was developed for metallized composite propellants, and a theoretical model based on the granular diffusion flame combustion model was developed for nonmetallized composite propellants. The trends predicted by the theoretical metallized propellant model relative to variations in burning rate coefficient and pressure exponent with acceleration and in burning rate with the direction of the acceleration force were in qualitative agreement with the experimental data. The theoretical model for nonmetallized composite propellant also showed qualitative agreement with the general trends in the experimental data where comparison was possible. However, a more detailed comparison with the data of Anderson showed important discrepancies. The causes of these discrepancies were not resolved.

AUTHOR

INTRODUCTION

In all rocket propelled vehicles, or missiles, a high degree of attitude stabilization must be achieved if the actual flight path is to closely approximate the flight path desired. At the present time, three methods of attitude stabilization are employed: spin stabilization, aerodynamic stabilization, and controlled stabilization. The first two methods are passive because neither attitude sensing nor control systems are required; the latter is an active system because these components are required.

It is well known that an appreciable fraction of the cost of a rocket propelled vehicle is attached to an attitude control system. Moreover, the inclusion of an attitude control system generally decreases the reliability and ruggedness of the vehicle and its payload capacity. Therefore, the use of passive attitude stabilization, when the generality offered by an active system is not required, is highly desirable from both economic and reliability standpoints.

The method of passive stabilization to be employed depends, to a large degree, upon both the characteristics and the flight path of the vehicle. For example, aerodynamic stabilization cannot be employed outside the sensible atmosphere because of the inability to generate aerodynamic forces of sufficient magnitude. Therefore, considerable interest resides with spin stabilization, and a number of rocket propelled vehicles currently employ this method of attitude stabilization.

However, numerous static spin tests¹ have demonstrated that the performance characteristics of a solid propellant rocket motor depend upon its spin rate.⁽¹⁻²³⁾ Figure 1 illustrates the variation of the pressure-time history for a solid propellant rocket motor with a CP grain configuration. The figure shows that the deviations from 0 rpm performance increase as the spin rate increases and that, in this case, the deviations are large; at 400 rpm, the peak pressure is approximately 66 percent greater than the 0 rpm value. Moreover, the deviations are not uniform throughout the burning period; the ignition phase is essentially unaffected, but the position of maximum pressure varies with the spin rate. Since high performance rocket motors must of necessity incorporate small factors of safety, it is seen that the failure to include spin effects in the design of a rocket motor could lead to motor failure.

The spin effects observed have been attributed to spin induced changes in the following: internal gas dynamics, combustion phenomena, metal/metal oxide retention, heat transfer, and deformation of the burning surface. Murphy and Wall⁽²⁴⁾ have analyzed the experimental data of Wall⁽²⁵⁾ and have shown that the latter factor is, at most, a secondary effect. Therefore, the remaining factors must control the magnitude of spin effects.

It is important to note that all of these effects are interrelated since (a) the burning rate depends upon the orientation of the burning surface, the local pressure, and the mass flux relative to the burning surface; (b) the internal gas dynamics depends

-
1. Static spin test is employed to denote a test where the vehicle, or rocket motor, is essentially fixed in space but rotating about its longitudinal axis of symmetry.

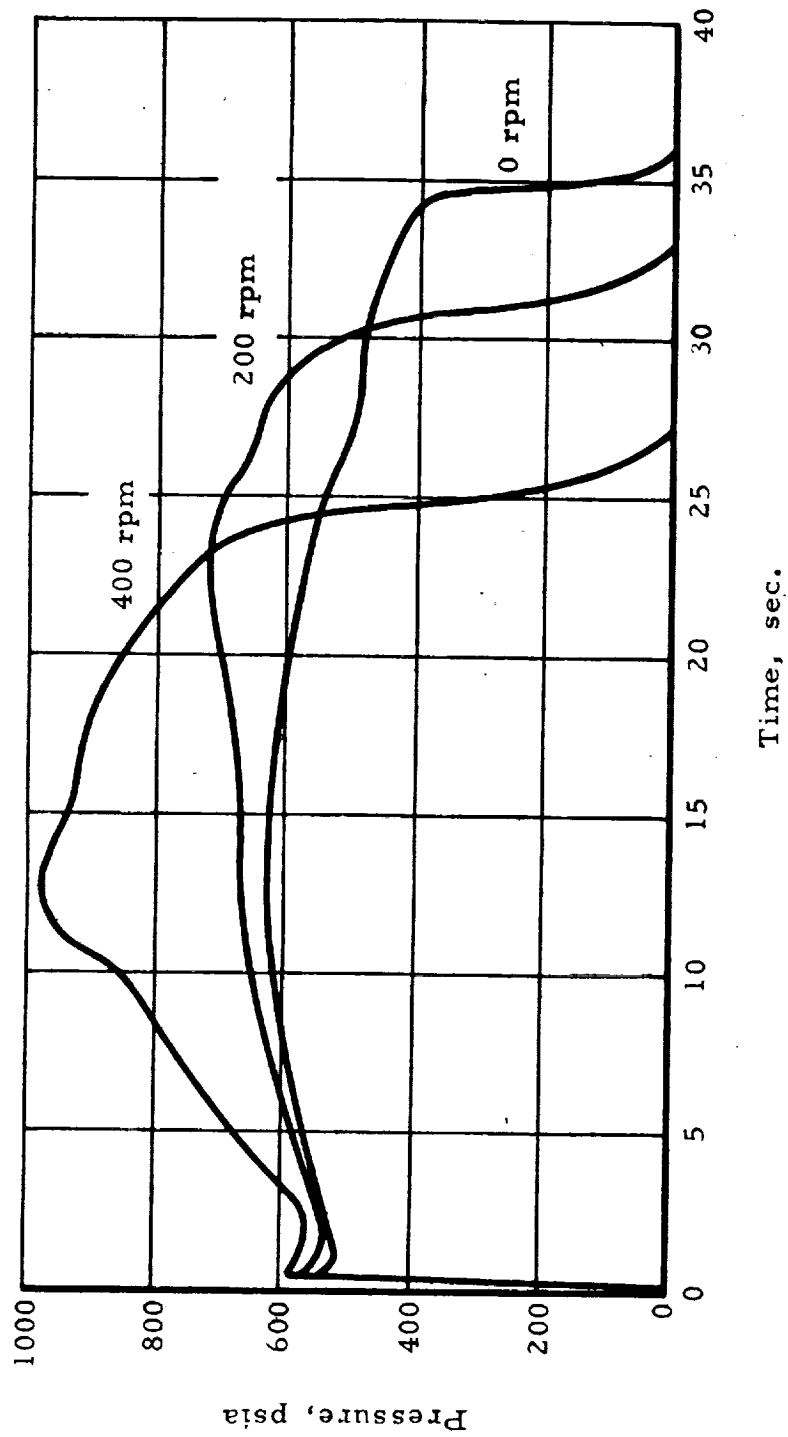


Figure 1. Effect of Spin on the Pressure-Time History of a Solid Propellant Rocket Motor (Reference 1)

upon the geometry of the burning surface, the local burning rate, and the mass discharge characteristics of the nozzle(s); (c) the retention of metal/metal oxide depends upon the geometry of the burning surface, the flow patterns within the motor, and the local burning rate; and (d) the heat transfer depends upon the flow patterns and metal/metal oxide retention. Since the hypothesized causes for the spin effects observed in motor tests are interrelated and since motor test data usually consist solely of over-all parameters (pressure and thrust-time histories), it is difficult if not impossible to determine the exact roles of the participating causes from the test data. Therefore, an understanding of spin effects must be founded on knowledge of the individual causes and their interplay.

It is also important to note that spin effects, in the main, lie outside the scope of conventional internal ballistics and grain analysis procedures. This precludes the analytical design as well as the analytical evaluation of rocket motors for spin applications, thereby constraining design and evaluation to trial and error procedures with prototype-sized motors--an expensive and time-consuming process.

In view of this state of affairs an analytical study program that was aimed at exploring spin-induced changes in the combustion processes of aluminized and nonaluminized composite propellants and spin-induced changes in the flow patterns in the port and nozzle(s) of rocket motors was proposed to the Langley Research Center of the National Aeronautics and Space Administration. This proposal led to the present program sponsored by NASA under Contract No. NAS7-406. The program was composed of two main phases:

- Phase I - Analytical study of the internal gas dynamics of cylindrically perforated grains.
- Phase II - Analytical study of the effects of radial acceleration upon the combustion mechanism of composite solid propellants.

In Phase I, attention was focused on the effects of Spin upon the flow patterns in the port and nozzle(s) of a rocket motor with a cylindrically perforated (CP) grain and the attendant effects upon motor performance.

The tasks to be performed in Phase I were as follows:

1. Derivation of the equations for flow in the port of a spinning rocket motor by integral methods.
2. Solution of equations derived under Task 1.
3. Combine solution of port equations with solution of nozzle equations.
4. Parametric study using above equations to determine influence of various parameters.

In Phase II, attention was focused on the combustion phenomenon itself, and the direct effect of acceleration upon the propellant burning rate was sought. Two cases were

examined: (a) nonaluminized composite propellants and (b) aluminized composite propellants. The tasks performed in Phase II were as follows:

1. Derivation and solution of equations for modified granular diffusion flame combustion model.
2. Derivation and solution of equations for particle burning.
3. Comparison with experimental data.

The above tasks have been completed; the remainder of this report describes the technical effort in detail.

ANALYSIS

PHASE I - INTERNAL GAS DYNAMICS

General

The objective of this phase was to develop an equilibrium ballistics-at-fixed-time computer program that would include spin effects. At equilibrium the operating point of the motor is established by the equality of the mass rate of gas generation through combustion and the mass rate of gas discharged through the nozzle. The characteristics of swirling flow through a converging-diverging nozzle had been previously studied by Mager.⁽²⁶⁾ Therefore, the nozzle aspects of the problem could be readily solved by adapting Mager's results to the conditions at hand. On the other hand, the flow field within the port was a considerably more difficult problem because no preliminary work had been performed. An exact analysis of this problem would have required, in the least, the numerical solution of two non-linear third order partial differential equations. In view of the time allowed and the introductory nature of the analysis, an approximate solution was sought instead. The approach taken was to find suitable approximations to the velocity profiles and then combine these profiles with the once integrated form of the equations of change. This yielded a system of coupled ordinary differential equations that could be numerically integrated along the port.

The discussion that follows concerns swirling flow in the port of an axisymmetric grain, swirling flow in converging-diverging nozzles, and the resulting equilibrium ballistics-at-fixed-time computer program.

Swirling Flow in the Port of an Axisymmetric Grain

Figure 2 shows the system under consideration and illustrates the coordinate system, the control surface, and the nomenclature employed. Conventional cylindrical coordinates are employed with r denoting the radius and z denoting the axial distance from the head end of the motor. The radius of the burning surface is r_0 and the radius of the throat is r_* . The components of velocity in the r , θ , and z directions are V_r , V_θ , and V_z , respectively, and s denotes the distance along the surface of the grain.

The first major question that arises is the importance of viscous effects. Experiments with vortex chambers⁽²⁷⁾ have shown that as long as the radial Reynolds number ($Re_r = \rho V_r r / \mu$) is greater than 5, viscous effects are negligible. The order of magnitude of the radial Reynolds number is readily estimated since $O(\rho V_r) = r_b \rho_p$.¹ Thus, the order of magnitude of the radial Reynolds number is

$$O(Re_r) = r_b \rho_p r_0 / \mu \quad (1)$$

Typical values for the terms in Eq. (1) are as follows: $r_b \approx 0.3$ in/sec; $\rho_p \approx 0.064$ lb/in³; $r_0 \approx 1$ in.; and $\mu \approx 3.8 \times 10^{-6}$ lb/in-sec. Therefore, the order of magnitude of Re_r in a typical rocket motor is about 500. Since this value is approximately 100 times the aforementioned critical value, it may be concluded that, except for the region

1. Symbols are defined in the Nomenclature.

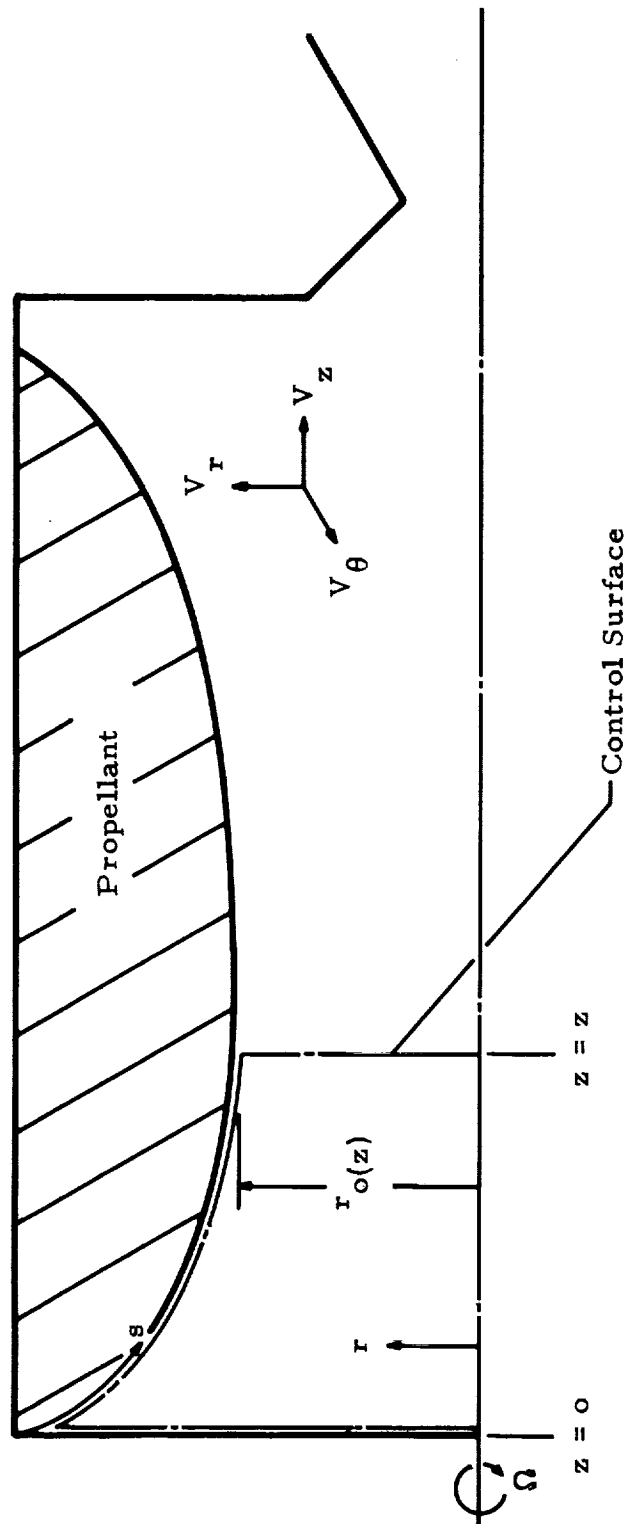


Figure 2: Schematic Diagram Illustrating System.

very near to the axis of rotation, viscous effects are negligible. This same conclusion was reached by Reference 28 although a different approach was employed. In that case solutions for viscous, incompressible vortex flow were examined under conditions compatible with those inside a rocket motor.

Since viscous effects will be small, it was assumed that the flow was inviscid. In addition to this assumption it was also assumed that the flow was steady, axisymmetric, and adiabatic, and that the fluid was a perfect gas with constant specific heats and molecular weight. With these assumptions the equations of change for the volume bounded by the control surface illustrated on Figure 2 became:

$$\text{Continuity} \quad \oint \rho \vec{V} \cdot d\vec{A} = 0 \quad (2a)$$

$$\text{Energy} \quad \oint \rho H \vec{V} \cdot d\vec{A} = 0 \quad (2b)$$

$$\text{Axial Momentum} \quad \oint \rho V_z \vec{V} \cdot d\vec{A} + \oint p dA_x = 0 \quad (2c)$$

$$\text{Axial Moment of Momentum} \quad \oint \rho r V_\theta \vec{V} \cdot d\vec{A} = 0 \quad (2d)$$

By performing the indicated integrations over the control surface and then differentiating those expressions with respect to z , Eqs. (2) were expanded to the following:

$$\frac{d}{dz} \left[2\pi \int_0^{r_o(z)} \rho V_z r dr \right] = d\dot{m} \quad (3a)$$

$$\frac{d}{dz} \left[2\pi \int_0^{r_o(z)} \rho H V_z r dr \right] = H'_s d\dot{m} \quad (3b)$$

$$\frac{d}{dz} \left[2\pi \int_0^{r_o(z)} p r dr \right] + \frac{d}{dz} \left[2\pi \int_0^{r_o(z)} \rho V_z^2 r dr \right] - p_o dA_o - V' d\dot{m} = 0 \quad (3c)$$

$$\frac{d}{dz} \left[2\pi \int_0^{r_o(z)} \rho V_z V_\theta r^2 dr \right] = r_o V_{\theta s} d\dot{m} \quad (3d)$$

To complete the transformation of the equations of change to a set of simultaneous ordinary differential equations, approximate expressions for the radial variation of density, pressure, axial velocity, tangential velocity, and total enthalpy must be chosen

so that the integrals in Eqs. (3) can be evaluated. Insight into the nature of the functions required was gleaned from the inviscid equations of motion. These equations in non-dimensional form are as follows:

$$\rho^+ \left[V_r^+ \frac{\partial V_r^+}{\partial r^+} + V_z^+ \frac{\partial V_r^+}{\partial z^+} - \frac{V_\theta^{+2}}{r^+} \right] = - \frac{\partial p^+}{\partial r^+} \quad (4a)$$

$$V_r^+ \frac{\partial V_\theta^+}{\partial r^+} + V_z^+ \frac{\partial V_\theta^+}{\partial z^+} + \frac{V_r^+ V_\theta^+}{r^+} = 0 \quad (4b)$$

$$\rho^+ \left[V_r^+ \frac{\partial V_z^+}{\partial r^+} + V_z^+ \frac{\partial V_z^+}{\partial z^+} \right] = - \frac{\partial p^+}{\partial z^+} \quad (4c)$$

Interest lies primarily in the regions where spin effects may be appreciable. Therefore, the spin rate will also be appreciable and the tangential velocity of the gas at the burning surface will be large. Moreover, the analysis will be restricted to motors with large length-to-diameter ratios. Therefore, the order of magnitude of the following nondimensional terms can be established: $O(z^+) = 1/\delta$; $O(r^+) = 1$; $O(V_\theta^+) = 1$; $O(V_z^+) = 1$; $O(V_r^+) = \delta$ where $O(\delta) < 1$. If these orders of magnitude are employed for the values in Eqs. (4)¹, and the terms of lower order neglected, Eqs. (4a) and (4c) reduce to

$$\frac{V_\theta^{+2}}{r^+} = \frac{1}{\rho^+} \frac{\partial p^+}{\partial r^+} \approx O(1) \quad (5a)$$

$$\frac{1}{\rho^+} \frac{\partial p^+}{\partial z^+} \approx O(\delta) \quad (5b)$$

while Eq. (4b) is unchanged. However, the order of magnitude of the individual terms in Eq. (4b) is δ .

Eqs. (5) show two important results: (1) the tangential velocity field controls the radial pressure gradient, and (2) the radial pressure gradient is much larger than the

$$1. \quad O \left(\frac{\partial V_\theta^+}{\partial r^+} \right) = \frac{O(V_\theta^+)}{O(r^+)} = 1; \text{ etc.}$$

axial pressure gradient $\left[O \left(\frac{\partial p^+}{\partial r^+} \right) > O \left(\frac{\partial p^+}{\partial z^+} \right) \right]$. The first result enables computation of the radial pressure variation from the tangential velocity field. The second result has broader significance since it implies that, to an approximation of order δ , axial pressure gradients are negligible when compared with radial pressure gradients. Therefore, to a first approximation the static pressure could be taken as independent of axial distance.

The radius of the burning surface may vary with distance from the head end of the motor $[r_0 = f(z)]$; therefore, the kinetic energy of the combustion gas may also vary from point to point on the burning surface. However, the flame temperature (and static enthalpy) will not vary over the burning surface and the preceding analysis has indicated that to a first approximation the static pressure can be considered constant over the burning surface. The question is, "How important are the kinetic energy changes?" This question can be answered, in part, by examining the ratio of the kinetic energy of the gas at the burning surface to the flame enthalpy since this ratio is representative of the importance of the kinetic energy to the whole. This ratio is

$$\Gamma_H = \frac{(r_0 \Omega)^2}{2 c_p T_f} \quad (6)$$

From structural considerations based on turbine practice $O(r_0 \Omega) = 1000$ ft/sec, and based on current solid propellants $O(T_f) = 6000^\circ\text{R}$ and $O(c_p) = 0.6$ B/lb_m-R. Therefore, $O(\Gamma_H) = 0.006$. The pressure change due to this kinetic energy (velocity head) can also be determined since for small changes

$$\frac{dp}{p} = \frac{\gamma}{\gamma-1} \frac{dt}{t} \approx \frac{\gamma}{\gamma-1} \Gamma_H \quad (7)$$

Thus, since $\gamma \approx 1.2$ for solid propellant gases, $O(dp/p) = 0.036$. These results show that pressure and total enthalpy changes due to the kinetic energy of the combustion gases at the burning surface are small. When these results are combined with the previous results, it is seen that to a first approximation both the total pressure and the total enthalpy are the same for each streamline in the flow field. In other words, the flow field is nearly isentropic. This implies that first approximations for the required velocity, enthalpy, pressure and density profiles may be obtained from potential flow results.

It is interesting to note that the streamlines with the highest total pressure originate near the head end of the motor. However (in the flow field), these streamlines lie at the smaller radii where viscous effects (which will reduce their total pressure) are most severe. Therefore, real fluid effects tend in some ways to force the physical system toward the idealized system assumed.

For a potential flow $\text{curl } \vec{V} = 0$ so that in an axisymmetric flow field

$$\partial_z (r V_\theta) = 0 \quad (8a)$$

$$\frac{\partial V_r}{\partial z} = \frac{\partial V_z}{\partial r} \quad (8b)$$

$$\frac{\partial (r V_\theta)}{\partial r} = 0 \quad (8c)$$

Integration of Eq. (8a) shows that

$$r V_\theta = K(r) \quad (9)$$

but Eq. (8c) shows that $K(r) = \text{constant}$ so that

$$V_\theta = K/r \quad (10)$$

Eq. (8b) in nondimensional form is

$$\frac{\partial V_r^+}{\partial z^+} = \frac{\partial V_z^+}{\partial r^+} \quad (11)$$

Integrating Eq. (11) from the burning surface inward gives

$$V_z^+ = \int_1^{r^+} \frac{\partial V_r^+}{\partial z^+} dr^+ + V_z^+(1, z^+) \quad (12)$$

From the previous order of magnitude results $O\left(\frac{\partial V_r^+}{\partial z^+}\right) = \delta^2$. Therefore, from this result and Eq. (12)

$$V_z^+ \approx V_z^+(1, z^+) + O\left[\delta^2 (1 - r^+)\right] \quad (13)$$

Since r^+ is less than or equal to unity and $O(V_z^+) = 1$, it is seen that the axial velocity is essentially constant across the port. Accordingly, it was assumed that

$$V_z \approx V_z(r_0, z) = U(z) \quad (14)$$

The fact that the flow field is isentropic to a first approximation also implies that

$$p \approx C \rho^\gamma \quad (15)$$

Therefore, the radial pressure and density distribution can be determined by integrating Eq. (5a) using Eqs. (10) and (15). This yields

$$p \cong p_o \left[1 - \frac{\gamma-1}{2} M_\theta^2 \left[\left(\frac{r_o}{r} \right)^2 - 1 \right] \right]^{\frac{\gamma}{\gamma-1}} \quad (16)$$

$$\rho \cong \rho_o \left[1 - \frac{\gamma-1}{2} M_\theta^2 \left[\left(\frac{r_o}{r} \right)^2 - 1 \right] \right]^{\frac{\gamma-1}{\gamma}} \quad (17)$$

where $M_\theta = K/(r_o c_o)$.

Equations (16) and (17) show that at some finite radius r_c density and pressure vanish and that for $r < r_c$ both density and pressure become negative. Therefore, only the flow in the region $r_c \leq r \leq r_o$ can have physical significance and the lower limit of integration on Eqs. (3) must be changed to r_c . The critical radius r_c can be determined by equating either Eq. (16) or Eq. (17) to zero and solving for r . This yields

$$r_c = r_o \left[\frac{\frac{\gamma-1}{2} M_\theta^2}{1 + \frac{\gamma-1}{2} M_\theta^2} \right]^{1/2} \quad (18)$$

In the actual problem the axial variations of the variables are being sought. Therefore, it will be assumed that the flow field at any axial station is isentropic. This is in agreement with the order of magnitude analysis and the physical problem. It will further be assumed that the profiles represented by Eqs. (10), (16), and (17) express the radial variations of the respective functions and that the axial variations in tangential velocity, static pressure, and static density, can be obtained by assuming that K , p_o , and ρ_o are functions of axial distance. In addition it will be assumed that the axial velocity can be represented by

$$V_z(r, z) = U(z) + u'(r, z) \quad (19)$$

and that the total enthalpy is a function of axial distance only. The function $u'(r, z)$ in Eq. (19) is included to account for effects due to the boundary layer at the head end of the motor.

It is convenient to define as a new variable $\eta = (r/r_o)^2$. With this variable the common bracketed term of Eqs. (16) and (17) can be written as

$$\left[1 - \frac{\gamma-1}{2} M_\theta^2 \left[\left(\frac{r_o}{r} \right)^2 - 1 \right] \right] = 1 - \frac{\eta_c}{1 - \eta_c} \frac{1 - \eta}{\eta} = f(\eta, \eta_c) \quad (20)$$

where $\eta_c = (r_c/r_o)^2$.

The above results may be summarized by stating the functions to be employed to evaluate the integrals in Eqs. (3)

$$V_{\theta} = K(z)/r \quad (21a)$$

$$V_z = U(z) + u'(r, z) \quad (21b)$$

$$p = p_0(z) \left[f(\eta, \eta_c) \right]^{\frac{\gamma}{\gamma-1}} \quad (21c)$$

$$\rho = \rho_0(z) \left[f(\eta, \eta_c) \right]^{\frac{1}{\gamma-1}} \quad (21d)$$

$$H = H(z) \quad (21e)$$

Examination of Eqs. (3) shows that five different integrals must be evaluated using Eqs. (21) in order to complete the reduction of the equations of change to ordinary differential equations.

The first integral is

$$2\pi \int_0^{r_0} \rho V_z r dr = A_0 \rho_0 U \int_{\eta_c}^1 \left[f(\eta, \eta_c) \right]^{\frac{1}{\gamma-1}} d\eta + 2\pi \int_0^{r_0} \rho u' r dr \quad (22)$$

The two functions on the right hand side of Eq. (22) can be interpreted to be the mass flow due to mean flow and the mass flow due to perturbations introduced by the end wall boundary layers. With this interpretation

$$2\pi \int_0^{r_0} \rho u' r dr = 0 \quad (23)$$

because a nonzero result would imply net mass transport across the end wall boundary layer. Since the flow field has been assumed to be steady, net mass generation within the end wall boundary layer is impossible. Thus, Eq. (22) becomes

$$2\pi \int_0^{r_0} \rho V_z r dr = A_0 \rho_0 U \psi \quad (24)$$

where the function ψ is defined as

$$\psi = \int_{\eta_c}^1 \left[f(\eta, \eta_c) \right]^{\frac{1}{\gamma-1}} d\eta \quad (25)$$

The second integral is

$$2 \pi \int_0^{r_0} p r dr = A_0 p_0 \int_{\eta_c}^1 \left[f(\eta, \eta_c) \right]^{\frac{1}{\gamma-1}} d\eta = A_0 p_0 \varphi \quad (26)$$

where the function φ is defined as

$$\varphi = \int_{\eta_c}^1 \left[f(\eta, \eta_c) \right]^{\frac{\gamma}{\gamma-1}} d\eta \quad (27)$$

The third integral is

$$2 \pi \int_0^{r_0} \rho V_z^2 r dr = A_0 \rho_0 U^2 \int_{\eta_c}^1 \left[f(\eta, \eta_c) \right]^{\frac{1}{\gamma-1}} d\eta + 4 \pi U \int_0^{r_0} \rho u' r dr + \quad (28)$$

$$+ 2 \pi \int_0^{r_0} \rho (u')^2 r dr$$

Eq. (23) shows that the second term is zero. Therefore, Eq. (28) reduces to

$$2 \pi \int_0^{r_0} \rho V_z^2 r dr = A_0 \rho_0 U^2 \psi + 2 \pi \int_0^{r_0} \rho (u')^2 r dr \quad (29)$$

The first term on the right hand side of Eq. (29) is the axial momentum due to the mean flow while the second term is the axial momentum due to the boundary layer flow. The latter momentum is created by viscous effects in the end wall boundary layer. The problem now is how does this momentum flow change along the port. Clearly, analytical games could be played by choosing different variations, but how could the correct variation be established? Accordingly, a variation that seems physically plausible and offers analytical advantages will be chosen; therefore, choose¹

$$2 \pi \int_0^{r_0} \rho (u')^2 r dr = \text{constant} \quad (30)$$

The fourth integral is

$$2 \pi \int_0^{r_0} \rho H V_z r dr = A_0 \rho_0 U H \int_{\eta_c}^1 \left[f(\eta, \eta_c) \right]^{\frac{1}{\gamma-1}} d\eta + 2 \pi H \int_0^{r_0} \rho u' r dr \quad (31)$$

-
1. Only the change of axial momentum appears in the equations of change; therefore, this choice eliminates the end wall effects from the equations.

Eq. (23) shows that the second term is zero. Therefore, Eq. (31) becomes

$$2 \pi \int_0^{r_0} \rho H V_z r dr = A_0 \rho_0 U H \psi \quad (32)$$

The fifth integral is

$$2 \pi \int_0^{r_0} \rho V_\theta V_z r^2 dr = A_0 \rho_0 U K \int_{\eta_c}^1 \left[f(\eta, \eta_c) \right]^{\frac{1}{\gamma-1}} d\eta + 2 \pi K \int_0^{r_0} \rho u' dr \quad (33)$$

Eq. (23) shows that the second term is zero. Therefore, Eq. (33) reduces to

$$2 \pi \int_0^{r_0} \rho V_\theta V_z r^2 dr = A_0 \rho_0 U K \psi \quad (34)$$

The ordinary differential form desired for the equations of change may now be obtained by substituting Eqs. (24), (26), (29), (32), and (34) into Eqs. (3). This yields

$$d[A_0 \rho_0 U \psi] = d\dot{m} \quad (35a)$$

$$d[p_0 A_0 \phi] + d[A_0 \rho_0 U^2 \psi] - p_0 dA_0 - V' d\dot{m} = 0 \quad (35b)$$

$$d[A_0 \rho_0 U H \psi] = H_s d\dot{m} \quad (35c)$$

$$d[A_0 \rho_0 U K \psi] = r_0 V_{\theta s} d\dot{m} \quad (35d)$$

Eqs. (35) together with the equation of state

$$\rho_0 = \rho_0 R t_0 \quad (36)$$

the supplementary equation

$$H = c_p t_0 \left[1 + \frac{\gamma-1}{2} (M_z^2 + M_\theta^2) \right] \quad (37)$$

where

$$M_z = U/c_o \quad (38)$$

and the equations defining η_c , ϕ , and ψ give a sufficient number of equations to define the dependent variables along the port.

The nonlinearity of the equations and the general nature of the boundary conditions preclude an analytical solution. Therefore, a numerical procedure to solve the equations was sought. The procedure employed parallels a successful procedure currently employed at Thiokol for one-dimensional flow problems. This procedure uses a Runge-Kutta numerical integration technique to perform a forward integration of the equation for dM_z^2/M_z^2 from the head end to the aft end of the grain. To employ this procedure Eqs. (35) must be put into influence coefficient form. Equations (35) were first transformed into the dimensionless form

$$\frac{dA_o}{A_o} + \frac{dU}{U} + \frac{d\rho_o}{\rho_o} + \frac{d\psi}{\psi} = \frac{d\dot{m}}{\dot{m}} \quad (39a)$$

$$\left(1 - \frac{1}{\phi}\right) \frac{dA_o}{A_o} + \gamma \frac{\psi}{\phi} M_z^2 \frac{dU}{U} + \frac{dp_o}{p_o} + \frac{d\Phi}{\Phi} + \gamma \frac{\psi}{\phi} M_z^2 \frac{d\dot{m}}{\dot{m}} + \quad (39b)$$

$$+ \frac{\gamma}{2} \frac{\psi}{\phi} M_z^2 \left(-2 \frac{V'}{U} \frac{d\dot{m}}{\dot{m}} \right) = 0$$

$$\frac{dH}{c_p t_o} = \frac{d\bar{H}}{c_p t_o} \quad (39c)$$

$$\frac{dV_{\theta o}}{V_{\theta o}} = \frac{d\bar{V}_{\theta}}{V_{\theta o}} - \frac{1}{2} \frac{dA_o}{A_o} \quad (39d)$$

where

$$\frac{d\bar{H}}{c_p t_o} = \frac{H_s - H}{c_p t_o} \frac{d\dot{m}}{\dot{m}} \quad (39e)$$

and

$$\frac{d\bar{V}_\theta}{V_{\theta o}} = \frac{V_{\theta s} - V_{\theta o}}{V_{\theta o}} \frac{d\dot{m}}{\dot{m}} \quad (39f)$$

In addition to these equations the following were derived¹ from the definitions of M_z , M_θ , φ , and ψ :

$$\frac{dM_z^2}{M_z^2} = 2 \frac{dU}{U} - \frac{dt_o}{t_o} \quad (40)$$

$$\frac{dM_\theta^2}{M_\theta^2} = 2 \frac{dK}{K} - \frac{dA_o}{A_o} - \frac{dt_o}{t_o} \quad (41)$$

$$\frac{d\varphi}{\varphi} = g_\varphi \frac{dM_\theta^2}{M_\theta^2} \quad (42)$$

$$\frac{d\psi}{\psi} = g_\psi \frac{dM_\theta^2}{M_\theta^2} \quad (43)$$

Also, from the equation of state and Eq. (37)

$$\frac{dp_o}{p_o} = \frac{d\rho_o}{\rho_o} + \frac{dt_o}{t_o} \quad (44)$$

1. The derivation of Eqs. (42) and (43) is presented in Appendix I.

and

$$\begin{aligned} \frac{dH}{H} = & \frac{\frac{\gamma-1}{2} M_z^2}{1 + \frac{\gamma-1}{2} (M_z^2 + M_\theta^2)} \frac{dM_z^2}{M_z^2} + \frac{\frac{\gamma-1}{2} M_\theta^2}{1 + \frac{\gamma-1}{2} (M_z^2 + M_\theta^2)} \frac{dM_\theta^2}{M_\theta^2} + \\ & + \frac{dt_o}{t_o} \end{aligned} \quad (45)$$

Examination of Eqs. (39a - 45) shows that there are 15 variables and 10 equations. Therefore, choose 5 of the variables, that can be specified, to be independent variables; the remaining 10 are to be treated as dependent variables. The independent variables are dA_o/A_o , $d\dot{m}/\dot{m}$, $-2V'd\dot{m}/(U\dot{m})$, $d\bar{H}/(c_p t_o)$, and $d\bar{V}/V_{\theta o}$. The only dependent variables that need to be expressed in terms of the independent variables are dM_z^2/M_z^2 , dM_θ^2/M_θ^2 , dt_o/t_o , and dp_o/p_o since the other dependent variables can be expressed in terms of these variables by algebraic relationships.

The required algebraic manipulations were performed, and Table I presents the influence coefficients for swirling flow while Table II presents the same influence coefficients for one-dimensional flow. (29) Since $g_\psi = g_\phi = 0$ and $\psi = \phi = 1$ when $M_\theta = 0$, it is seen that the swirling flow influence coefficients have the correct limiting form as M_θ approaches zero. It is interesting to note that the function ζ is always greater than or equal to one; therefore, a swirling flow "chokes" at an axial Mach number that is less than one.

The differential equations describing the flow in the port of a spinning rocket motor were written in terms of the influence coefficients as¹

$$\frac{dM_z^2}{ds} = M_z^2 \left[\left(G_{11} + G_{13} \frac{H_s - H}{c_p t_o} + G_{14} \frac{V_{\theta s} - V_{\theta o}}{V_{\theta o}} \right) \frac{2\pi r_o r_b}{\dot{m}} + \frac{G_{15}}{A_o} \frac{dA_o}{ds} \right] \quad (46a)$$

$$\frac{dM_\theta^2}{ds} = M_\theta^2 \left[\left(G_{21} + G_{23} \frac{H_s - H}{c_p t_o} + G_{24} \frac{V_{\theta s} - V_{\theta o}}{V_{\theta o}} \right) \frac{2\pi r_o r_b}{\dot{m}} + \frac{G_{25}}{A_o} \frac{dA_o}{ds} \right] \quad (46b)$$

1. The effect of the axial momentum carried by the injected mass is usually neglected in internal ballistics calculations because its effect is small; it was neglected here. G_{ij} refers to the various influence coefficients in Table I, i.e. $G_{23} = (\psi \gamma M_z^2 / \phi - 1) / (1 - M_z^2 \zeta)$

TABLE I
INFLUENCE COEFFICIENTS FOR SWIRLING FLOW

j →	Independent Variable →				
		1	2	3	4
↓	Dependent Variable ↓	$\frac{d\dot{m}}{\dot{m}}$	$2\gamma \frac{d\dot{m}}{\dot{m}}$	$\frac{dH}{C_p O}$	$\frac{d\bar{V}_\theta}{V_{\theta 0}}$
		$\frac{dM_\theta^2}{M_\theta^2}$	$\frac{dM_z^2}{M_z^2}$	$\frac{d\bar{V}_\theta}{V_{\theta 0}}$	$\frac{d\bar{V}_\theta}{V_{\theta 0}}$
1	$\frac{dM_\theta^2}{M_\theta^2}$	$\frac{\gamma-1}{2} \frac{M_\theta^2}{1 + \frac{\gamma}{2} M_\theta^2} (1 + \frac{\gamma}{2} M_\theta^2)$	$\frac{\gamma-1}{2} \frac{M_z^2}{1 + \frac{\gamma}{2} M_z^2} (1 + \frac{\gamma}{2} M_z^2)$	$\frac{1 + \frac{\gamma}{2} M_z^2}{1 - M_z^2} + \frac{2 \left[\frac{\gamma-1}{2} M_\theta^2 (1 + \frac{\gamma}{2} M_\theta^2) - \frac{2}{\phi} (1 + \frac{\gamma-1}{2} M_z^2) \right] (g_\psi - g_\phi)}{1 - M_z^2}$	$\frac{(\gamma-1) M_\theta^2 (1 + \frac{\gamma}{2} M_\theta^2) + \frac{4 \left[1 + \frac{\gamma-1}{2} (M_z^2 + M_\theta^2) \right] (g_\psi - g_\phi)}{1 - M_z^2}}{1 - M_z^2}$
2	$\frac{dM_\theta^2}{M_\theta^2}$	$\frac{(\gamma-1) M_\theta^2 (1 + \frac{\gamma}{2} M_\theta^2)}{1 - M_z^2}$	$\frac{\gamma \frac{\gamma-1}{2} \frac{M_z^4}{M_z^2}}{1 - M_z^2}$	$\frac{\frac{\gamma}{\phi} \gamma M_z^2 - 1}{1 - M_z^2}$	$\frac{2 \left[(\gamma-1) M_\theta^2 + (1 + \frac{\gamma-1}{2} M_\theta^2) (1 - \frac{\gamma}{\phi} M_z^2) \right]}{1 - M_z^2}$
3	$\frac{dP_0}{P_0}$	$\frac{-2 \frac{\gamma}{\phi} \gamma M_\theta^2 (1 + \frac{\gamma-1}{2} M_\theta^2)}{1 - M_z^2} + \frac{\frac{\gamma}{\phi} \gamma M_z^2 (1 + g_\psi)}{1 - M_z^2}$	$\frac{\frac{\gamma}{\phi} \gamma M_z^2 (1 + g_\psi)}{1 - M_z^2}$	$\frac{g_\phi - \frac{\gamma}{\phi} \gamma M_z^2 (1 + g_\psi)}{1 - M_z^2}$	$\frac{2 (1 + \frac{\gamma-1}{2} M_\theta^2) (\frac{\gamma}{\phi} \gamma M_z^2 g_\psi - g_\phi) + \frac{\frac{\gamma}{\phi} \gamma M_\theta^2 (1 - \frac{\gamma-1}{2} M_\theta^2) + \frac{\phi+1}{\phi} (\gamma-1) M_z^2 g_\phi}{1 - M_z^2}}{1 - M_z^2}$
4	$\frac{dt_0}{t_0}$	$\frac{(\gamma-1) M_\theta^2 (1 + \frac{\gamma}{2} M_\theta^2)}{1 - M_z^2}$	$\frac{-\gamma \frac{\gamma-1}{2} \frac{M_z^4}{M_z^2}}{1 - M_z^2}$	$\frac{1 - \frac{\gamma}{\phi} \gamma M_z^2}{1 - M_z^2}$	$\frac{(\gamma-1) \left[M_\theta^2 (1 - \frac{\gamma}{\phi} \gamma M_\theta^2) / 2 + M_z^2 (1/\phi - g_\psi + g_\phi) \right]}{1 - M_z^2}$

$$\zeta = \frac{\gamma}{\phi} \gamma - (\gamma-1) (1 + g_\psi - g_\phi)$$

TABLE II
INFLUENCE COEFFICIENTS FOR ONE-DIMENSIONAL FLOW

Independent Variable ↓	→ Dependent Variable	$\frac{d\dot{m}}{\dot{m}}$	$-2\gamma \frac{d\dot{m}}{\dot{m}}$	$\frac{d\bar{H}}{C_t p_0}$	$\frac{dA_0}{A_0}$
$\frac{dM_z}{M_z}$	$\frac{2(1+\gamma M_z^2)(1+\frac{\gamma-1}{2}M_z^2)}{1-M_z^2}$	$\frac{\gamma M_z^2(1+\frac{\gamma-1}{2}M_z^2)}{1-M_z^2}$	$\frac{1+\gamma M_z^2}{1-M_z^2}$	$-\frac{2(1+\frac{\gamma-1}{2}M_z^2)}{1-M_z^2}$	
$\frac{dp_0}{p_0}$	$-\frac{2\gamma M_z^2(1+\frac{\gamma-1}{2}M_z^2)}{1-M_z^2}$	$\frac{\gamma M_z^2[1+(\gamma-1)M_z^2]/2}{1-M_z^2}$	$-\frac{\gamma M_z^2}{1-M_z^2}$	$\frac{\gamma M_z^2}{1-M_z^2}$	
$\frac{dt_0}{t_0}$	$-\frac{(\gamma-1)M_z^2(1+\gamma M_z^2)}{1-M_z^2}$	$-\frac{\gamma(\gamma-1)M_z^4/2}{1-M_z^2}$	$\frac{1-\gamma M_z^2}{1-M_z^2}$	$\frac{(\gamma-1)M_z^2}{1-M_z^2}$	

$$\frac{dp_o}{ds} = p_o \left[G_{31} + G_{33} \frac{H_s - H}{c_p t_o} + G_{34} \frac{V_{\theta s} - V_{\theta o}}{V_{\theta o}} \right] \frac{2\pi r_o r_b}{\dot{m}} + \frac{G_{45}}{A_o} \frac{dA_o}{ds} \quad (46c)$$

$$\frac{dt_o}{ds} = t_o \left[G_{41} + G_{43} \frac{H_s - H}{c_p t_o} + G_{44} \frac{V_{\theta s} - V_{\theta o}}{V_{\theta o}} \right] \frac{2\pi r_o r_b}{\dot{m}} + \frac{G_{35}}{A_o} \frac{dA_o}{ds} \quad (46d)$$

$$\frac{d\dot{m}}{ds} = 2\pi r_o r_b \quad (46e)$$

Distance along the burning surface was employed as the independent variable because it is continuous and monotonically increasing. The burning rate was assumed to be related to the flow field variables by the equation

$$r_b = \alpha_t p_o^n \left[1 + k_1 (p_o M_{rel})^{k_2} \right] \quad (47)$$

where α_t , n , k_1 , and k_2 are constants and the Mach number of the flow relative to the rotating surface is

$$M_{rel} = \left[U^2 + [V_{\theta o} - (r_o \Omega)]^2 \right]^{1/2} / c_o \quad (48)$$

The velocity components required in Eq. (48) were determined from the Mach numbers and the static temperature

$$U = \left[M_z^2 (\gamma R t_o) \right]^{1/2} \quad (49)$$

$$V_{\theta o} = \left[M_{\theta}^2 (\gamma R t_o) \right]^{1/2} \quad (50)$$

The initial conditions for Eqs. (46) are

$$M_z^2 = \dot{m} = 0 \quad (51a)$$

$$t_o = t_f \quad (51b)$$

$$p_o = p' \quad (51c)$$

$$M_{\theta}^2 = (r_o \Omega)^2 / (\gamma R t_f) \quad (51d)$$

The conditions throughout the port can now be determined by forward integration of Eqs. (46) from the initial conditions given by Eq. (51). The integration was performed numerically with a fourth order Runge-Kutta procedure.

Swirling Flow in Converging-Diverging Nozzles

As mentioned previously a theory for isentropic swirling flow in converging-diverging nozzles has been formulated by Mager⁽²⁶⁾. The analysis was approximate and proceeded from a scalar potential function. The results of the analysis showed that both the mass flow and the vacuum thrust were swirl dependent. In particular Mager showed that

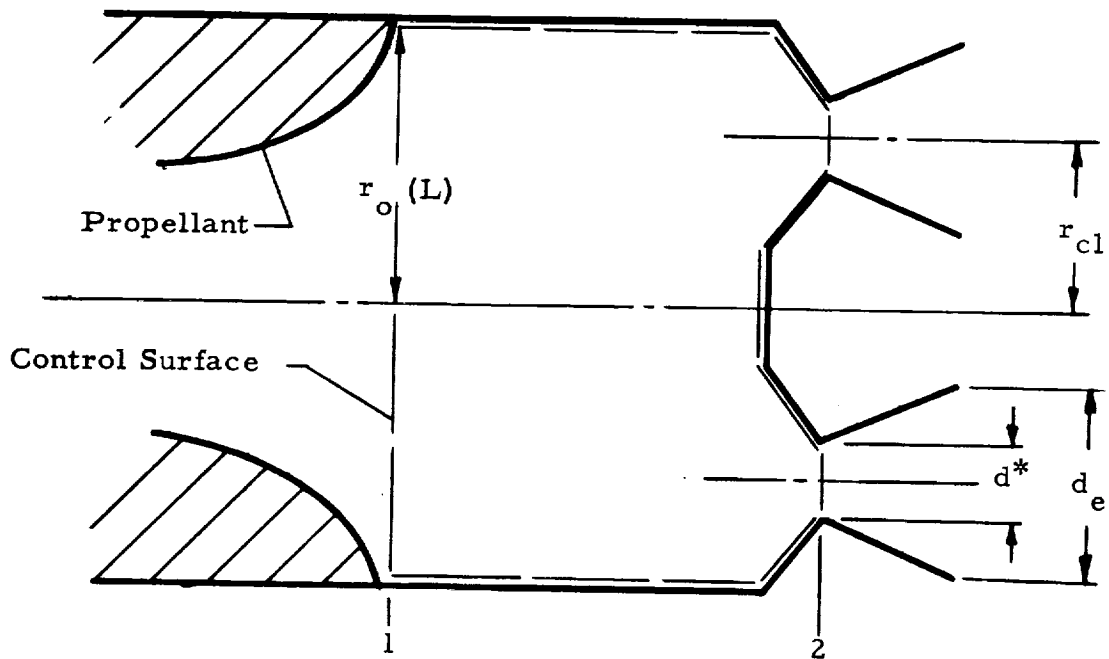
$$\dot{m}/\dot{m}_{1-D} = f(\alpha^*, \gamma) \quad (52a)$$

and

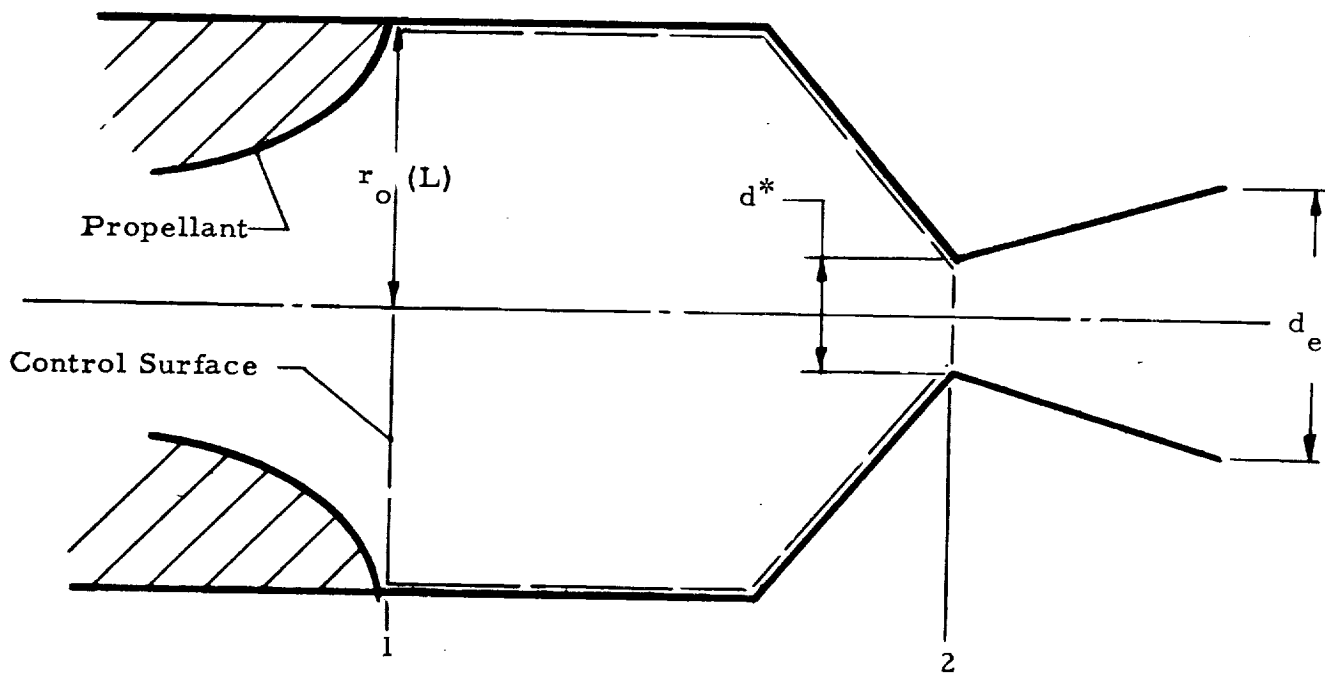
$$F/F_{1-D} = g(\alpha^*, \gamma, \epsilon) \quad (52b)$$

where α^* is a swirl parameter given by the expression

$$\alpha^* = \frac{K^*}{r^* c_t} \sqrt{\frac{\gamma-1}{2}} \quad (53)$$



a. Multiple Nozzles



b. Single Nozzle

Figure 3. Schematic Diagram Illustrating Systems for Nozzle Analysis

and \dot{m}_{1-D} and F_{1-D} are the mass flow rate and thrust without swirl.

The extension of Mager's theory to the problem at hand was accomplished by a moment-of-momentum balance between the exit of the port and the throat of the nozzle(s). Figure 3 is a schematic diagram that illustrates the systems employed for the analysis and shows the nomenclature. It was assumed that in the region between the exit of the port and the throat of the nozzle(s) that the flow was isentropic and that moment-of-momentum was conserved $(MM)_2 = (MM)_1$. The first assumption is compatible with existing internal ballistic procedures. The second assumption is obviously true for axisymmetric geometries where external torques are limited solely to those produced by shear stresses; in multiple nozzle configurations this assumption is largely unjustified because torques produced by pressure forces are possible. However, secondary vortices, which are compatible with the assumption, have been observed in test motors.

The axial moment-of-momentum transported through the control surface at station 1 is

$$(MM)_1 = 2\pi \int_0^{r_o} \rho V_z V_\theta r^2 dr \quad (54)$$

The quantities in the integral being evaluated at $z = L$. The tangential velocity is $V_\theta = K/r$; therefore, Eq. (54) becomes

$$(MM)_1 = K_1 \dot{m} \quad (55)$$

The factor K_1 can be computed from the tangential Mach number and the static temperature at the port exit ($z = L$) by employing the definition of the tangential Mach number or

$$K_1 = r_o(L) \left[M_\theta^2(L) \gamma R t_o(L) \right]^{1/2} \quad (56)$$

Axial moment-of-momentum is transported through station 2 by two modes: (1) rotation of the gas in a nozzle relative to that nozzle and (2) rotation of the gas in a nozzle relative to the centerline of the motor by virtue of the rotation of the nozzles. The moment-of-momentum transported by the first mode is

$$(MM)_2' = \sum_{i=1}^N K_i^* \dot{m}_i \quad (57)$$

The moment-of-momentum transported by the second mode is

$$(MM)_2'' = \sum_{i=1}^N \Omega r_{cl,i}^2 \dot{m}_i \quad (58)$$

The total moment-of-momentum is the sum of these two quantities or

$$(MM)_2 = \sum_{i=1}^N \dot{m}_i \left(K_i^* + \Omega r_{cl,i}^2 \right) \quad (59)$$

In most practical systems the nozzles are identical so that $r_{cl,i} = r_{cl,j}$, $\dot{m}_i = \dot{m}_j$, and $K_i^* = K_j^*$. Therefore, Eq. (59) reduces to

$$(MM)_2 = \dot{m} \left(r_{cl}^2 \Omega + K^* \right) \quad (60)$$

The K factor at the nozzle throat can now be related to that at the exit of the port by equating Eqs. (55) and (60). This yields

$$K^* = K_1 - r_{cl}^2 \Omega \quad (61)$$

Equation (61) shows that for a single nozzle motor ($r_{cl} = 0$) $K_1 = K^*$. However, for a multiple nozzle motor K^* can be equal to, greater than, or less than zero depending upon the relative magnitudes of K_1 and $r_{cl}^2 \Omega$. Since swirl effects in the nozzle are dependent upon the value of α^* and hence K^* , Eq. (61) suggests that swirl effects can be eliminated by proper choice of r_{cl} .

By employing Eqs. (53), (56), and (61) the swirl parameter α^* may be computed thereby permitting Mager's theory to be employed for the determination of swirl effects in the nozzle(s) of a spinning rocket motor.

Equilibrium Ballistics at Fixed Time Computer Program

The preceding sections contain the theoretical background for determining the flow fields in the port and the nozzle(s) of a spinning rocket motor. By employing this knowledge and a mass balance, the equilibrium operating point was determined. The basic computational procedure was as follows: (1) estimate the head end pressure (p^1), (2) integrate Eqs. (46) along the port to determine the mass flow, K factor, and stagnation conditions at the exit of the port, (3) compute the mass flow rate through

the nozzle by employing Eqs. (53) and (61) and Mager's theory, and (4) iterate on p^1 until the mass flows balance.

Figure 4 is a flow diagram that illustrates the major elements of the computer program. The program is divided into eight major blocks: Block 1 - data input, output, and conversion to program units; Block 2 - computation of tables of the ϕ , ψ , g_ϕ , g_ψ functions with M_θ^2 as argument and a table of r_o and z with s as argument; Block 3 - estimation of $p_o(o)$; Block 4 - determination of non-zero starting line values for the Runge-Kutta integration; Block 5 - the numerical integration of Eqs. (46) to the end of the port; Block 6 - computation of the mass rate of flow through the exhaust nozzle(s); Block 7 - error detector and iterator; and Block 8 - output of calculated results.

Block 1 is largely self-explanatory. Units conversion transforms the units employed for the input data to the ft, slug, sec, $^\circ R$, ft-lb_f, lb_f units employed throughout the program.

In Block 2 tables are formed so that functions may be determined by interpolation. The ψ , ϕ , g_ψ and g_ϕ tables are formed from the functions defined by Eqs. (25, 27, I-9, I-10); the integrals are evaluated by employing Simpson's rule. (30) The contour of the burning surface is described by a collection of points specified by their corresponding r and z coordinates. An additional INFO parameter is specified for each point. This parameter determines where the following segment of surface is combustible or not. The collection of points is employed to divide the burning surface into segments that are truncated cones and the distance from the head end (s coordinate) of each point is computed from

$$s_i = s_{i-1} + \left[(r_i - r_{i-1})^2 + (z_i - z_{i-1})^2 \right]^{1/2} \quad (62)$$

The points defining the surface also define the locations where output data are printed.

The head end pressure is estimated in Block 3 under the assumptions that pressure is uniform throughout the port and that there are no total pressure losses, swirl effects in the nozzle, or erosive burning.

Experience with a previous one-dimensional computer program where the influence coefficient equations were integrated numerically showed that computational problems resulted if the Runge-Kutta procedure was started at $s = 0$. The difficulties were associated with zero values for M_z^2 and \dot{m} . Accordingly, a small step was made under the assumption that $p_o = p_o(o)$ to obtain non-zero values for these terms, and the Runge-Kutta integration was begun with these values at $s = \Delta$. The flow diagram illustrates the equations employed to determine the flow variables at $s = \Delta$.

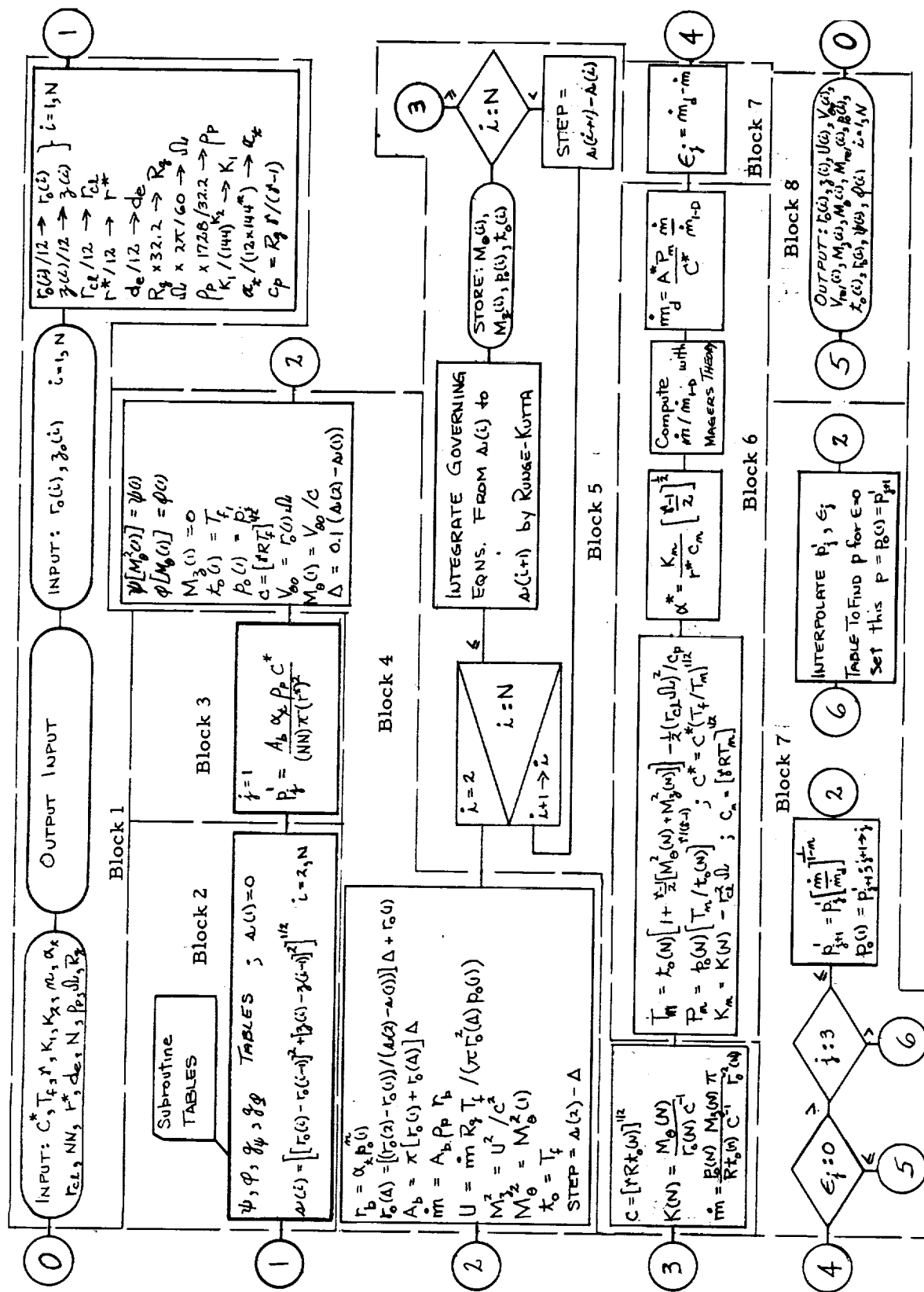


Figure 4. Flow Diagram.

The Runge-Kutta procedure employed in Block 5 was fourth order and was available as a subroutine. The subroutine automatically selected the step size based on an accuracy criteria. The integration proceeds from s_{i-1} to s_i . The dependent variables at s_i are stored in a table for output purposes.

In Block 6 the mass discharge through the nozzle(s) is computed. The total pressure and total temperature relative to the nozzle(s) is computed first, C^* is corrected for temperature deviations, and the mass flow under one-dimensional conditions is computed. The K factor and the nozzle swirl parameter are then computed, and Mager's theory is employed to find the correction to the mass flow due to swirl.

In Block 7 the absolute value of the relative error in mass generation and mass discharge is compared with an acceptable error. If the error is sufficiently small, control passes to Block 8. However, if the error is unacceptable the head end pressure p^1 is re-estimated. For the first three passes through the re-estimation procedure, the next head end pressure is determined from

$$p_j^1 = p_{j-1}^1 \left(\frac{\dot{m}_g}{\dot{m}_d} \right)_{j-1}^{\frac{1}{1-n}} \quad j = 1 - 3 \quad (63)$$

For the fourth and successive passes the p_j^1 -error table is examined to determine the pressure for which the error is zero.

In Block 8 the computed results are printed out. Values are presented at each of the points employed to define the burning surface. These values are computed from the values stored in Block 5.

PHASE II - EFFECT OF ACCELERATION ON BURNING RATE

General

The objective of this phase was to develop analytical burning rate models for composite solid propellants that included acceleration effects. Experimental data⁽³¹⁾ have shown that increased burning rates in metallized propellants are intimately connected with metal/metal oxide that is retained on the burning surface by the acceleration force. Therefore, the rate controlling mechanisms in an acceleration environment must be different for metallized and nonmetallized propellants. Accordingly, different burning rate models were developed for each case. For nonmetallized propellants the granular diffusion flame model of Summerfield⁽³²⁾ was modified to include acceleration effects; for metallized propellants an analytical model originated by Reference 28 was modified to include particle burning, and preliminary studies were made with another particle burning model.

Metallized Propellants

In Reference 28 a theoretical model for the effect of acceleration on the burning rate of metallized composite propellants was advanced. The model is based on the hypothesis that a fraction of the metal that is evolved at the burning surface during the combustion process is retained and burns there. The energy released by this metal combustion increases the energy transfer to the decomposing surface thereby increasing

the burning rate. It was further hypothesized that the process is steady-state and that the metal particles retained on the surface of the propellant burn there until they reach a critical size such that viscous drag overcomes the acceleration force and the particle is literally blown off the surface.

The increase in burning rate was related to the amount of energy released at the propellant surface by the combustion of metal particles through the steady state energy balance

$$[r_b - (r_b)_{a=0}] h_v = r_b w_M Q_M f \quad (64)$$

where r_b is the burning rate, h_v is the energy required to heat up and gasify a unit mass of propellant, w_M is the mass fraction of metal in the propellant, Q_M is the energy released to the burning surface in the combustion of a unit mass of metal, and the function f represents the fraction of metal mass that must be removed from a distribution of particles such that all particles larger than the critical size are reduced to the critical size. The left-hand side of the equation represents the amount of energy required for a rate increase from $(r_b)_{a=0}$ to r_b , while the right-hand side represents the amount of energy released at the surface of the propellant by the combustion of the metal particles.

Rearrangement of Eq. (64) gives the burning rate ratio explicitly as

$$r_b / (r_b)_{a=0} = \left[1 - \frac{w_M Q_M f}{h_v} \right]^{-1} \quad (65)$$

Equation (65) shows that the maximum burning rate that can be achieved is dependent upon the parameter $w_M Q_M / h_v$ and that this parameter must be less than one for physically meaningful results.

The most difficult task was to determine the function f . This was accomplished by assuming that the particles were spherical and that the particle size distribution obeyed a log normal distribution. After performing suitable mathematical manipulations, the following result was obtained

$$f = \frac{1}{2} \left[\operatorname{erfc} \left[\ln (\xi'_M / \xi_{Mm}) / \sigma \right] - (\xi'_M / \xi_{Mm})^3 e^{9\sigma^2/2} \operatorname{erfc} \left[\ln (\xi'_M / \xi_{Mm}) / \sigma + 3\sigma \right] \right]. \quad (66)$$

The critical particle size was determined from a force balance between viscous drag and inertial forces. With the further assumption of Stokes flow this yielded

$$\xi'_M = \left[\frac{9}{2} \frac{\mu_{go} r_b \rho_p}{\rho_a \rho_{go} a} \right]^{1/2} \quad (67)$$

Thus, for a particular propellant the radius ratio becomes, in general,

$$\xi'_M / \xi_{Mm} = \left[[r_b / (ap)] / [r_b / (ap)]_c \right]^{1/2} \quad (68)$$

For a particular propellant in a particular motor at equilibrium conditions Eq. (68) reduces to

$$\xi'_M / \xi_{Mm} = (a_c / a)^{1/2} \quad (69)$$

Examination of Eqs. (68) and (69) shows that by specifying $w_M Q_M / h_v$, σ , and the operating conditions, the burning rate increase due to acceleration can be determined.

The approach presented above in brief represents the first serious and thoughtful approach to the problem. Unfortunately, the approach deviates from observed physical phenomena. First, the burning surface is pitted.⁽³¹⁾ This indicates that increased burning rates are attained only at certain locations; the theory assumes the rate increase is uniform. Second, particulate residue whose size is large compared with the particle size of the metal additive is retained in the motor after firing.^(28, 31) This suggests that agglomeration occurs on the burning surface; the theory neglects agglomeration. These two discrepancies together with the fact that the theory gives no information regarding the effect of non-normal acceleration forces form the basic objections to the theory developed by Reference 28.

The basic objections listed above are largely concerned with the neglect of particle burning effects. Accordingly the theory of Reference 28 was modified to include particle burning effects within the general framework of the theory. In particular, the following assumptions were introduced:

1. Condensed phase particles that are initially retained on the burning surface agglomerate and remain on the burning surface.
2. The interaction between the retained condensed phase material and the burning surface occurs only at a finite number of points.

3. The line of descent of the agglomerated metal through the propellant is colinear with the acceleration force vector.

The other assumptions were unchanged.

Figure 5 illustrates the analytical model employed. The figure shows conical pits in the burning surface, the mean burning surface, the agglomerated metal particle, and illustrates some of the nomenclature.

The rate of descent of a single agglomerated particle through the propellant (r_{ba}) was computed from an energy balance between the amount of energy required to increase the burning rate above the base rate and the energy supplied through combustion of metal at the particle. The energy required to increase the burning rate above the base rate is

$$\dot{E}_r = [r_{ba} - (r_b)_{a=0}] h_v \rho_p A_i \quad (70)$$

where A_i is the effective interaction area of the particle with the propellant. This area was assumed to be the area where the local burning rate was modified (refer to Figure 5) and is

$$A_i = \pi (\xi_a \cos \theta_c)^2 \quad (71)$$

However, $\cos^2 \theta_c = 1 - \sin^2 \theta_c$ and $\sin \theta_c = (r_b)_{a=0} / r_{ba}$. Therefore, Eq. (71) becomes

$$A_i = \pi \xi_a^2 \left[1 - [(r_b)_{a=0} / r_{ba}]^2 \right] \quad (72)$$

Since the surface is pitted, any metal added to the agglomerated particle must originate within its own cone. If it is assumed that there are N_s pits per unit area of the mean burning surface¹, the area swept by each pit is

$$A_s = N_s^{-1} \cos \phi \quad (73)$$

1. This assumption is equivalent to relating the number of pits to the physical structure of the propellant.

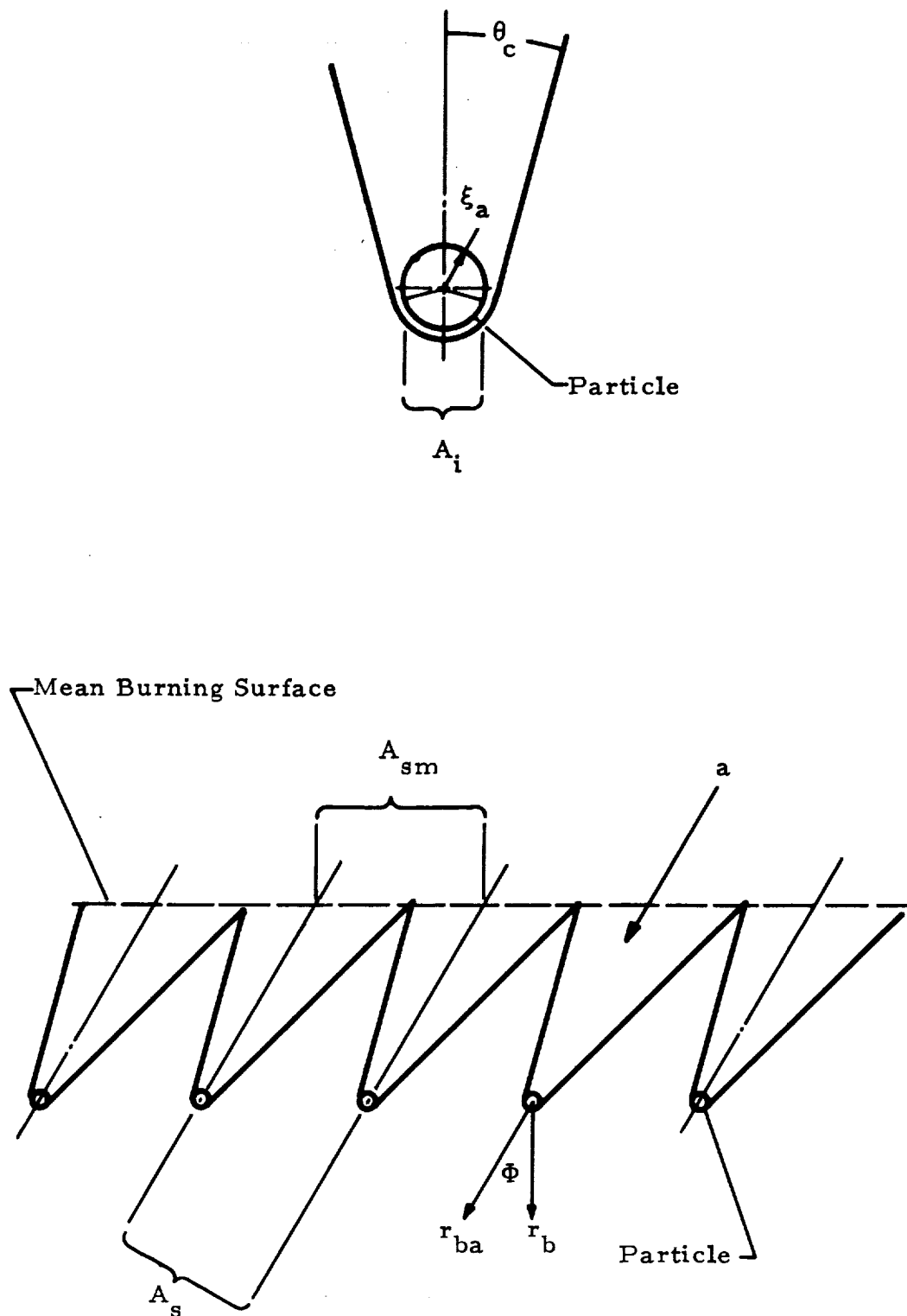


Figure 5. Analytical Model for Particle Burning.

Therefore, the metal added to the agglomerated particle in unit time is

$$\dot{m} = r_{ba} \rho_p w_M \left[A_i + (A_s - A_i) G \right] \quad (74)$$

It has been assumed that all of the metal particles evolved in the interaction area are agglomerated but that only the fraction G of the metal evolved on the sides of the cone is agglomerated. Since the process has been assumed to be invariant with time, this metal must be burned in unit time. However, all of the energy released in this process will not reach the interaction area. To compute the fraction that does, it was assumed that the energy release was uniform over the surface of the sphere. Therefore, if ΔH_c is the lower heating value for the combustion of the metal in the products of combustion of the binder and the oxidizer, the energy supplied to the burning surface is

$$\dot{E}_s = 2\pi r_{ba} \xi_a^2 \rho_p w_M \Delta H_c \left[A_i + (A_s - A_i) G \right] \left[1 - (r_b/a)_{a=0}/r_{ba} \right] \quad (75)$$

The burning rate r_{ba} may be determined by equating Eqs. (70) and (75). This yields

$$\frac{r_{ba}}{(r_b/a)_{a=0}} = \frac{1 - \Pi(1 - G)}{1 - \Pi[1 + (\beta - 1)G]}^{1/2} \quad (76)$$

where $\Pi = w_M \Delta H_c / (2 h_v)$ and $\beta = (N_s \pi \xi_a^2)^{-1} \cos \Phi$. Equation (76) gives the rate of descent of the agglomerated particle through the propellant. However, the burning rate desired is the regression rate of the mean burning surface r_b . Examination of the vector diagram on Figure 5 shows that

$$r_b = r_{ba} \cos \Phi \quad (77)$$

Therefore, the burning rate ratio desired becomes

$$\frac{r_b}{(r_b/a)_{a=0}} = \frac{1 - \Pi(1 - G)}{1 - \Pi[1 + (\beta - 1)G]}^{1/2} \cos \Phi \quad (78)$$

Equation (78) shows the following: the maximum burning rate occurs when the acceleration force is normal to and into the burning surface; the burning rate reaches an upper bound at high accelerations ($G = 1$) given by

$$\left[\frac{r_b}{(r_b)_{a=0}} \right]_{\max} = (1 - \Pi \beta)^{-1} \quad (79)$$

so that the term $\Pi \beta$ must be less than one, and some critical angle Φ_c exists¹ beyond which acceleration does not effect burning rate. The latter occurs because the burning rate ratio must be greater than or equal to one. Thus, for angles greater than Φ_c , Eq. (78) is invalid.

The function G is the fraction of metal evolved on the sides of the cone that is agglomerated and retained. Therefore, G is simply the first term of Eq. (66) or

$$G = \operatorname{erfc} \left[\ln(\xi_M' / \xi_{Mm}) / \sigma \right] / 2 \quad (80)$$

Moreover, analysis shows that when the drag coefficient is that for Stokes flow the radius ratio given by Eqs. (68) and (69) remains valid for particles on the surface of the cones. Therefore, the effect of acceleration on burning rate can be determined by employing Eqs. (68), (78), and (80).

Nonmetallized Propellants

The objective of this part of the study was to extend the granular diffusion flame burning rate model developed by Summerfield⁽³²⁾ so that acceleration effects would be included.

The basic features of the granular diffusion flame model are as follows:

1. A quasi-steady gaseous flame exists adjacent to the burning surface.
2. The burning surface is dry (the oxidizer and fuel vapors are liberated directly from the solid phase by sublimation or pyrolysis).
3. No significant chemical reactions occur outside the gaseous flame zone adjacent to the burning surface.

1. Φ_c is defined as the angle at which $r_b / (r_b)_{a=0} = 1$.

4. The vapors of oxidizer or fuel, or both, are released in the form of pockets with a certain mass content and these pockets proceed to burn in the surrounding medium of the opposite reactant (granular diffusion flame).
5. Burning occurs as a result of energy fed back from the flame to the exposed surface of the propellant.
6. Transport phenomena in the gas phase reaction zone are molecular in nature.

Figure 6 is a schematic diagram of the granular diffusion flame model. The important items illustrated are the heterogeneous solid propellant composed of a solid fuel binder and small particles of ammonium perchlorate oxidizer, the burning surface, the gas phase reaction zone, and the reacted gases.

An energy balance at the burning surface was employed to relate the burning rate of the propellant to the rate of heat transfer from the gases to the burning surface or (considering unit area)

$$q_s'' = r_b \rho_p \left[c_p (T_s - T_i) - Q_s \right] \quad (81)$$

The rate of heat transfer was related to the temperature difference across and the thickness of the gas phase reaction zone by

$$q_s'' = \lambda_g (T_f - T_s) / \delta_r \quad (82)$$

The thickness of the gas phase reaction zone was related to the nature of the zone by solving this problem for limiting cases of low pressure and high pressure and then joining these solutions. At low pressure, since the rate of molecular diffusion is very much faster than the oxidation reaction, the zone was assumed to be a premixed flame in which a second order reaction was taking place. The thickness of the gas phase reaction zone in this case was shown to be

$$\delta_r' = \frac{r_b \rho_p}{\rho_g} \left[(1 - \epsilon)^2 \rho_g A \exp(-E/RT_g) \right] \quad (83)$$

On the other hand, at very high pressure, the chemical reaction rate is so fast that the rate of oxidation is controlled entirely by the rate of interdiffusion and the burning rate is determined by the granular nature of the zone. Since the pockets of fuel vapor are embedded in the oxidizer vapor, the thickness of the gas phase reaction zone

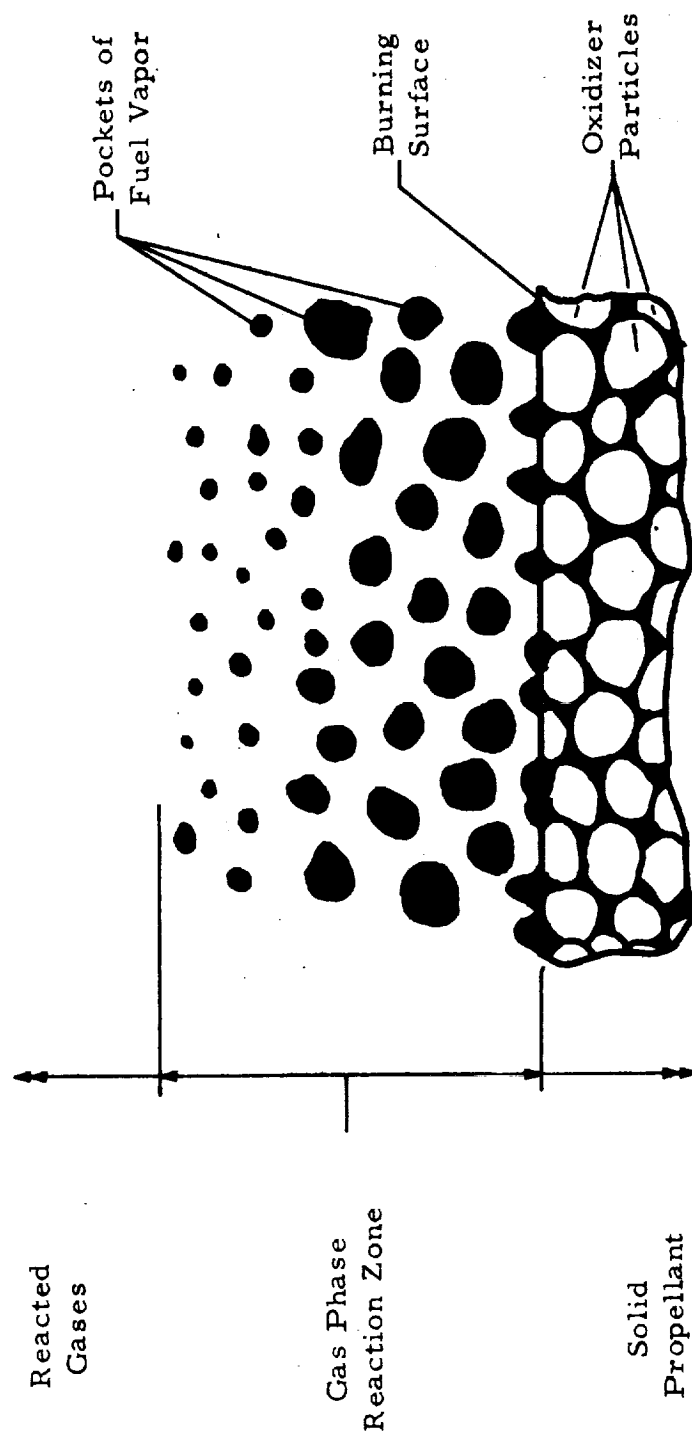


Figure 6. Schematic Diagram Illustrating the Granular Diffusion Flame Model

was taken to be the product of the lifetime of an average pocket and the average velocity of the gas in the zone or

$$\delta_r'' = v_g \tau_{fv} \quad (84)$$

The average gas velocity was related to the burning rate by a mass balance at the burning surface or

$$v_g = r_b \rho_p / \rho_g \quad (85)$$

The average lifetime of a fuel vapor pocket was related to the characteristic dimensions of the pocket and the diffusivity of the gases by

$$\tau_{fv} \propto d_{fv}^2 / D_g \quad (86)$$

The mass of the pocket of fuel vapor was related to the mean dimension of the pocket and the mean density of the gases by

$$m \propto \rho_g d_{fv}^3 \quad (87)$$

Therefore, by combining Eqs. (84-87) and rearranging, it was found that

$$\delta_r'' \propto \frac{r_b \rho_p m^{2/3}}{\rho_g^{5/3} D_g} \quad (88)$$

The thickness of the gas phase reaction zone at intermediate pressures was determined by a linear combination of the thicknesses for the limiting cases or

$$\delta_r = z_1 \delta_r' + z_2 \delta_r'' \quad (89)$$

Introduction of the above expressions into Eq. (81) yielded

$$(r_b)_{a=0}^{-1} = \left[\frac{\rho_p^2 [c_p (T_s - T_i) - Q_s]}{\lambda_g (T_f - T_s)} \right]^{1/2} \left[\frac{z_1}{\rho_g A \exp(-E/R_u T_g)} + \frac{z_2 m^{1/3}}{D_g^{1/2} \rho_g^{5/6}} \right] \quad (90)$$

The scope of this work is the pressure range of practical interest ($p > 600$ psia). In this range, experimental data presented by Reference 32 show that the combustion phenomenon is dominated by the rate of interdiffusion; this result is consistent with the basic analytical model. Therefore, the analysis will be limited to the effect of acceleration on the limiting case for high pressures.

With the granular diffusion flame model, acceleration induced changes in burning rate must originate from acceleration induced effects within the gas phase reaction zone. Two effects appear possible. First, the acceleration field will produce a pressure difference across the gas phase reaction zone. Second, the acceleration field will act on the density inhomogeneities within the gas phase reaction zone.

The order of magnitude of the acceleration induced pressure change across the gas phase reaction zone is readily estimated. Figure 7 is a sketch that illustrates the system for estimating this pressure difference. Application of the momentum theorem to the control surface illustrated yields (employing D'Alembert's principle)

$$p_s - p_f = r_b \rho_p (v_f - v_s) + \delta_r \rho_g a \quad (91)$$

Equation (91) shows that the pressure difference is due to two factors: the momentum change of the gas and the acceleration induced body force. It is also seen that the first term is not explicitly dependent upon the acceleration level.

The order of magnitude of the two terms in Eq. (91) will be estimated for the typical conditions tabulated in Table C-I and the maximum acceleration level encountered in practice (50,000 g). This yields

$$O [r_b \rho_p (v_f - v_s)] = 2.4 \times 10^{-2} \text{ psi} \quad (92)$$

$$O [\delta_r \rho_g a] < 8 \times 10^{-2} \text{ psi} \quad (93)$$

Since the pressure level of interest is greater than 600 psia, it is seen that both of these effects are negligible. Therefore, pressure is essentially constant across the gas phase. In addition, it may be concluded that the observed effect of acceleration on burning rate must be caused by the action of the acceleration field on the density inhomogeneities in the gas phase reaction zone.

Density inhomogeneities within the gas phase reaction zone arise from the following main sources: the heterogeneous nature of the zone and the mean temperature gradient through the zone. Thus, the gas phase reaction zone may be pictured as having mean characteristics that are dependent only upon the distance from the mean burning surface and heterogeneous characteristics that are dependent upon both spatial location and time. The latter are typified by pockets of fuel vapor embedded in oxidizer vapor. The action of the acceleration field on the mean characteristics of the zone will produce a mean fluid motion that will be closely related to free convection flows. On the other hand, the action of the acceleration field on the heterogeneous characteristics will

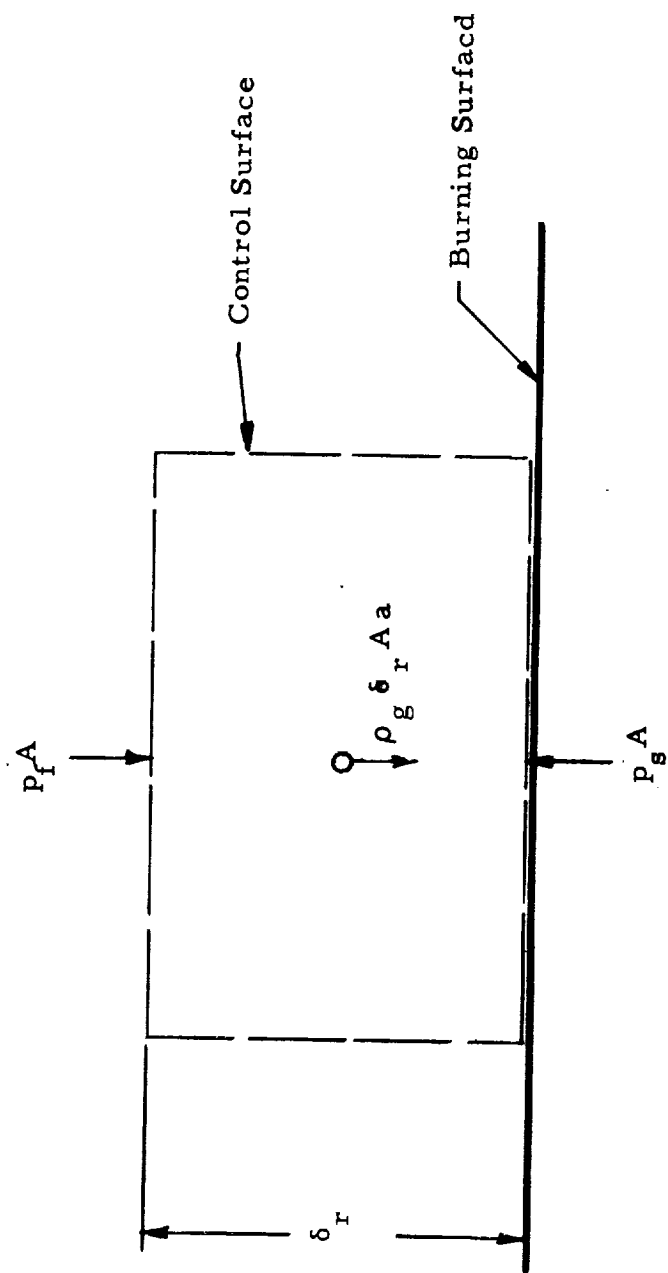


Figure 7. Sketch Illustrating System Employed for Estimating the Pressure Difference Across the Gas Phase Reaction Zone

produce relative motion between the pockets of fuel vapor and the surrounding oxidizer vapors. These two effects will be considered separately.

The nature of the effects produced by an acceleration field acting on the mean density gradient within the gas phase reaction zone will depend upon the magnitude and direction of the acceleration force relative to the burning surface. When the acceleration force is normal to and into the burning surface, no effects due to this source can occur because the acceleration force is aligned with the density gradient and no flow can result. On the other hand, when the acceleration force has a direction opposite to the density gradient, free convection flow should be possible. However, a one-dimensional flow is impossible because the denser gas would have to ascend at the same time that the lighter gas was descending. Experimental and theoretical results show that for the case where the fluid is bounded by impermeable walls, no flow occurs as long as the product of the Grashof¹ and Prandtl numbers is small. (33) However, when this product reaches a value around 1700, a cellular flow in which the cold, dense fluid ascends in the center of each cell and the hot, light fluid descends along the rim of the cell is initiated. (33) The effect of this flow is to effectively increase the rate of heat transfer from the hot to the cold plate. Reference 33 also shows that this increase can be accounted for by a fictitious thermal conductivity and that this conductivity is a function of the product of the Grashof and Prandtl numbers.

These results suggest that a similar phenomenon could occur in the gas phase reaction zone when the acceleration force vector is away from the burning surface and sufficiently large. However, the question arises as to the effect of the vertically upward flow that occurs in the case of burning propellant. Since increased heat transfer (and increased burning rate) depends, in the case of a cellular flow, upon the downward convection of hot, reacted gases, it appears that a vertically upward flow would block this flow and delay any appreciable effect of the cellular flow on the burning rate until the Grashof-Prandtl product is significantly greater than 1700.

The Grashof number is

$$Gr_{\delta} = \frac{a \rho_g \delta_r^3 (\rho_s - \rho_f)}{\mu_g^2} \quad (94)$$

Therefore, the acceleration required to initiate the cellular flow when there is no mean upward flow is

$$a_{cf} = \frac{1700 \mu_g^2}{\rho_g \delta_r^3 (\rho_s - \rho_f) Pr} \quad (95)$$

1. The characteristic dimension in the Grashof number is the thickness of the zone.

Substitution of the typical values found in Table C-I into Eq. (95) shows that $a_c \approx 3000g$. In certain applications, acceleration levels of 50,000 g are encountered. However, it is expected that cellular flow effects will not be important in practice because of the stabilizing effect of the vertical gas flow and the facts that sustained high acceleration occur only in spinning rocket motors¹ and grain configurations that possess propellant surfaces normal to and away from the acceleration force cannot be supported at high acceleration levels. In other words, structural considerations will, in general, prohibit a situation where this effect could be significant. For these reasons, this effect will not be considered further.

The preceding discussion shows that acceleration induced mean flows will not occur in situations of practical interest when the acceleration force is normal to the burning surface. Therefore, it can be concluded that mean flow effects can occur only when a component of the acceleration force is parallel to the burning surface.

When a component of the acceleration vector is parallel to the burning surface, a free convection flow having a boundary layer character will result. Exact treatment of this problem is difficult. Therefore, an approximate treatment will be made to determine the severity of the effects that could result from these flows. Further work on this aspect of the problem will depend on the results of this study.

In the granular diffusion flame model, the thickness of the gas phase reaction zone is controlled by the product of the vertical velocity of the gas and the lifetime of a pocket of fuel vapor. The effect of a mean flow parallel to the surface on these quantities should not be extremely large. Therefore, the thickness of the gas phase reaction zone will remain relatively constant. Since this thickness is small and phenomena that can effect the burning rate must occur within this zone, the mean flow in the gas phase reaction zone must exhibit a boundary layer character. That is, variations of parameters along the burning surface will be small compared with variations of the same parameters normal to the surface. Moreover, at large distances measured along the burning surface from the edge of the propellant, the variation of parameters with distance from the edge will be very small.

The boundary layer equations for laminar free convection flows of a compressible fluid are⁽³³⁾

$$\rho \left(u \frac{\partial u}{\partial x} + \frac{\partial u}{\partial y} \right) = a_x (\rho - \rho_f) + \frac{\partial}{\partial y} \left(\mu \frac{\partial u}{\partial y} \right) \quad (96)$$

and

$$\frac{\partial (\rho u)}{\partial x} + \frac{\partial (\rho v)}{\partial y} = 0 \quad (97)$$

-
1. Very high accelerations can occur in gun boosted rockets while the rocket is in the gun. However, the duration of these accelerations is very short.

Since variations with distance along the burning surface will be small and the order of magnitude of u and v will be essentially the same, the order of magnitude of the term $v \partial u / \partial y$ will be greater than that of $u \partial u / \partial x$. Therefore, Eq. (96) can be reduced to

$$\rho v \frac{\partial u}{\partial y} = a_x (\rho - \rho_f) + \frac{\partial}{\partial y} \left(\mu \frac{\partial u}{\partial y} \right) \quad (98)$$

Since variations with distance along the burning surface are small, Eq. (97) shows that

$$\rho v \approx \text{constant} \quad (99)$$

In Eq. (99) the constant is the value at the burning surface $r_b \rho_p$.

The viscous shear stress is

$$\tau = \mu \frac{\partial u}{\partial y} \quad (100)$$

Equation (98) can be rewritten in terms of the viscous shear stress as

$$\frac{\partial \tau}{\partial y} = \frac{r_b \rho_p}{\mu} \tau - a_x (\rho - \rho_f) \quad (101)$$

At the edge of the gas phase reaction zone $(\rho - \rho_f) = 0$; therefore, for the region beyond this zone ($y \geq \delta_r$)

$$\frac{\partial \tau}{\partial y} = -\frac{r_b \rho_p}{\mu} \tau \quad (102)$$

Equation (102) shows the following:

- (a) If $\tau(x, \delta_r) > 0$, $\lim_{y \rightarrow \infty} \tau = \infty$.
- (b) If $\tau(x, \delta_r) < 0$, $\lim_{y \rightarrow \infty} \tau = -\infty$.

It can be concluded that $u(x, \delta_r) = 0$. Therefore, at $y = \delta_r$

$$\partial u / \partial y = \partial^2 u / \partial y^2 = 0 \quad y \geq \delta_r \quad (103)$$

The lateral body force on a fluid particle crossing the zone will impart an axial momentum to it. It may be concluded that $u(x, \delta_r) > 0$.

The velocity profile through the gas phase reaction zone will be approximated with the third order polynomial

$$u = c_0 + c_1 \eta + c_2 \eta^2 + c_3 \eta^3 \quad (104)$$

where $\eta = y / \delta_r$. The four parameters are evaluated by employing Eq. (103), the no slip condition at the burning surface, and Eq. (98) evaluated at the burning surface. The evaluation yields

$$u = \frac{(\rho_s - \rho_f) a_x \delta_r}{\rho_p r_b} \frac{Re_\delta}{Re_\delta + 2} \eta [1 - \eta + \eta^2/3] \quad (105)$$

where $Re = r_b \rho_p \delta_r / \mu$. Thus, the velocity at the outer edge of the gas phase reaction zone is

$$u(x, \delta_r) = \frac{a_x \delta_r (\rho_s - \rho_f) Re_\delta}{3 r_b \rho_p (Re_\delta + 2)} \quad (106)$$

The question now arises as to how this mean flow can effect the burning rate. Within the framework of the granular diffusion flame model the burning rate is directly related to the ratio λ_g / δ_r . Thus, acceleration induced mean flow effects must be related to λ_g and δ_r . Two effects appear possible: (1) increase in the effective value for λ_g through turbulence generated by lateral acceleration forces acting on the density inhomogeneities in the reaction zone and (2) decrease in δ_r by the mean flow. The first possibility is beyond the scope of this analysis; however, it certainly represents a phenomenon that could limit the range of validity of the analysis. The second effect requires a mechanism for coupling the acceleration induced mean flow with the lifetime of a fuel vapor pocket. Figure 8 illustrates a possible coupling mechanism-velocity gradient deformation of the fuel vapor pockets. The figure shows that a pocket embedded in a velocity gradient is progressively deformed so that the effective length is increased and the effective thickness decreased. Since the lifetime of a pocket is related to its smallest characteristic dimension, it is seen that velocity gradient deformation can decrease the lifetime of the pocket. Therefore, velocity gradient deformation of the

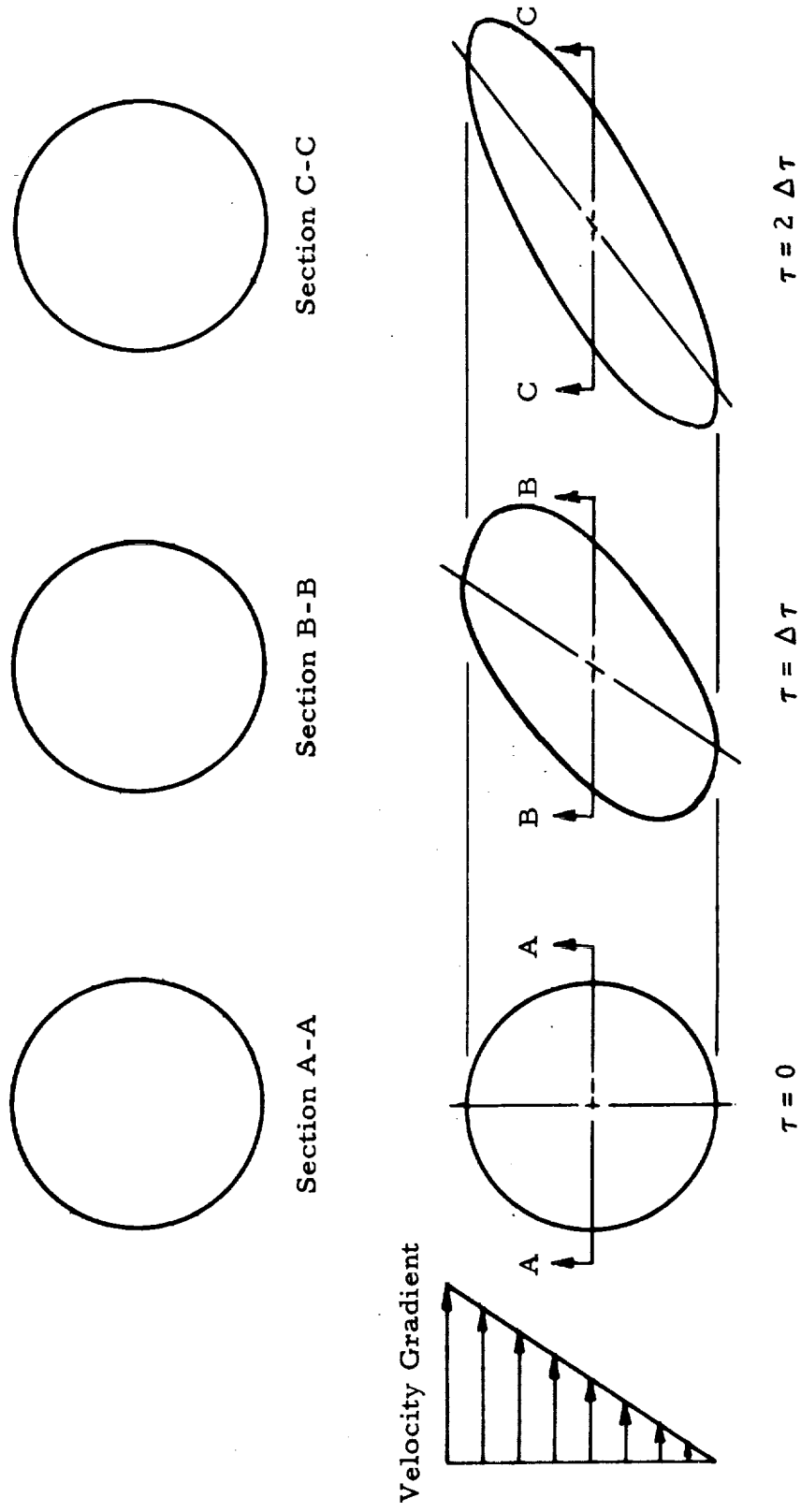


Figure 8. Sketch Illustrating the Deformation of a Spherical Fuel Vapor Pocket by a Velocity Gradient

fuel vapor pocket provides a coupling mechanism between acceleration induced mean flows and the combustion phenomenon. Note that these flows could be produced by pressure gradients (erosive burning effects).

Figure 9 illustrates the analytical model and nomenclature chosen for the analysis of fuel vapor pocket deformation by a velocity gradient. The pocket is idealized as a parallelepiped. The figure shows the pocket at some time τ after its creation (solid lines) and at a later time $\tau + \Delta\tau$ (dashed lines). The pocket at time $\tau + \Delta\tau$ has been displaced so that its lower leading edge coincides with that of the pocket at time τ . In the time interval $\Delta\tau$ the distance S increases so that

$$\Delta S = \Xi \frac{\partial u}{\partial y} \Delta\tau \quad (107)$$

From Figure 9 it is seen that

$$\tan(\omega + \Delta\omega) = (\Xi \tan \omega + \Xi \frac{\partial u}{\partial y} \Delta\tau) / \Xi. \quad (108)$$

However, the tangent of the sum of the two angles is⁽³⁰⁾

$$\tan(\omega + \Delta\omega) = \frac{\tan \omega + \tan \Delta\omega}{1 - \tan \omega \tan \Delta\omega}. \quad (109)$$

Equating these two expressions, expanding, and simplifying yields

$$\frac{\tan \Delta\omega}{\Delta\tau} = \frac{\partial u}{\partial y} \sec^2 \omega + \tan \omega \frac{\partial u}{\partial y}. \quad (110)$$

Expanding the tangent of $\Delta\omega$ in a Maclaurin series, substituting this result into Eq. (110) and taking the limit of the resulting expression as $\Delta\tau$ approaches zero yields¹

$$\frac{d\omega}{d\tau} = \cos^2 \omega \frac{du}{dy}. \quad (111)$$

1. It is assumed here that $u = f(y)$ and that $\tan \omega$ and $\partial u / \partial y$ are finite.

Time is related to the normal velocity of the pocket by

$$\frac{d y}{d \tau} = v. \quad (112)$$

The desired end of the analysis is to determine how a velocity gradient affects the lifetime of a fuel vapor pocket traversing it. It is assumed that the pocket is consumed according to Piobert's law. Then, if \dot{S} represents the rate of consumption along a normal to the surface of the pocket, the time rate of change of the length of the pocket is¹

$$\frac{d \xi}{d \tau} = \frac{2 \dot{S}}{\cos \omega} \quad (113)$$

Since $\xi(0) = \Sigma(0)$ and $\xi \leq \Xi$, it is seen that the lifetime of the pocket corresponds to the time required for ξ to go from $\xi(0)$ to 0.²

Combining Eqs. (111) and (112) and separating the variables yields

$$\frac{d \omega}{\cos^2 \omega} = \frac{d u}{v} \quad (114)$$

To be in accord with the averaging approach employed by Summerfield in the granular diffusion flame model, it is assumed that $v = \text{constant}$. Therefore, Eq. (114) can be integrated to yield

$$\tan \omega = u/v \quad (115)$$

Equation (115) shows that $\omega = 0$ at the birth of the pocket and increases as the pocket moves away from the surface.

The effect of this distortion on the lifetime of the pocket can be obtained by substituting Eq. (115) into Eq. (113). This yields

$$d \tau = \frac{\cos [\tan^{-1}(u/v)]}{2 \dot{S}} d \xi \quad (116)$$

-
1. It is important to note that $d \xi / d \omega = 0$. Therefore, ξ changes only when the pocket is consumed.
 2. Note that at any time τ , $\Sigma = \xi \cos \omega$. Therefore, when $\xi = 0$, $\Sigma = 0$.

If $\omega \approx 0$, then $\cos \omega \approx 1 - \omega^2/2$ and $\tan \omega \approx \omega$. Therefore, Eq. (116) becomes

$$d\tau \approx \frac{2 - (u/v)^2}{4 \dot{S}} d\xi \quad (117)$$

Working with means, we have $d\tau \approx \tau_{fv}$ and $d\xi / (2\dot{S}) \approx (\tau_{fv})_{a=0}$ where $(\tau_{fv})_{a=0}$ is the lifetime of the fuel vapor pocket with no distortion effects. Moreover, $u(x, \delta_r) \geq u(x, y)$ and $v(x, y) \geq v(x, o)$. Substitution of these approximations into Eq. (117) yields

$$\tau_{fv} / (\tau_{fv})_{a=0} \geq [2 - u(x, \delta_r) / v(x, o)] / 2 \quad (118)$$

The acceleration levels of importance to this study are somewhat less than 1000 g. The velocity $u(x, \delta_r)$ can be estimated by employing this acceleration, the values tabulated in Table C-I, and Eq. (106). This yields $u(x, \delta_r) \approx 0.4$ ft/sec. A typical value for $v(x, o)$ is tabulated in Table C-I as v_g . Substituting these results into Eq. (118) yields $\tau_{fv} / (\tau_{fv})_{a=0} \approx 0.9992$. It can be concluded that burning rate changes produced by mean flow effects are negligible for the acceleration level of interest in this study. It can be further concluded that the effect of acceleration on burning rate is connected with the heterogeneous nature of the gas phase reaction zone.

The effect of an acceleration field on the heterogeneous nature of a gas phase reaction zone will be typified by the action of an acceleration field on a pocket of fuel vapor embedded in a steady flow of oxidizer vapor. Figure 10 is a schematic diagram that illustrates the analytical model. The schematic diagram illustrates the pocket of fuel vapor and the forces involved.

In the framework of the granular diffusion flame model in the high pressure limit, the thickness of gas phase reaction zone is

$$\delta_r'' = v_{fv} \tau_{fv} \quad (119)$$

where v_{fv} is the normal velocity of the fuel vapor pocket and τ_{fv} is the lifetime of the pocket. Since the burning rate is inversely proportional to the thickness of the gas phase reaction zone, the effects of acceleration on burning rate must be explainable by the effects of acceleration on v_{fv} and τ_{fv} .

The density of the oxidizer and fuel vapors are, in general, different. Therefore, in an acceleration field, the pocket of fuel vapor will move relative to the oxidizer vapor. This movement will affect v_{fv} . Moreover, the direction of the acceleration will determine whether the normal velocity of the pocket of fuel vapor is greater than, equal to, or less than the velocity of the flow surrounding it. In addition, relative motion between the pocket of fuel vapor and the surrounding oxidizer vapor will always increase the rate of interdiffusion, thereby decreasing the lifetime of the pocket. Therefore, it is seen that

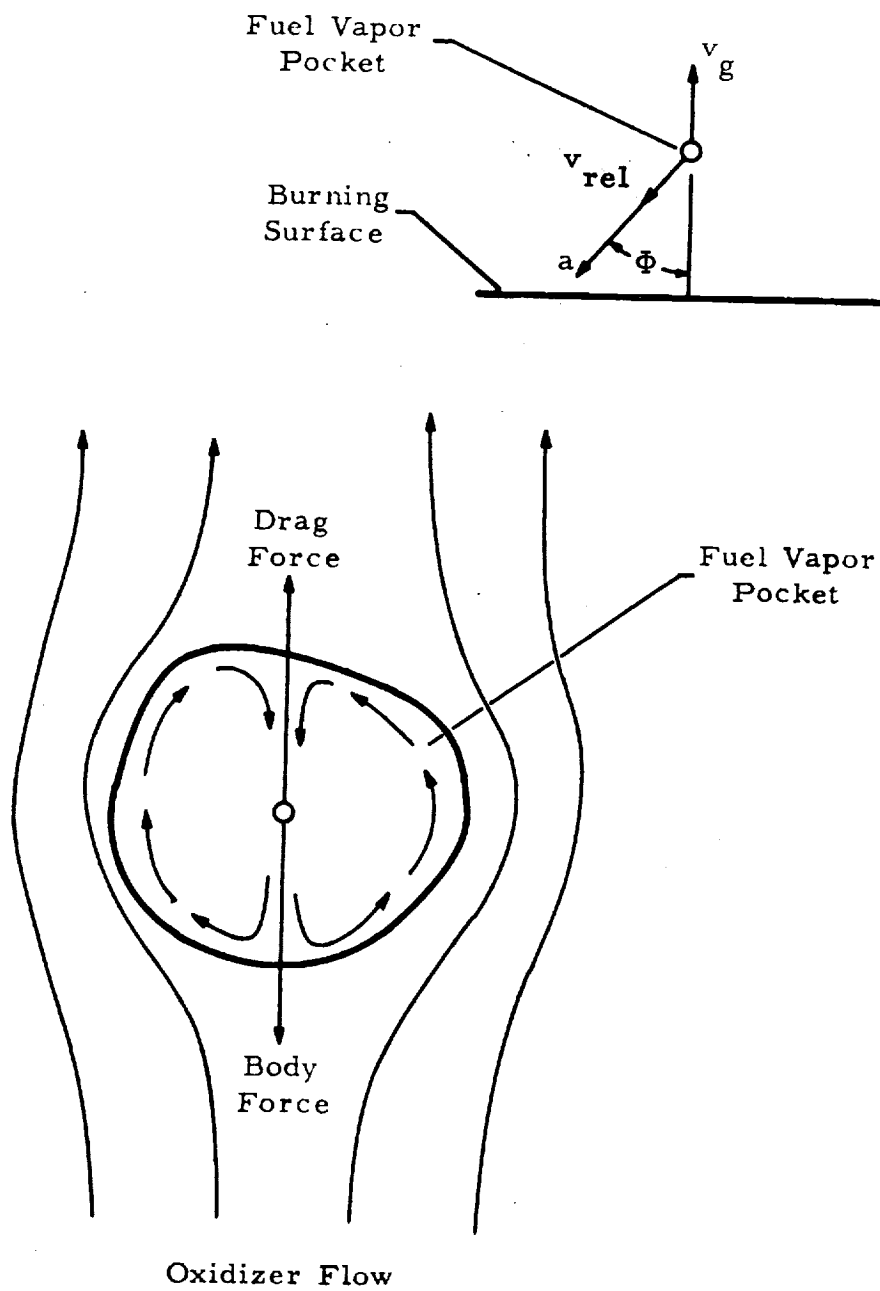


Figure 10. Schematic Diagram of the Analytical Model

the action of the acceleration field produces two distinct effects. First, the lifetime of the pocket is reduced. Second, the upward velocity of the pocket is altered. It is important to note that the first effect is a scalar effect while the second is a vector effect.

Assume now that the density of the fuel vapor is greater than the density of the oxidizer vapor. Therefore, when the acceleration force is normal to and into the burning surface, the vertical velocity of the pocket is reduced ($v_{fv} < v_g$) and the lifetime is decreased. On the other hand, when the acceleration force is normal to and away from the burning surface, the vertical velocity of the pocket is increased ($v_{fv} > v_g$), but the lifetime of the particle is decreased. Finally, when the acceleration is parallel to the burning surface, the vertical velocity of the pocket is unchanged ($v_{fv} = v_g$), but the lifetime of the pocket is decreased. It may be concluded that an acceleration force into the propellant will cause relatively large increases in burning rate while accelerations away from the propellant should produce small effects, the direction of which will depend upon the relative magnitude of the two effects. Finally, an acceleration parallel to the burning surface should cause only moderate to small increases. It is important to note that the available data indicate this trend.

The motion of the pocket is governed by the acceleration induced body force (reversed effective force) $\Lambda \Delta \rho a$ and the drag force $\rho_g C_d A \bar{V}_{rel} |\bar{V}_{rel}|/2$. It will be assumed that these two forces are equal and opposite. The volume of the pocket is

$$\Lambda \propto d_{fv}^3 \quad (120)$$

and the frontal area is

$$A \propto d_{fv}^2 \quad (121)$$

Therefore, the relative velocity between the fuel vapor pocket and the oxidizer vapors is

$$V_{rel} \propto \left[\frac{a d_{fv} \Delta \rho}{\rho_g C_d} \right]^{1/2} \quad (122)$$

and the normal velocity of the fuel vapor pocket is

$$v_{fv} = v_g - V_{rel} \cos \Phi \quad (123)$$

The mean rate of mass transfer is

$$\dot{m} = h_D A \Delta C_v \quad (124)$$

The mean rate is also

$$\dot{m} = m / \tau_{fv} \quad (125)$$

Thus, the lifetime of the fuel vapor pocket is

$$\tau_{fv} = \frac{m}{h_D A \Delta C_v} \quad (126)$$

The surface coefficient of mass transfer is usually expressed in terms of the Sherwood number ($Sh = h_D d_{fv} / D_g$). Therefore, recognizing that the concentration difference is ρ_{fv} , Eq. (126) can be rewritten in the following form

$$\tau_{fv} \propto \frac{d_{fv}^2}{D_g} \frac{1}{Sh} \quad (127)$$

Comparison of Eq. (127) with Eq. (86) shows that the Sherwood number is a generalizing parameter for the lifetime of the pocket.

The thickness of the gas phase reaction zone is obtained by substituting Eqs. (85), (122), (123), and (127) into Eq. (119). This yields

$$\delta_r'' = C_1 \frac{d_{fv}^2}{D_g} Sh^{-1} \left\{ \frac{r_b \rho_p}{\rho_g} - C_2 \left[\frac{a d_{fv} \Delta \rho}{\rho_g C_d} \right]^{1/2} \cos \Phi \right\} \quad (128)$$

The burning rate can be related to the thickness of the gas phase reaction zone by combining Eqs. (81) and (82). This yields ($\delta_r'' = \delta_r$ in the high pressure limit)

$$r_b = \frac{\lambda_g (T_f - T_s)}{\delta_r \rho_p [c_p (T_s - T_i) - Q_s]} \quad (129)$$

Therefore,

$$r_b = \left\{ \frac{\lambda_g (T_f - T_s)}{\rho_p [c_p (T_s - T_i) - Q_s]} \frac{D_g}{d_{fv}^2} \right\} \frac{C_1 Sh}{\frac{r_b \rho_p}{\rho_g} - C_2 \left[\frac{a d_{fv} \Delta \rho}{\rho_g C_d} \right]^{1/2} \cos \Phi} \quad (130)$$

When the acceleration approaches zero, the burning rate approaches its static value $(r_b)_{a=0}$. Therefore, in Eq. (130), the terms in braces must be $(r_b)_{a=0}^2 \rho_p / (\rho_g C_1 Sh_0)$ where Sh_0 denotes the limiting value for the Sherwood number as the acceleration approaches zero. Employing this result and expanding Eq. (130) yields with some rearrangement

$$\left[\frac{r_b}{(r_b)_{a=0}} \right]^2 - \left\{ \frac{C_2 \rho_g}{(r_b)_{a=0} \rho_p} \left(\frac{a d_{fv} \Delta \rho}{\rho_g C_d} \right)^{1/2} \cos \Phi \right\} \left[\frac{r_b}{(r_b)_{a=0}} - \frac{Sh}{Sh_0} \right] = 0 \quad (131)$$

Therefore, the burning rate ratio can be obtained by employing the quadratic formula. However, before performing this operation, define a Grashof number built upon the characteristic dimension of the fuel vapor pocket as

$$Gr_d = \frac{\rho_g a \Delta \rho d_{fv}^3}{\mu_g^2} \quad (132)$$

and a Reynolds number as

$$Re_o = \frac{(r_b)_{a=0} \rho_p d_{fv}}{\mu_g} \quad (133)$$

It is seen that the term in braces in Eq. (131) is exactly $C_2 (Gr_d / Re_o^2)^{1/2} \cos \Phi$. Therefore, since the burning rate ratio must be positive

$$\frac{r_b}{(r_b)_{a=0}} = C_3 \frac{Gr_d^{1/2} \cos \Phi}{C_d^{1/2} Re_o} + \left[C_3^2 \frac{Gr_d \cos^2 \Phi}{C_d Re_o^2} + \frac{Sh}{Sh_0} \right]^{1/2} \quad (134)$$

Dimensional analysis suggests that

$$C_d = \text{function} (Re_{rel}) \quad (135)$$

and

$$Sh = \text{function} (Re_{rel}, Sc_g) \quad (136)$$

where $Re_{rel} = \rho_g V_{rel} d_{fv} / \mu_g$. The form of the functions will depend largely upon the magnitude of the Reynolds number.

The relative velocity in the case where the acceleration force is normal to and into the burning surface of the propellant ($\ddot{x} = 0$) cannot exceed v_g . A basic postulate of the granular diffusion flame model is that the mass of the fuel pocket in the solid will be much less than the mass of a mean oxidizer particle. Moreover, the mass of the pocket is invariant with pressure; therefore,

$$O(d_{fv}) < d_{ox} \left[\frac{\rho_p}{\rho_g} \right]^{1/3} \quad (137)$$

and the order of magnitude of the Reynolds number Re_{rel} will be

$$O(Re_{rel}) < \frac{r \rho_p d_{ox}}{\mu_g} \left[\frac{\rho_p}{\rho_g} \right]^{1/3} \quad (138)$$

Substitution of the values found in Table C-I into Eq. (138) shows that the Reynolds number cannot greatly exceed 20. Therefore, for small accelerations, the flow should be dominated by viscous forces.

For the Stokes flow regime, Redfield and Houghton⁽³⁴⁾ have found that the drag coefficients for single bubbles in a liquid obey the relationship

$$C_d \propto Re_{rel}^{-1} \quad (139)$$

They also report that this relationship is obeyed for liquid-liquid drop systems. The mass transfer results of Redfield and Houghton are scattered for the low Reynolds

number regime. Therefore, a relationship for solid spheres, which has the correct asymptotic form as Re_{rel} approaches zero will be employed

$$Sh = Sh_0 + 0.57 Re_{rel}^{0.5} Sc_g^{0.35} \quad (140)$$

where $Sh_0 = 2$.

The relative velocity can be obtained by substituting Eq. (139) into Eq. (122) or

$$V_{rel} = C_4 \frac{a d_{fv}^2 \Delta \rho}{\mu_g} \quad (141)$$

Therefore, the drag coefficient is

$$C_d = C_4^{-1} Gr_d^{-1} \quad (142)$$

Substitution of Eqs. (140) and (142) into Eq. (134) yields

$$\frac{r_b}{r_{b \ a = 0}} = C_5 \frac{Gr_d}{Re_0} \cos \Phi + \left[\left[C_5 \frac{Gr_d}{Re_0} \cos \Phi \right]^2 + 0.28 Gr_d^{1/2} Sc_g^{0.35} + 1 \right]^{1/2} \quad (143)$$

Equation (143) should be valid for an acceleration range where $Gr_d < 10$. For accelerations that exceed this criteria, Eq. (143) will fail because the drag coefficient becomes a function of the size of the bubble as well as the properties of the fluids. Unfortunately, neither empirical correlations nor valid theoretical analyses are available for this regime. This precludes the analytical development of a specific equation for the burning rate ratio for the regime where $Gr_d > 10$.

RESULTS AND DISCUSSION

PHASE I - INTERNAL GAS DYNAMICS

The effect of spin on the head end pressure of a rocket motor with a single nozzle and a CP grain configuration was investigated. The rocket motor geometry was characterized by a grain that was 20 inches long and a single nozzle with $d^* = 1.5$ in. The effect of acceleration on burning rate was accounted for by employing the assumed variation for $\alpha_t/(\alpha_t)_{a=0}$ shown by Figure 11.

Figures 12 and 13 show the effect of spin on head end pressure¹ for the motor considered when the port diameter is 1.8 and 4.0 in., respectively. Results are presented for the following condition: (1) spin induced changes in burning rate, (2) spin induced changes in burning rate and nozzle flow, and (3) spin induced changes in burning rate, nozzle flow, and port flow. The figures show that for the lower spin rates the only noticeable effect is caused by spin induced changes in burning rate and that for all spin rates the effect due to spin induced changes in the port flow is small. In addition, Figure 12 shows that head end pressure changes caused by spin induced changes in the internal flow field of the motor is small--even at very large spin rates. However, Figure 13 shows that spin induced changes in the nozzle flow are very large at high spin rates.

These results presented suggest that at the acceleration levels of interest to this study the primary spin effects in single nozzle motors with CP grains are connected with acceleration induced changes in burning rate and spin induced changes in the nozzle flow and that the former is the most important.

PHASE II - EFFECT OF ACCELERATION ON BURNING RATE

Review of the Literature

A review of the literature has shown that it can be put into the following general categories: literature concerning qualitative spin effects and literature concerning quantitative spin effects. The literature in the first category consists mainly of pressure-time and thrust-time histories of rocket motors. However, because of the unknown magnitude of effects due to internal ballistic changes and non-uniform surface regression when the burning rate is dependent upon the orientation of the burning surface, these data cannot be reduced to the point where the burning rate can be defined as a function of its independent variables. Since this study was concerned with the relationship between the burning rate and its independent variables, these data are of little value and will not be reviewed herein. This literature comprises References 1 through 23.

The literature in the second category is composed of literature directed at the effects of acceleration on the burning rate of double-base solid propellants, metallized composite propellants, and nonmetallized composite propellants. The physical structure of double-base propellants and, consequently, their combustion phenomena are

-
1. These results were obtained with a special computer program that is limited to geometries with $r_0 = \text{constant}$.

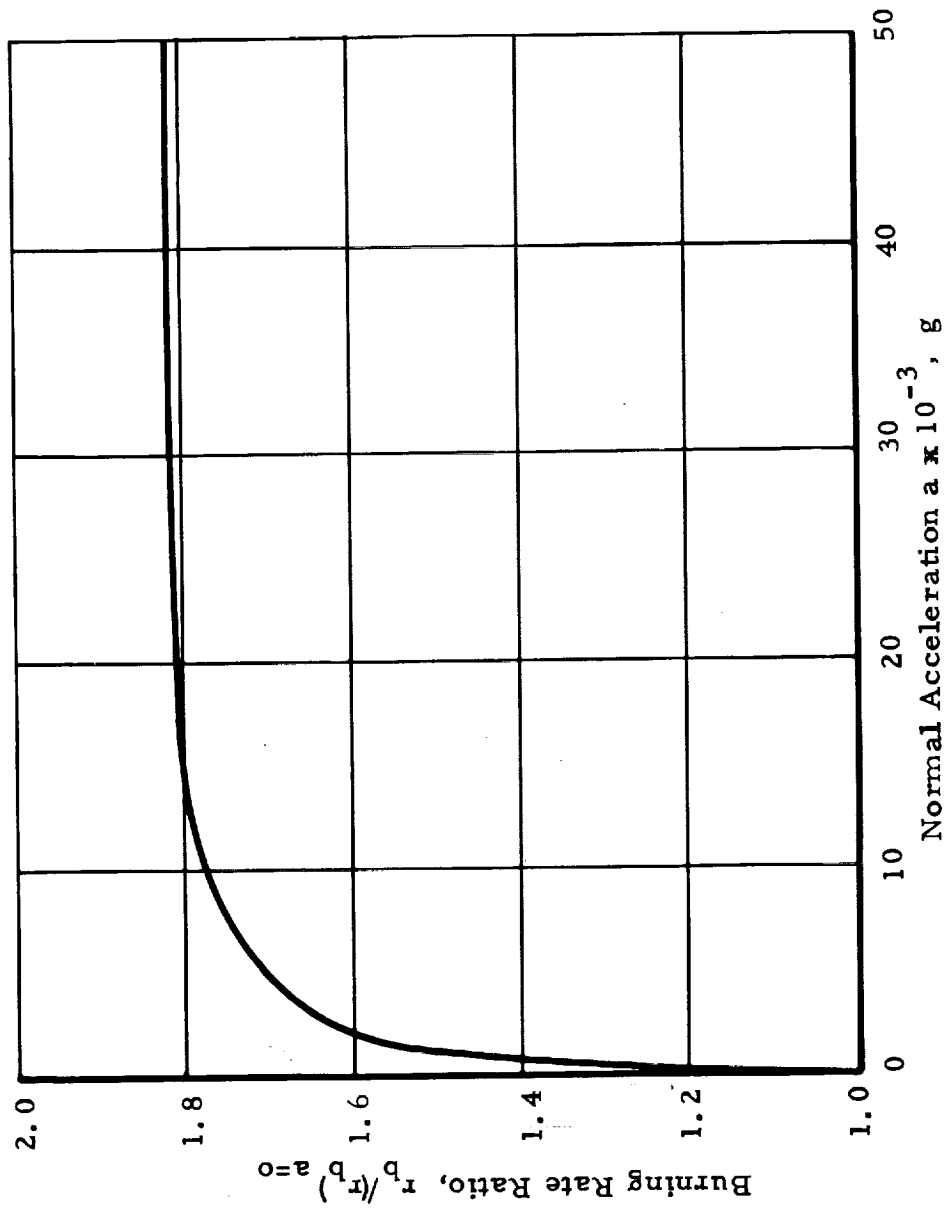


Figure 11. Assumed Effect of Acceleration on Burning Rate.

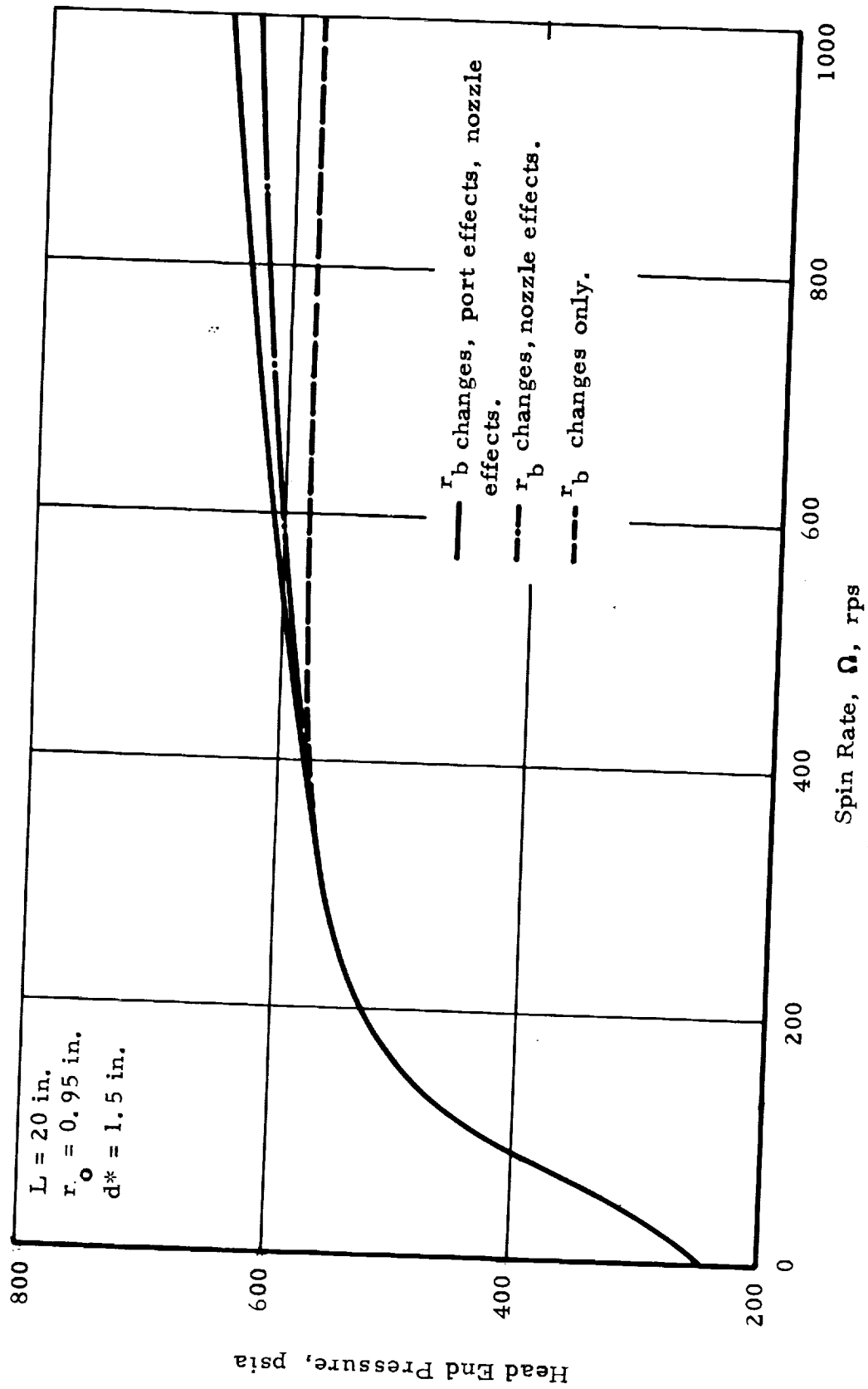


Figure 12. Effect of Spin on Head End Pressure When $\pi r_o^2 \approx A^*$.

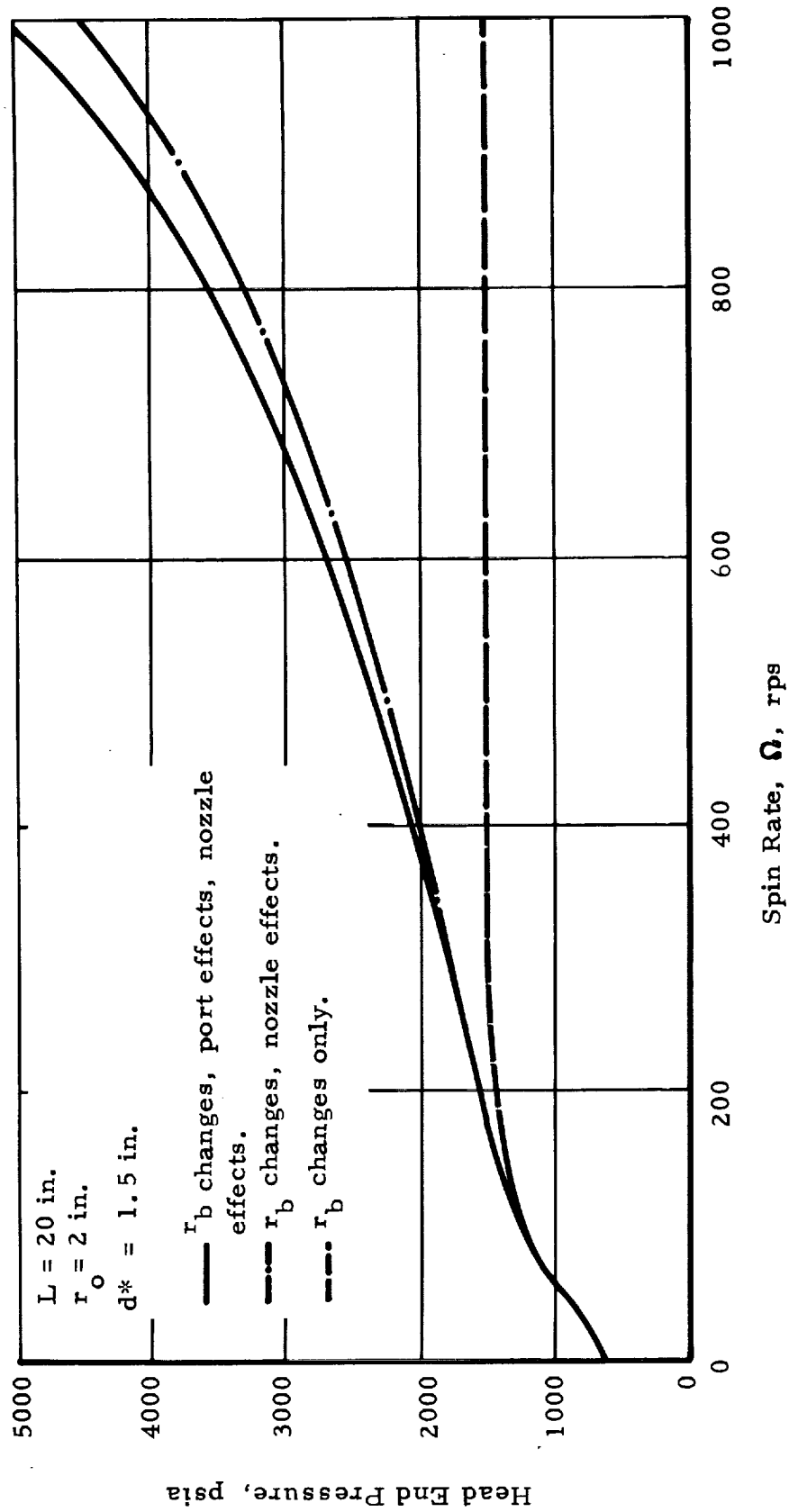


Figure 13. Effect of Spin on Head End Pressure When $\pi r_o^2 > A^*$.

different than those of composite propellants. Therefore, literature that pertains to double-base propellants will not be reviewed. As mentioned previously, the combustion phenomenon of metallized and nonmetallized composite propellants in an acceleration field is different. Therefore, the literature pertaining to these metallized and non-metallized propellants will be reviewed separately.

Metallized Propellants

The quantitative literature that pertains to metallized propellants that is unclassified consists of References 28, 31, and 35-37. These references will be reviewed in turn.

Reference 28 has investigated the effect of acceleration on burning rate of a metallized PBAN-AP propellant in the range from 0 to 120 g with a single nozzle motor that was spun about its axis of symmetry. The motor had a CP grain with 4.5 in O. D. and 0.6 in. web; the ends were tapered to achieve a neutral area web trace. The instantaneous burning rate was computed from the chamber pressure via a mass balance and was corrected to the base point pressure by assuming that the pressure exponent was unchanged by the acceleration. The propellant variables investigated were oxidizer particle size, metal additive particle size, metal content, and additive composition. The results of the tests showed that burning rate varied with time during each test. In general, the burning rate increased with time and tended toward an asymptotic limit. However, in a few tests burning rate decreased with time. In one test the burning rate decreased through the firing; in several tests the burning rate first increased and then decreased as the web was approached.

It was also found that acceleration effects were reduced by decreasing the oxidizer particle size, decreasing the particle size of the metal additive, and decreasing the metal content. In addition, it was found that a refractory metal (tungsten) also produced appreciable burning rate increases. Visual examination of the residue showed that no agglomeration had occurred and that there was no appreciable chemical reaction.¹ This suggests that acceleration induced burning rate changes can be produced by a mechanism other than metal combustion at the propellant surface. Moreover, when the theoretical results were compared with the experimental results, it was found that the a_c required was far less than the theoretical a_c for the additive. This indicated that a pre-agglomeration of the metal particles took place before escape from the surface and final agglomeration in the pit. Figure 14 presents the effect of acceleration on the mean burning rate of an aluminized propellant with PBAN binder.

Reference 31 has investigated the effect of acceleration in the range from 0 to 300 g on the burning of an aluminized PBAA-AP composite propellant in a special slab burner. The slab burner had a web thickness of 0.5 inch and was mounted on an arm centrifuge so that the angle between the acceleration force and the burning surface could be varied. The study showed that acceleration affects both the burning rate coefficient and the pressure exponent (Figure 15) and that burning rate at any acceleration level depends upon the orientation of the burning surface relative to the acceleration forces. In addition, it was found that the amount of residue retained in the motor after firing was

1. Personal communication with P. G. Willoughby.

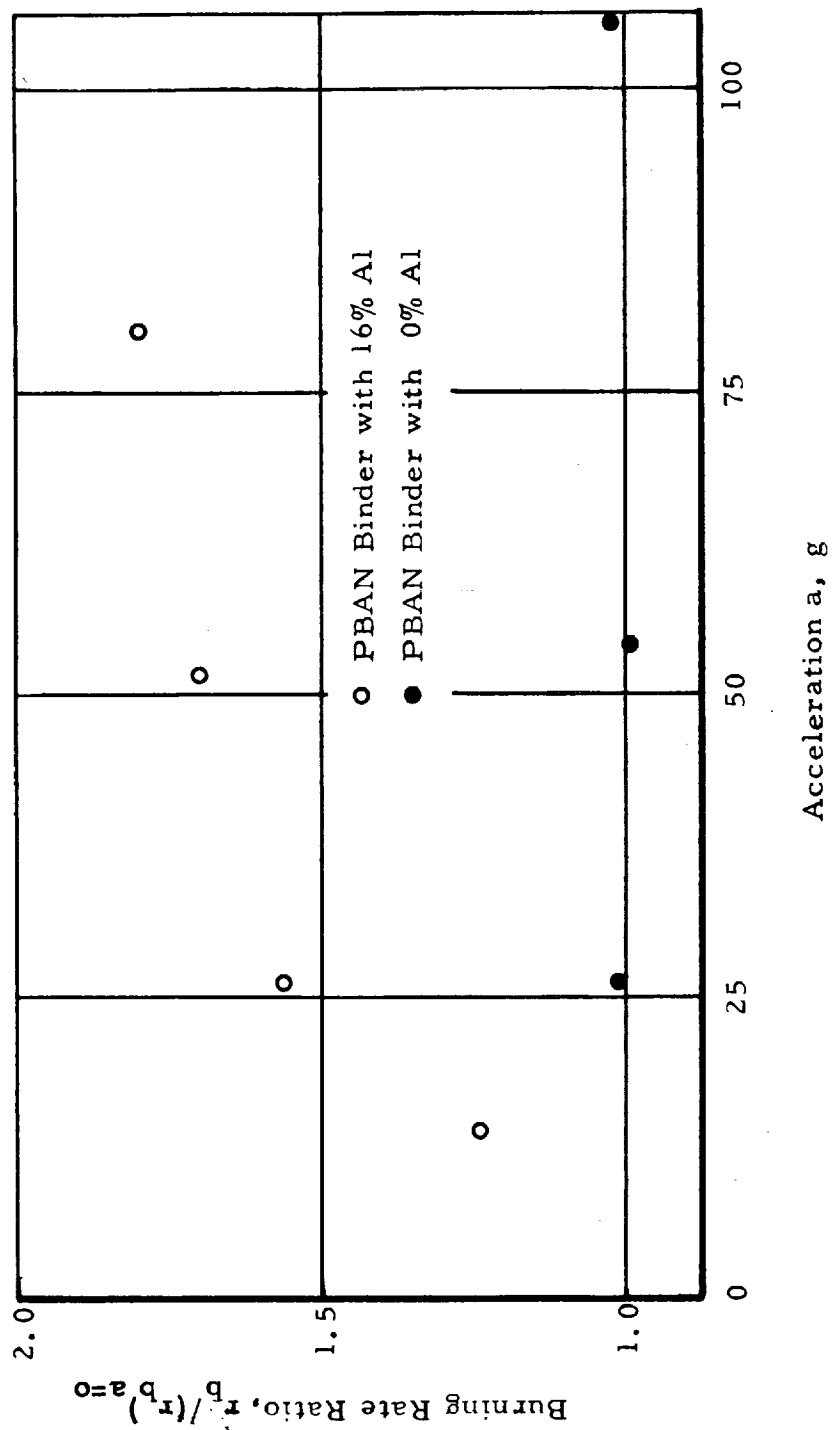


Figure 14. Effect of Acceleration on the Burning Rate of Aluminized and Nonaluminized Composite Propellants (Reference 28).

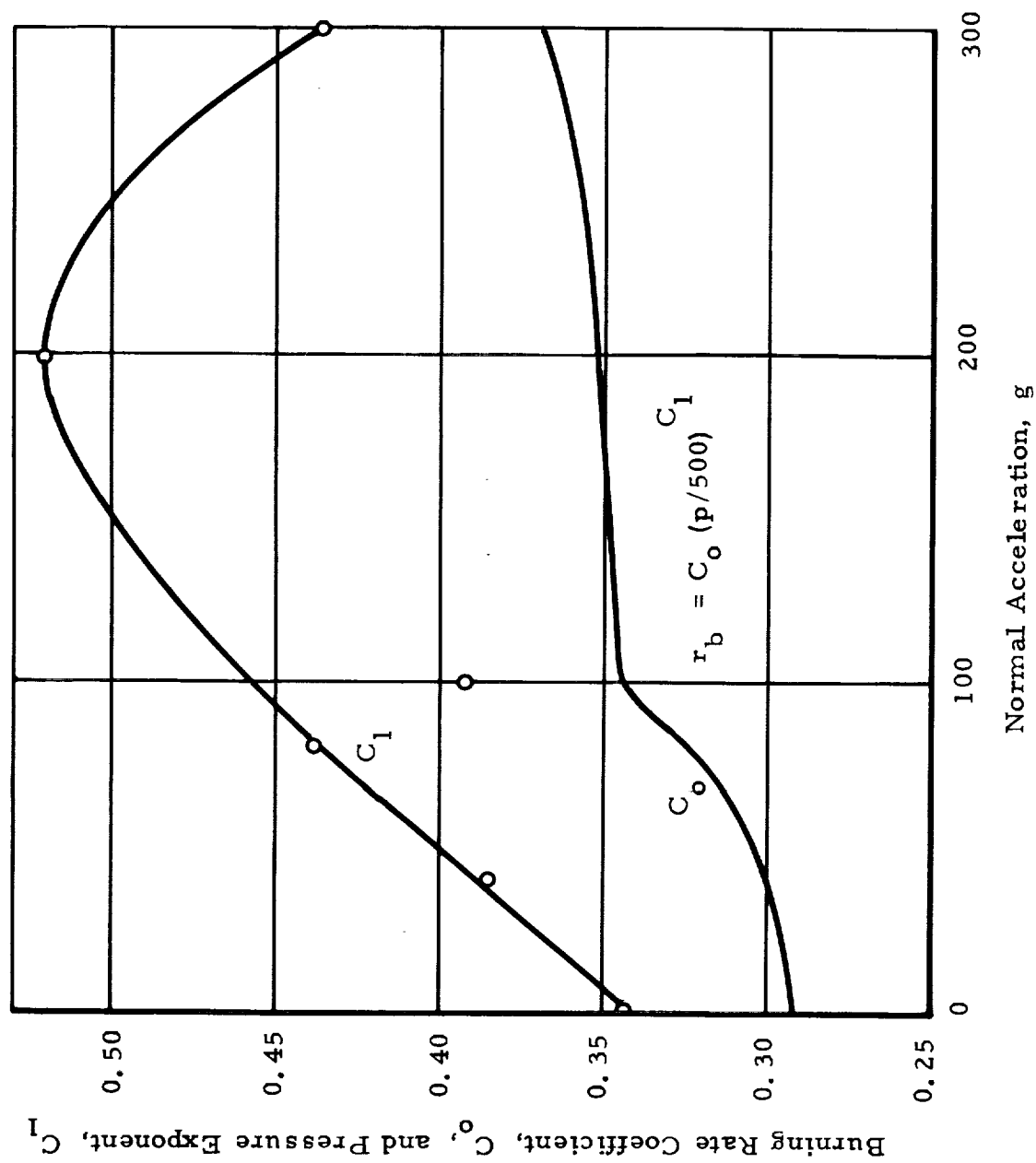


Figure 15. Effects of Acceleration on the Burning Rate Constant and Pressure Exponent (Reference 31).

related to the acceleration level. A sieve analysis showed that the mean size of the residue was also related to the acceleration level and that the mean residue size increased as the acceleration level increased (Figure 16). Moreover, the normalized size distribution of the residue is essentially independent of the acceleration level and is that for the aluminum additive (Figure 17).

Reference 37 has investigated the effect of acceleration on burning rate with a strand burner mounted on the arm of a centrifuge. The study investigated several different aluminized AP propellants with PBAN and Polyurethane binders at acceleration levels from 0 to 2000 g; the acceleration force was always normal to and into the burning surface. Figure 18 illustrates typical results. The results of the tests showed that the burning rate increased rapidly as the magnitude of the acceleration increased tending to an asymptotic value at the higher acceleration levels. In addition, it was found that the pressure exponent of the PBAN propellant was relatively insensitive to acceleration¹ while that of the Polyurethane propellant was quite sensitive. Residue was found in the case that enclosed the strand. At acceleration levels above 300 g, the residue was present as a single piece whose thickness increased with the acceleration level. X-ray diffraction analysis showed that the residue was aluminum oxide. The burning rate data for the PBAN binder with 17% of 7.1 μ aluminum was correlated by the equation

$$r_b/(r_b)_{a=0} = 1 + 0.028 a^{0.30} \quad (144)$$

while the burning rate data for the Polyurethane binder with 17.7% of 31 μ aluminum was correlated with the equation

$$r_b/(r_b)_{a=0} = 1 + C_1 \left[a p/(r_b) \right]^{C_2} \quad (145)$$

where C_1 and C_2 are pressure dependent.

Reference 35 reported test results for small rocket motors with CP and six pointed star grains. In the tests the pressure was approximately 600 psi, the acceleration ranged from 0 to 100 g, and the acceleration force was parallel to the burning surface. The test results showed no acceleration effects.

Reference 36 has reported test results for both small and moderate sized rocket motors containing aluminized composite propellant with CP grains. The tests were performed on an arm centrifuge and the acceleration vector was either parallel to or normal to the axis of the motor. The tests covered the pressure range from 1,000 to 2,000 psi and acceleration levels from 0 to 200 g. Regression analysis of the test results showed no effects that were attributable to acceleration.

Reference 38 presents results derived from micromotor tests on an arm centrifuge with UTX-2649 propellant containing 16% aluminum. The acceleration range from

1. This supports the data reduction procedure of Reference 28.

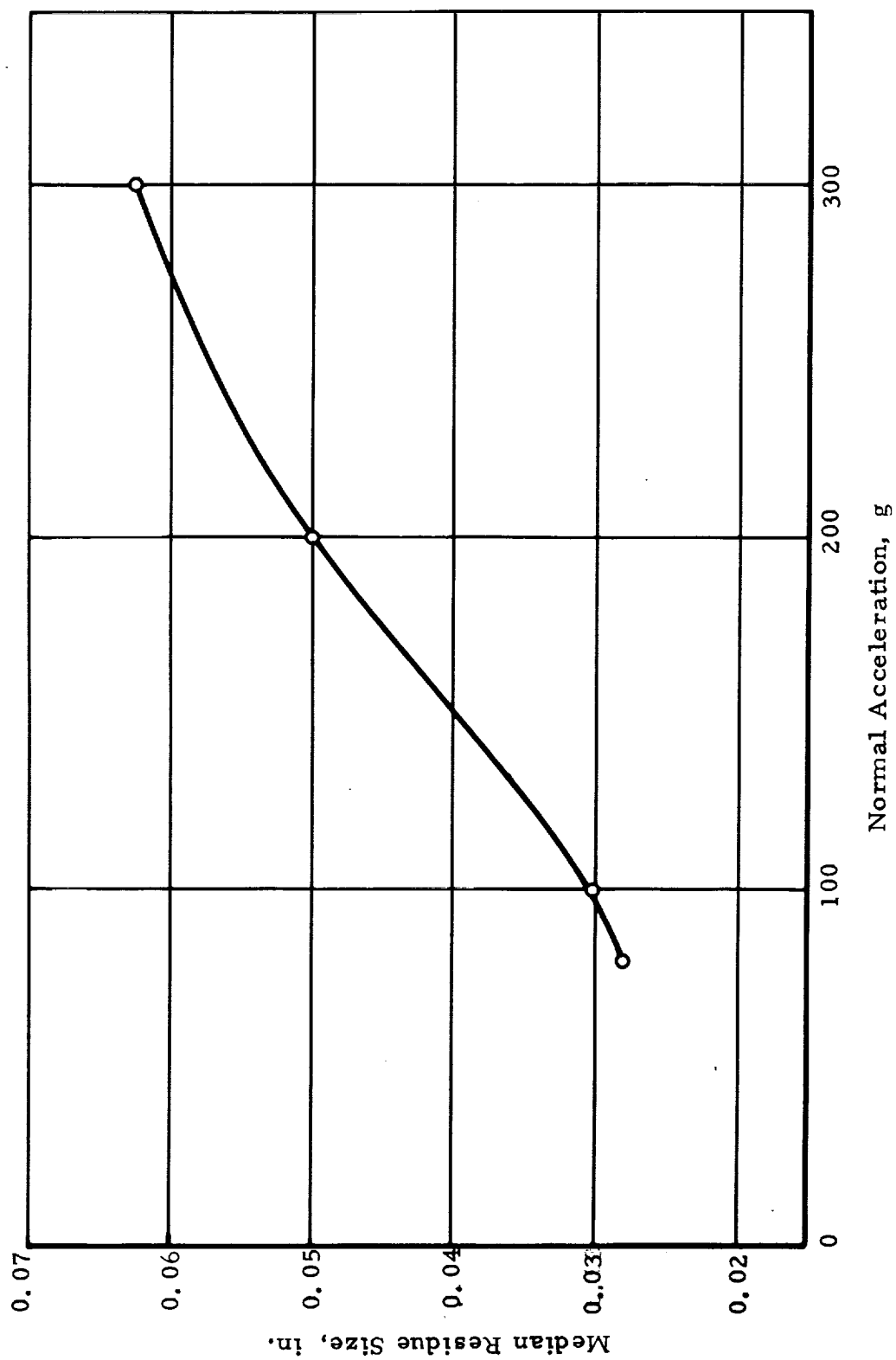


Figure 16. Effect of Normal Acceleration on Median Residue Size (Reference 31).

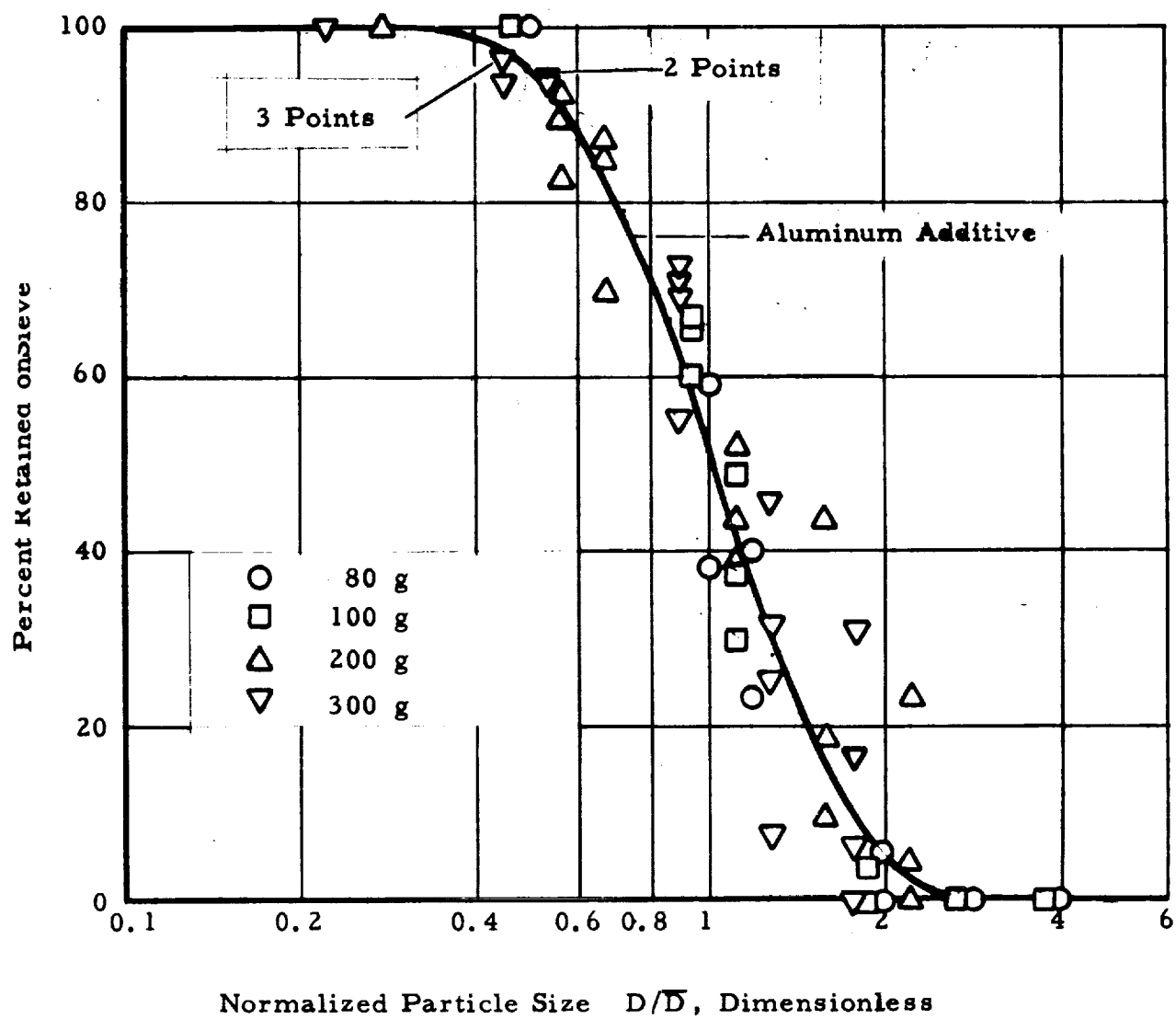


Figure 17. Residue Size Distribution (Data Reference 31).

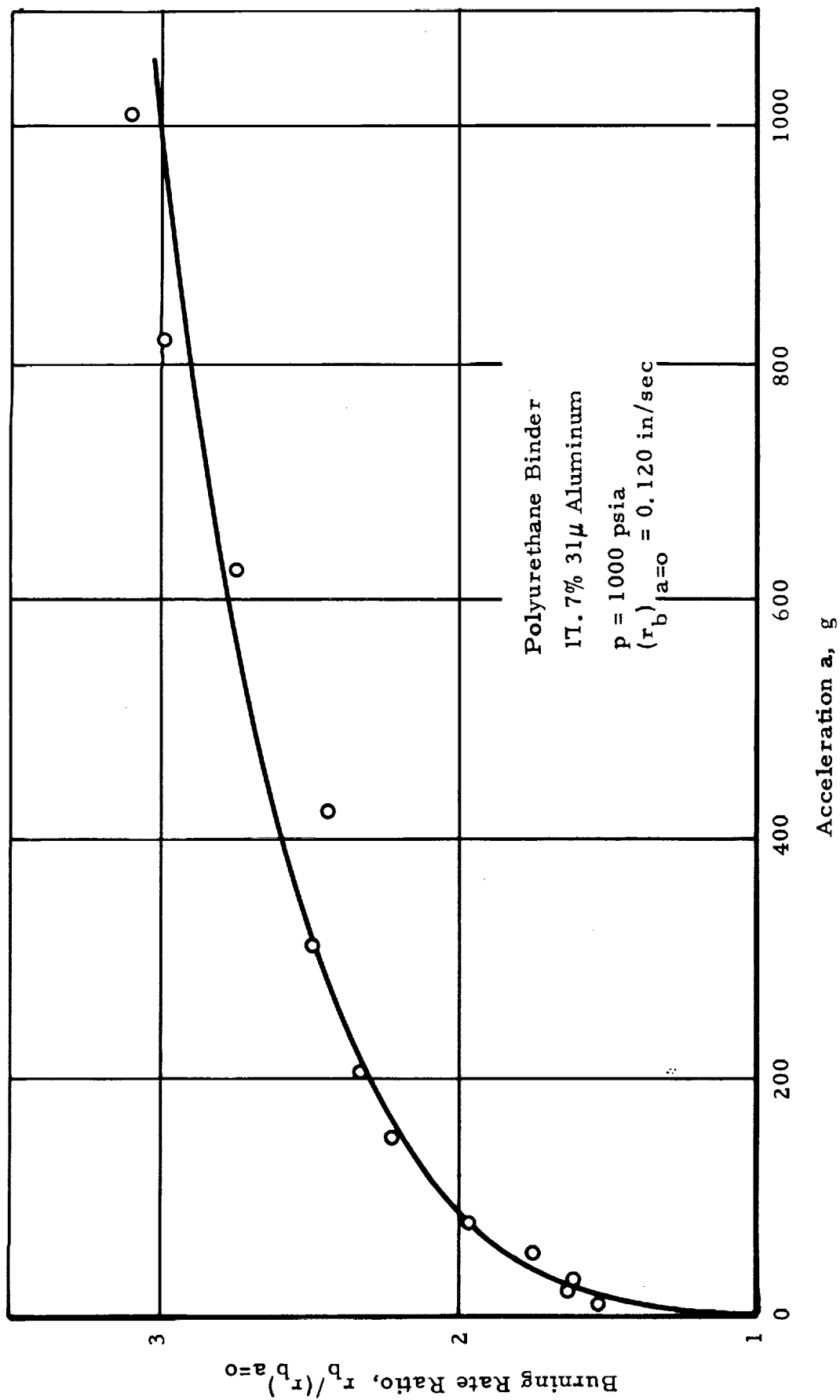


Figure 18. Effect of Acceleration on the Burning Rate of a Metallized Composite Propellant. (Reference 37)

0 to 800 g was studied at pressure levels of 1,000 and 2,000 psi; in all cases the acceleration force was parallel to the burning surface. The tests showed no consistent change in burning rate with acceleration level.

The experimental results suggest the following general trends:

1. Acceleration induced burning rate changes are largest when the acceleration force is normal to and into the burning surface.
2. Acceleration induced burning rate changes are negligible when the acceleration force is parallel to or away from the burning surface.
3. Acceleration induced burning rate changes can be reduced by reducing the metal content, metal particle size, and the oxidizer particle size.
4. Acceleration can affect the pressure dependency of burning rate and this effect depends upon the binder.
5. Acceleration induced burning rate changes occur irrespective of the reactivity of metal additive.

Nonmetallized Propellants

The quantitative literature relating to the effects of acceleration on the burning rate of nonmetallized composite propellants consists of References 24, 25, and 28 and References 38 through 42. References 25, 40, 41, and 42 are classified and therefore will not be reviewed herein. However, Reference 25 has been reviewed by Reference 24; Reference 42 has been reviewed by Reference 31; and the pertinent data in References 40 and 41 are for pressures below the range considered here. The remaining references are reviewed in the following paragraphs.

Reference 38 has tested micromotors with CP grains on an extended arm centrifuge. In all cases, the acceleration force vector was parallel to the surface of the propellant and in the direction of gas flow. The tests were conducted at nominal chamber pressures of 1,000 and 2,000 psia and at acceleration levels up to 800 g at 200 g intervals. Two different propellants, UTX-1724 and UTX-2649, were tested. The test data were somewhat scattered; however, there was no indication of an appreciable effect of acceleration on burning rate. The essentially null effect observed at two different pressures indicates that neither the burning rate coefficient α_t nor the pressure exponent n in the burning rate law $r_b = \alpha_t p^n$ are strongly dependent on acceleration in the range of the test.

Reference 28 has static spin tested small rocket motors with a PBAN propellant. The grain configuration used was an axisymmetric internal burner with inhibited wedge shaped ends to provide a neutral trace and maintain the burning surface so that the acceleration vector is always normal to and into the burning surface. The nominal chamber pressure was 600 psia and the acceleration level ranged from 0 to approximately 120 g. Figure 14 presents the experimental results and shows that there were no appreciable effects.

Reference 24 has reviewed the data of Wall⁽²⁵⁾ which showed that the pressure exponent n of the burning rate law $r_b = \alpha_t p^n$ was not influenced by spin, but that the burning rate coefficient α_t was dependent upon the configuration of the grain for a spinning rocket motor. Reference 24 has also correlated the variation of α_t with grain configuration found by Wall by employing the following variables: dimensionless burning rate coefficient $\alpha_t/(\alpha_t)_{a=0}$ and the grain complexity factor $X = C/(4\pi A_c)$. The correlation showed that $\alpha_t/(\alpha_t)_{a=0} = a X^b$ where a and b are constants and b is negative. Thus, increasing the grain complexity factor reduces mean acceleration effects. In addition to the above, Reference 24 showed that the effect of spin induced grain deformations on the performance of the motor was, at most, a secondary effect.

Reference 37 has investigated the effects of acceleration on the burning rate of propellants with polyurethane and PBAN binders. The investigation was performed with strands mounted in a bomb. The bomb was attached to the end of a 3-foot long centrifuge arm. In all tests, the acceleration was normal and into the burning surface. The tests were conducted at pressures of 500, 1,000, and 1,500 psia and at acceleration levels up to 2,000 g. Figures 19 and 20 illustrate the effects of acceleration on the burning rate ratio $r_b/(r_b)_{a=0}$ of the polyurethane propellant at pressures of 1,000 and 1,500 psia. The results suggest that there is a very large effect at relatively small accelerations ($a < 200$ g). However, the large effects occurred in the tests where the wire employed to ignite the stand broke during the test. The large increases in burning rate measured with the wire broken were attributed to the retention of a portion of the broken wire on the burning surface. This explanation appears reasonable because the burning rate of a metallized composite propellant is more sensitive to acceleration than a nonmetallized propellant (Figure 14) and metal and/or metal oxide is certainly retained on the burning surface of a metallized propellant. The large deviation between the data points where the wire was intact should also be noted. This suggests that considerable experimental error existed.

Figures 21, 22, and 23 illustrate the effects of acceleration on the burning rate ratio of PBAN propellant at pressures of 500, 1000, and 1500 psia. These results show the following: appreciable acceleration effects occur for accelerations as low as 500 g, the burning rate is essentially unaffected by accelerations under 100 g, burning rate is highly dependent upon acceleration for $100 < a < 300$ g, and the burning rate appears to approach an upper limit at very large accelerations. The insensitivity of burning rate to acceleration at accelerations below 100 g is supported by Reference 28.

Figure 24 is a composite plot of all of the data at 500, 1,000, and 1,500 psia for which the ignition wire remained intact. The figure shows that the variation of the burning rate ratio with acceleration is essentially the same at all three pressures. This indicates that the pressure exponent n is not strongly dependent upon the magnitude of the acceleration. The insensitivity of the pressure exponent to acceleration level is supported by the data of Reference 25.

In summary, the review of the literature that is pertinent to the effects of acceleration on the burning rate of nonmetallized composite propellants has shown that no previous theoretical analyses exist and that the available experimental data do not adequately cover the independent variables involved and their ranges of interest. Moreover, the majority of the data is derived from strand tests (Reference 37). It is well known that strand burning rates differ from motor burning rates. Therefore,

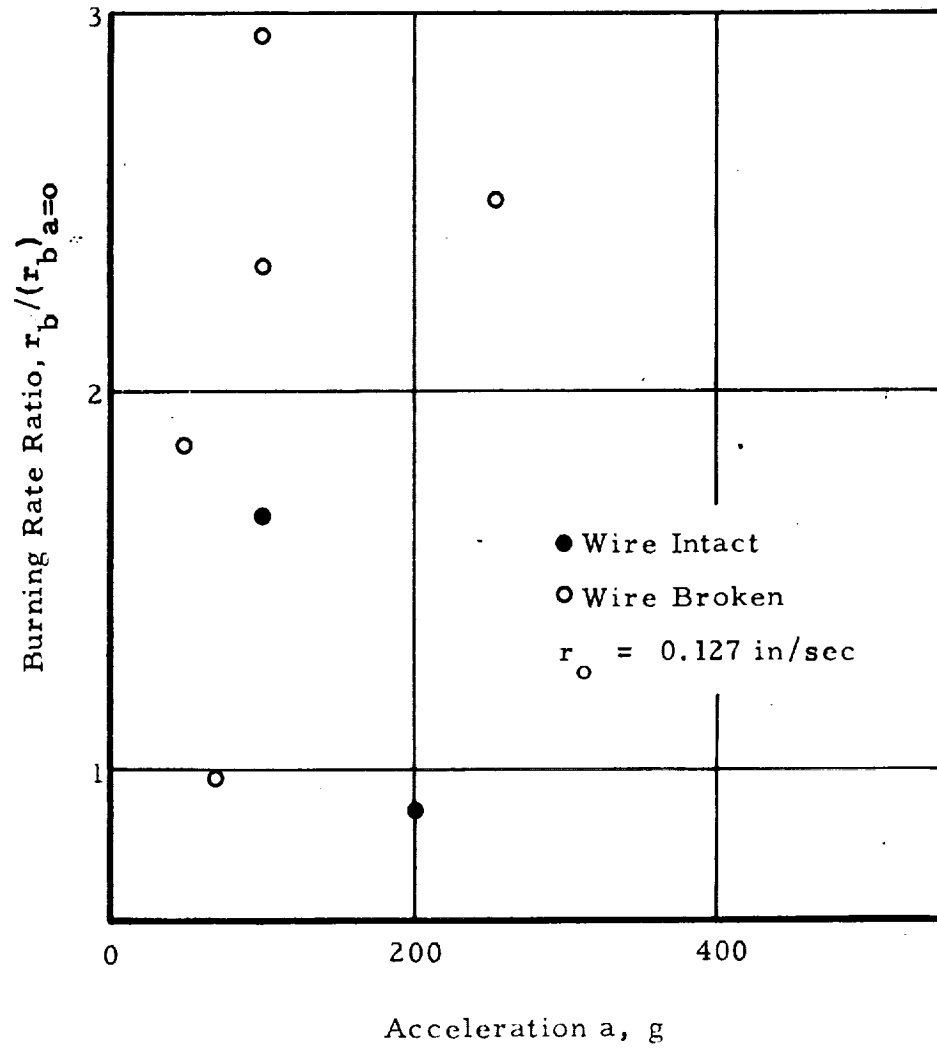


Figure 19. Effect of Acceleration on the Burning Rate of a Polyurethane Propellant at 1000 psia (Reference 37).

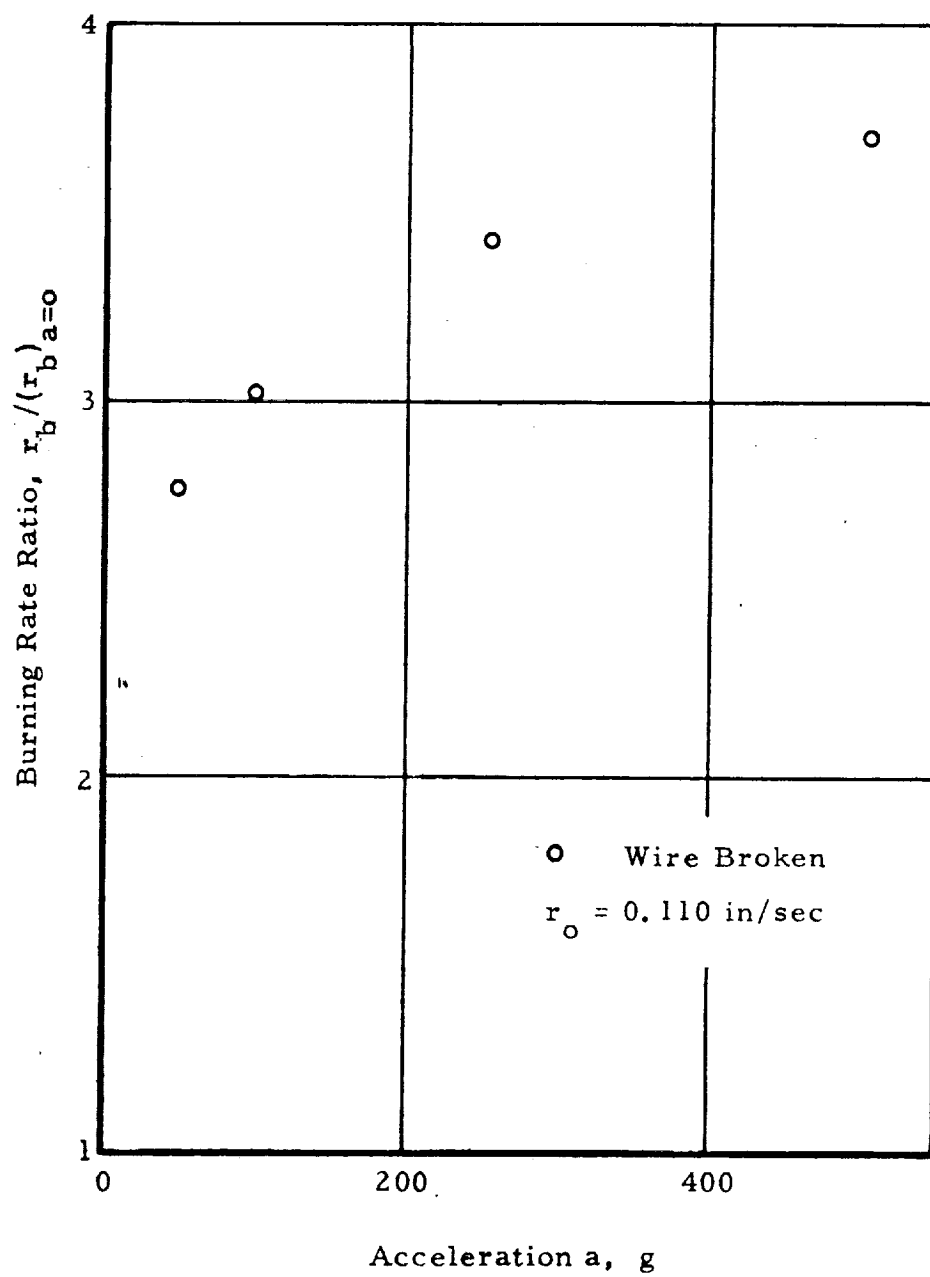


Figure 20. Effect of Acceleration on the Burning Rate of Polyurethane Propellant at 1500 psia (Reference 37).

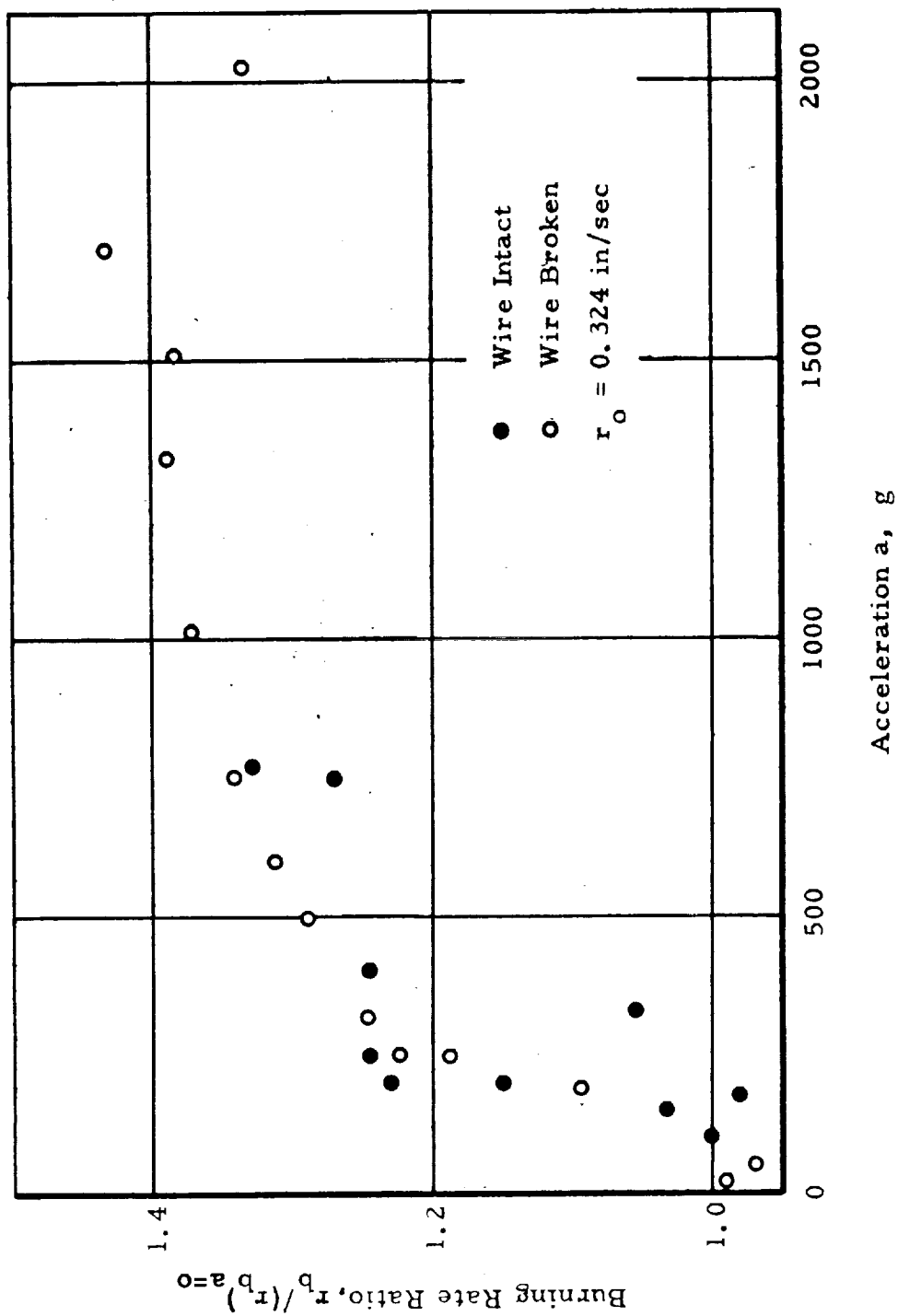


Figure 21. Effect of Acceleration on the Burning Rate of PBAN Propellant at 500 psia (Reference 37).

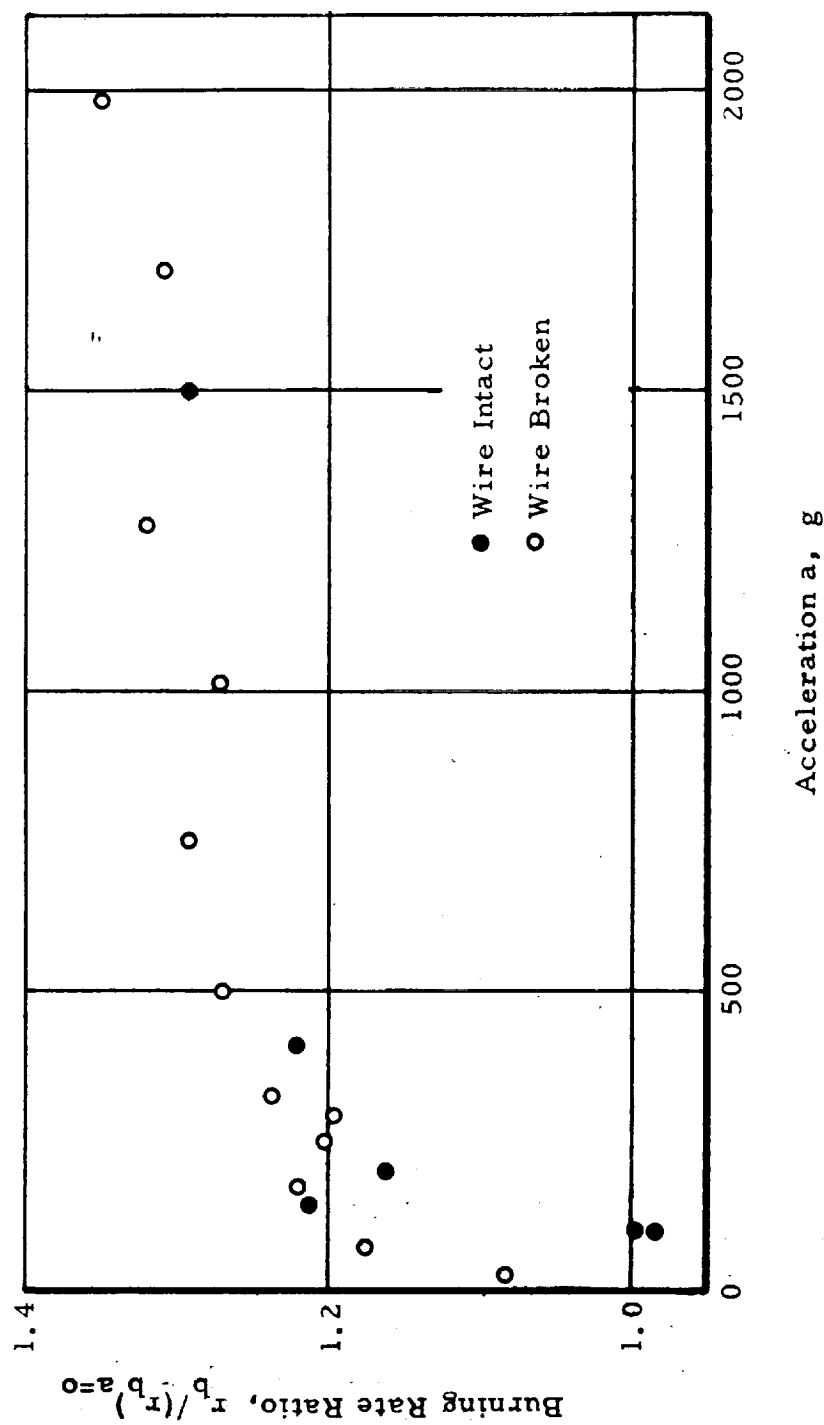


Figure 23. Effect of Acceleration on the Burning Rate of PBAN Propellant at 1500 psia (Reference 37).

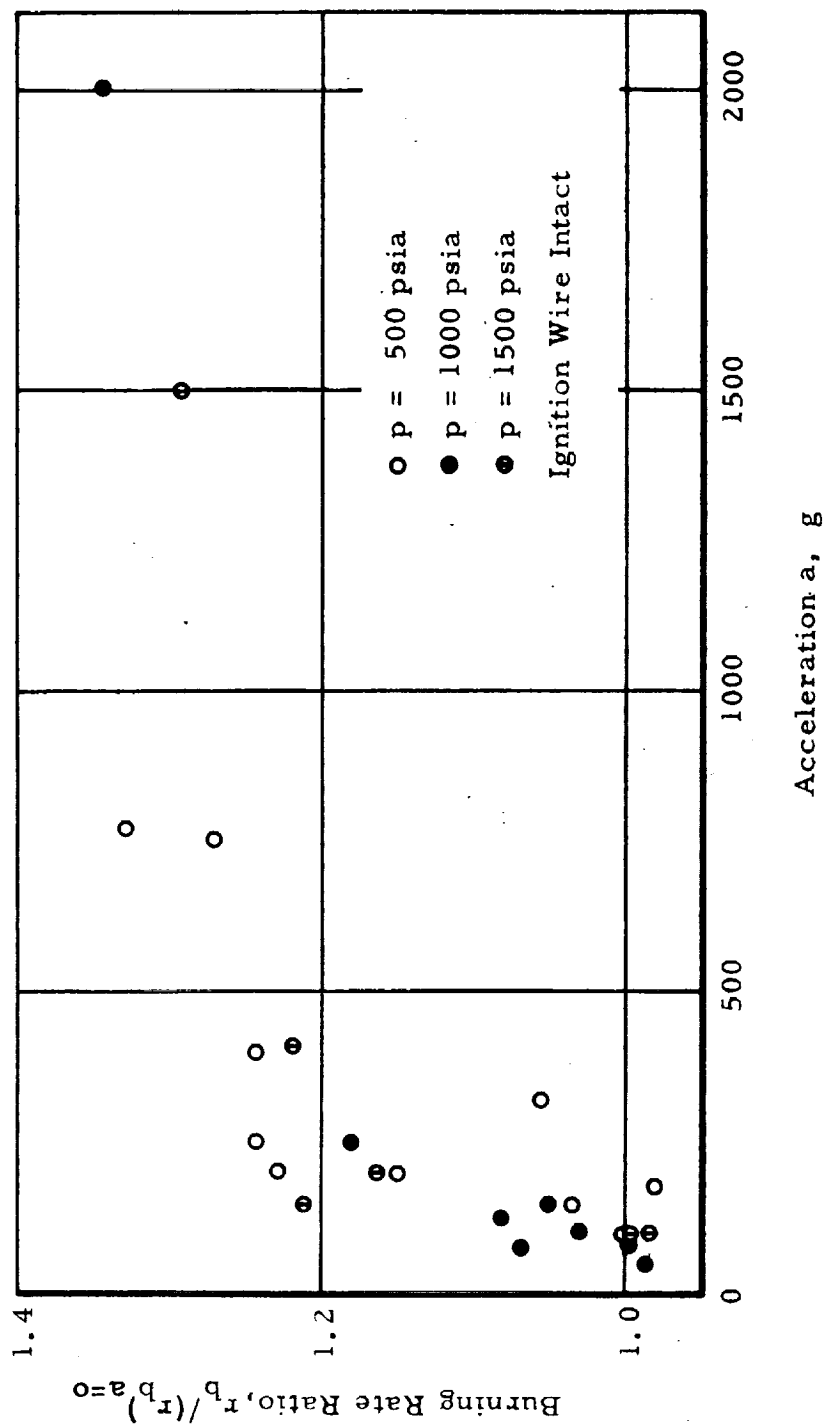


Figure 24. Comparison of Burning Rate Data at 500, 1000, and 1500 psia (Data Reference 37).

motor data confirming the trends shown by the data of Reference 37 are necessary before complete confidence can be placed in them. However, the experimental data do suggest the following trends.

1. The effect of acceleration on burning rate is small for accelerations less than 100 g.
2. Acceleration effects depend upon the direction of the acceleration vector relative to the burning surface.
3. When the acceleration vector is parallel to the burning surface, the effect of acceleration on burning rate is small.
4. When the acceleration vector is normal to and into the burning surface, appreciable increases in burning rate can occur.
5. When the acceleration vector is normal to and into the burning surface, the burning rate approaches an upper limit as the acceleration level increases.
6. The burning rate ratio is essentially independent of pressure.

Comparison of Theory and Experiment

Metallized Propellants

The general characteristics of the analytical model will be examined first. The theory developed in the ANALYSIS shows that the burning rate ratio is a function of the following variables: Π , β , σ , Φ and $(a p / r_b) / (a p / r_b)_c$. The latter variable contains the acceleration term so it will be treated as the independent variable and the other variables will be treated as parameters. Figure 25 illustrates the variation of the burning rate ratio with $(a p / r_b) / (a p / r_b)_c$ for the parameter values specified. The figure shows that the burning rate ratio increases asymptotically to a maximum value and that the way the asymptotic value is reached is dependent upon the variance of the particle distribution σ . When σ is small the asymptote is reached in a steep step; when σ is large the asymptote is reached in a more gradual step. Figure 25 also compares the theory developed herein with the theory developed by Reference 28. The comparison shows that, for the conditions shown, the two theories are essentially equivalent for small values of the independent variable when $\sigma = 0.46$; however, the new theory reaches the asymptotic value sooner. Moreover, the theoretical results of Reference 28 are not as strongly dependent upon the variance of the particle distribution as the new results are.

Most of the available experimental results present the burning rate ratio as a function of acceleration. Therefore, the independent variable a/a_c is desired rather than the variable $(a p / r_b) / (a p / r_b)_c$. This transformation can readily be achieved for constant pressure conditions ($p = p_c$) because under this constraint $a/a_c = [(a p / r_b) / (a p / r_b)_c] [r_b / (r_b)_{a=0}] / [(r_b)_c / (r_b)_{a=0}]$. The burning rate ratio at critical conditions is determined from the general results (refer to Figure 25).

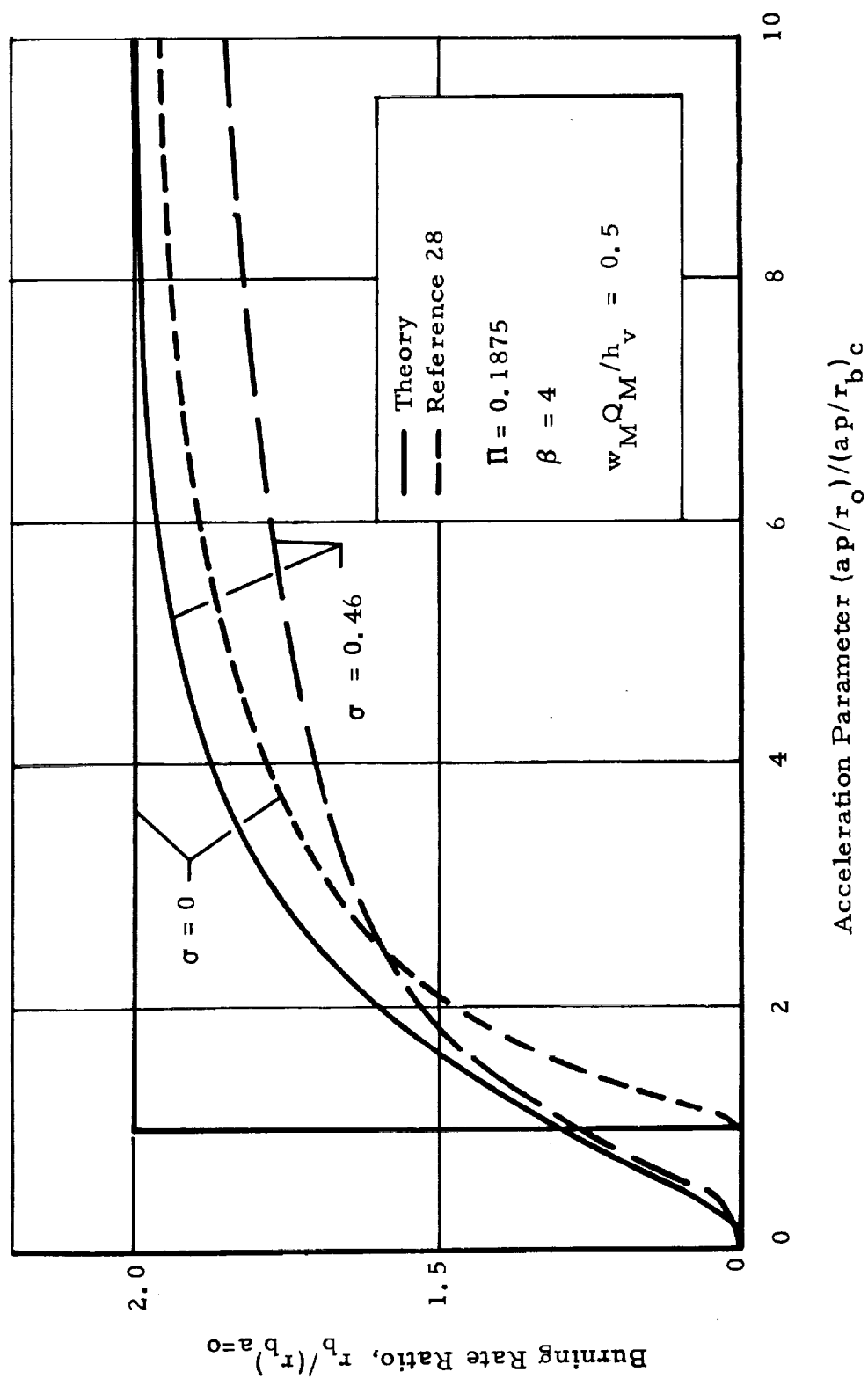


Figure 25. Theoretical Results.

Figure 26 illustrates the effect of the parameters Π and β on the burning rate ratio at constant pressure conditions. The figure shows that the general trends in the variation of burning rate ratio with acceleration ratio are unchanged and that both parameters affect the maximum value of the burning rate ratio. It is also seen that for equivalent asymptotic burning rate ratios (equivalent $\Pi\beta$ products) the characteristics depend upon the values of the individual parameters and that the magnitude of the characteristics change depends upon the magnitude of the $\Pi\beta$ product. When the $\Pi\beta$ product is small, the characteristics are not strongly dependent upon the individual (Π or β) values.

The theoretical results also show that the burning rate ratio is pressure dependent. The pressure dependence is conventionally expressed in the form

$$r_b = C_0 (p/p_c)^{C_1} \quad (146)$$

The effect of acceleration on the constants C_0 and C_1 will now be determined when $p = p_c$. The theory shows that burning rate can be written as

$$\left[(r_b)_{a=0} = \alpha_t (p/p_c)^n \right],$$

$$r_b = \alpha_t (p/p_c)^n f \left[(ap/r_b)/(ap/r_b)_c \right] \quad (147)$$

where the function f is illustrated graphically by Figure 25. Comparison of Eqs. (146) and (147) shows that the burning rate coefficient is $C_0 = \alpha_t f$. The burning rate exponent C_1 may be determined by differentiating Eqs. (146) and (147) with respect to p , equating the resulting expressions for $r_b^{-1} \partial r_b / \partial p$, and assuming that C_0 is not strongly dependent on pressure. This yields

$$C_1 = \frac{n + f' \left[(ap/r_b)/(ap/r_b)_c \right] / f}{1 + f' \left[(ap/r_b)/(ap/r_b)_c \right] / f} \quad (148)$$

where the prime denotes differentiation with respect to the argument of the function. Equation (148) shows that the burning rate coefficient has the same characteristics as the burning rate ratio. However, since f , f' , and $(ap/r_b)/(ap/r_b)_c$ are all greater than or equal to zero and $f'(0) = f'(\infty) = 0$, the C_1 variation will first increase from n and then decrease to n as the acceleration increases.

Figure 27 shows the theoretical variation of C_0 and C_1 with acceleration when $p = p_c$. Comparison of these results with the experimental results of Northam⁽³¹⁾ (refer to Figure 15) shows that the theory predicts the general trends shown by the experimental data. An exact comparison cannot be made between the figures because

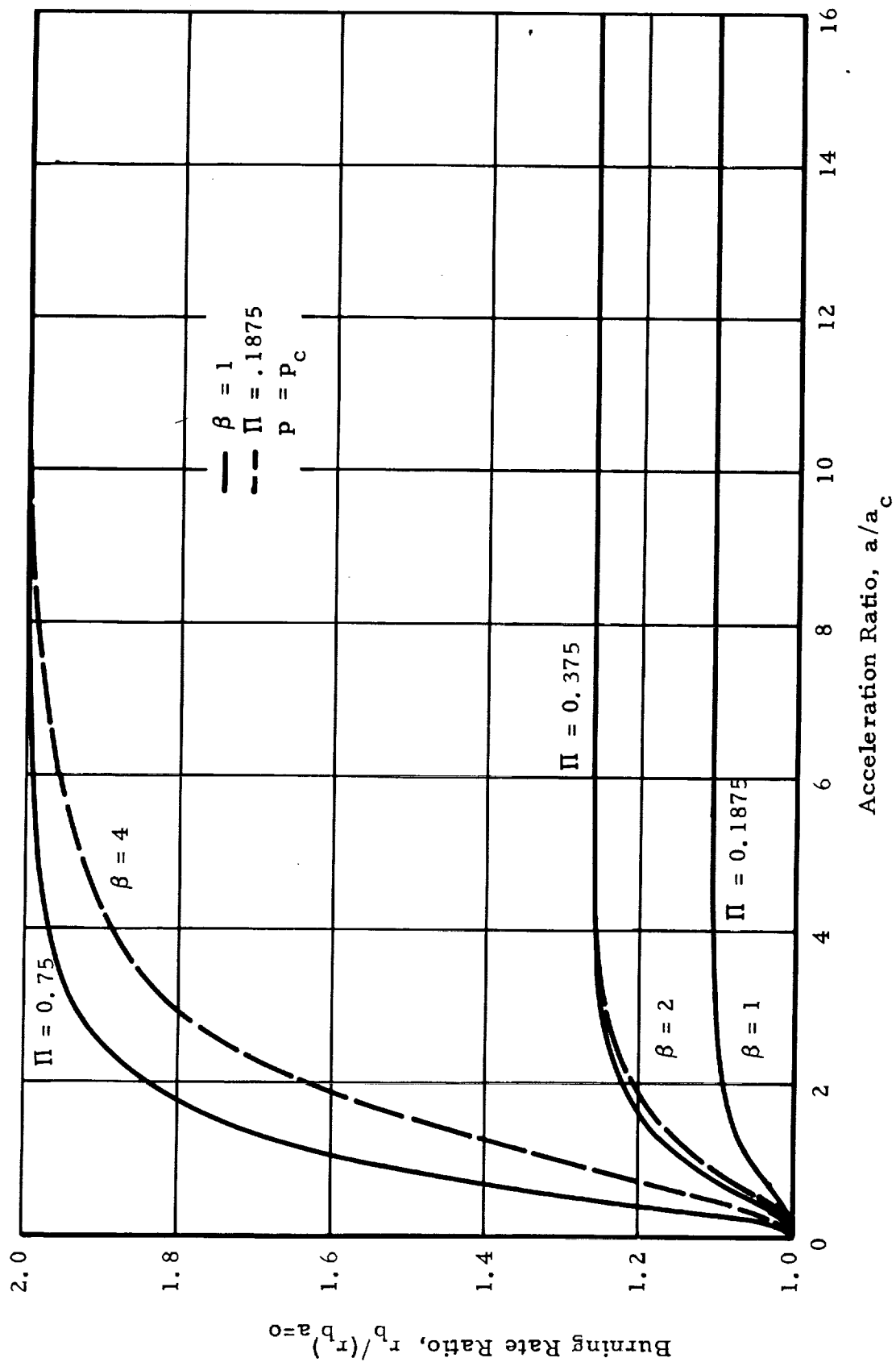


Figure 26. Effect of β and Π on the Theoretical Results.

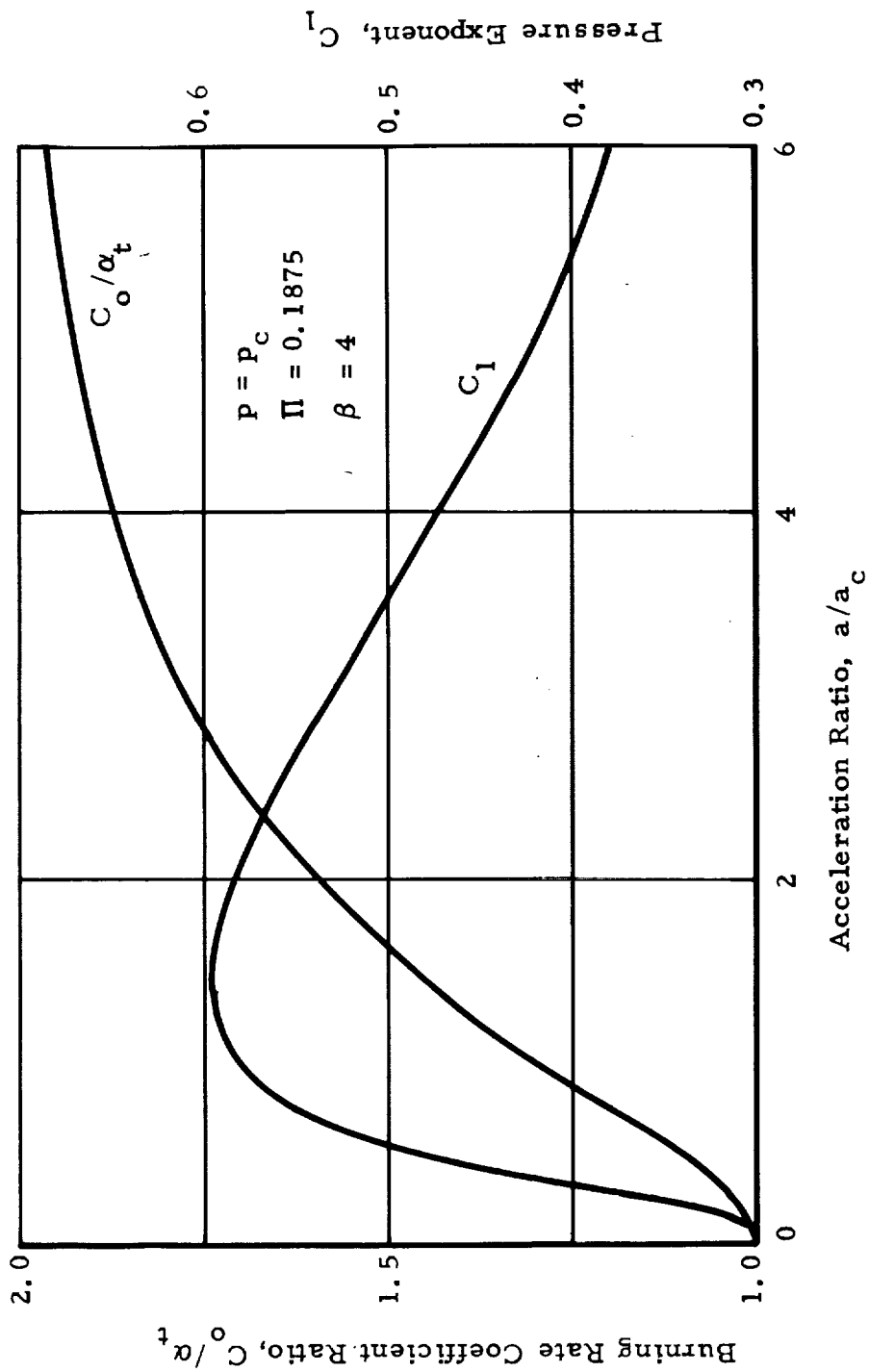


Figure 27. Effect of Acceleration on the Burning Rate Coefficient and the Pressure Exponent.

Northam's data also show that the parameter β is dependent upon the acceleration (refer to Figure 16); the theoretical results shown assume that $\beta = \text{constant}$. Further investigation of the theory when $\beta \neq \text{constant}$ is required before a quantitative comparison can be made. It should also be noted that the data of Reference 37 show that the pressure exponent depends upon both acceleration and binder composition. The variation observed with polyurethane binder agrees qualitatively with the theory; no significant variation was observed with PBAN binder. Further work is required to investigate the dependency of the pressure exponent with binder composition. It should also be noted that the theoretical variation of the burning rate coefficient C_0 is in qualitative agreement with the data of References 28, 31, and 37.

The general theory also shows that the burning rate varies with the direction of the acceleration force relative to the burning surface. This variation was investigated for conditions where the acceleration was sufficiently large for the burning rate ratio to be independent of the acceleration (saturated conditions). Figure 28 shows the variation of the burning rate ratio with angle for cases where $[r_b/(r_b)_{a=0}]_{\text{max}}$ are 1.5 and 2. The figure shows that the burning rate ratio decreases smoothly to unity as Φ increases. A simple cosine variation is included for comparison purposes. The figure shows that the theoretical change is more rapid than that predicted by the cosine function. The figure also shows that there is a critical angle beyond which, theoretically, the burning rate is independent of acceleration. Figure 29 illustrates the variation of the critical angle with the maximum value of the burning rate ratio. The figure shows that acceleration effects will not exist for $\Phi > 55^\circ$. The data of Northam⁽³¹⁾ at 100 g show that when $\Phi = 30^\circ$, $r_b/(r_b)_{a=0} = 1$. Examination of Northam's data shows that at 100 g the burning rate ratio is approximately 1.13. The theoretical value of Φ_c for this burning rate ratio is approximately 26° (refer to Figure 29). Therefore, the experimental and theoretical results again exhibit qualitative agreement.

Nonmetallized Propellants

The extension of the granular diffusion flame model presented in the ANALYSIS has shown that pressure differences and mean flows induced by accelerations are, at most, second order effects and that major effects must originate from the heterogeneous nature of the gas phase reaction zone. Moreover, the analytical formulation of the granular diffusion flame model has been extended and an equation relating the ratio of the burning rate in an acceleration field to the static burning rate to the drag coefficient of a pocket of fuel vapor, the direction of the acceleration force vector relative to the burning surface, and suitable Grashof, Reynolds, and Sherwood numbers has been derived. Because the first results are not amenable to comparison with experimental results, they will not be discussed further and the discussion will center on the analytical relationships that have been derived. In the first part of the discussion, the implications that arise as a consequence of these equations will be presented. In the second part of the discussion, the trends shown by the experimental data will be compared with the trends predicted by the analytical results.

Equations (134) and (143) have many similar characteristics. Therefore, these similar characteristics will be discussed first.

The fact that the Grashof number appears in the numerator of both equations implies that the burning rate ratio can increase without bound as the acceleration level increases. However, the experimental data of Anderson⁽³⁷⁾ (Figures 21 through 23)

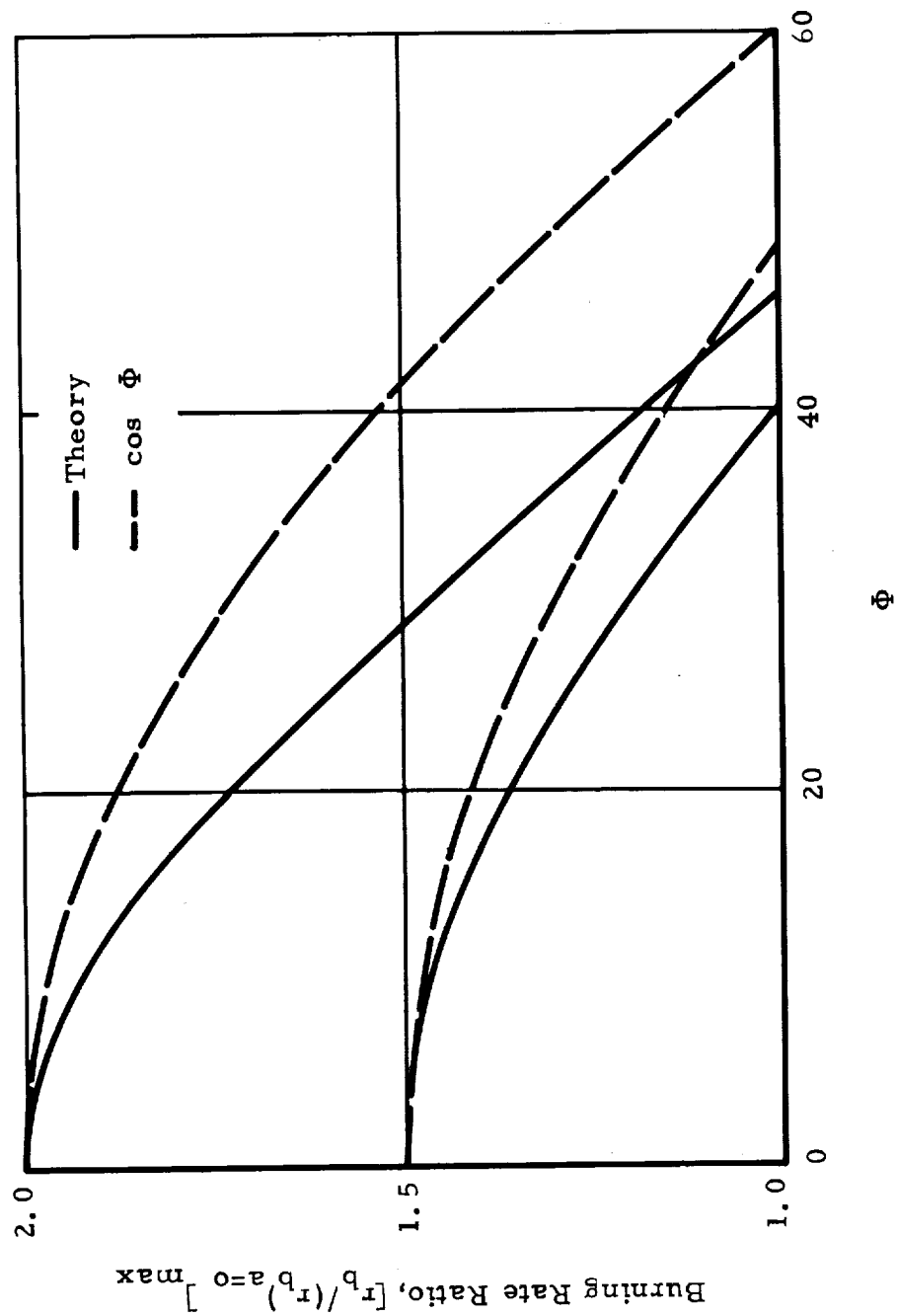


Figure 28. Effect of the Direction of Acceleration Force on the Maximum Burning Rate Ratio.

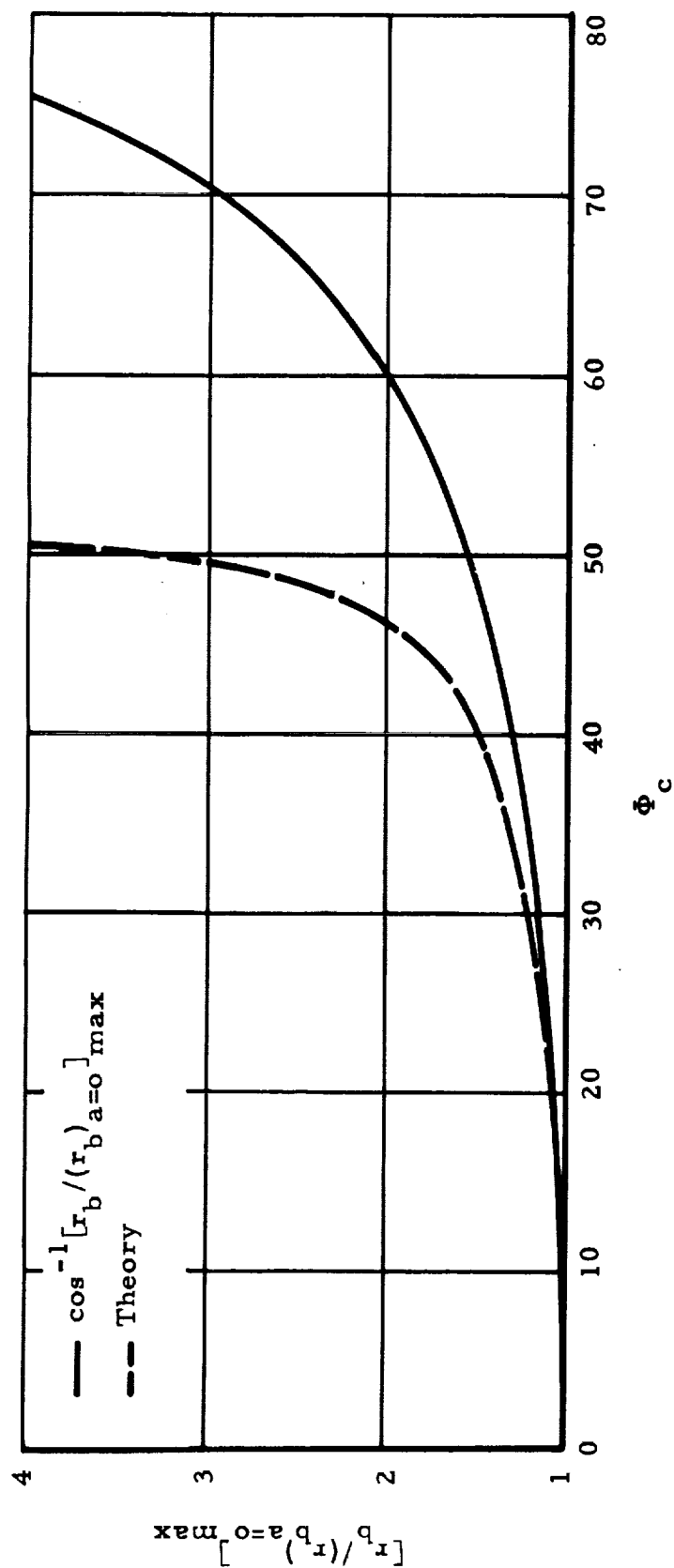


Figure 29. Variation of Critical Angle with Maximum Burning Rate Ratio.

and simple logic indicate that when $\Phi = 0$, the burning rate ratio approaches an upper bound as the acceleration level increases. When the acceleration is normal to and into the burning surface ($\Phi = 0$), the acceleration causes the velocity of the fuel vapor pocket to lag the velocity of the oxidizer vapors ($v_{fv} < v_g$). Therefore, when the acceleration is sufficiently large, the lag will have increased to the point where fuel vapor cannot escape from the burning surface in an unreacted state. Wherefore, the gas phase reaction zone should take on a stratified character. In this event, it would be expected that further increases in the acceleration level would have little effect on the burning rate.

The discussion above shows that the granular diffusion flame model must fail at high acceleration levels because the gas phase reaction zone loses its granular characteristics. The parameter that should govern the "granularity" of the gas phase reaction zone is the ratio of the thickness of the gas phase reaction zone to the characteristic dimension of the fuel vapor pocket. Therefore, when this parameter is large, the individual pockets will be identifiable and the model should apply. However, when this parameter is small, the model will not apply.

The fact that the Grashof number appears in the numerator also indicates that reducing the characteristic dimension of the fuel vapor pockets will reduce the effect of acceleration on burning rate. The characteristic dimension of the fuel vapor pocket has been assumed by Summerfield to be related to the mean diameter of the oxidizer particles.⁽³²⁾ Therefore, reducing the mean diameter of the oxidizer particles should reduce spin effects.

The fact that the static Reynolds number appears in the denominator shows that anything that increases the static burning rate will generally reduce the severity of acceleration effects. Therefore, the addition of burning rate catalysts as well as an increase in the initial temperature of the solid propellant should reduce acceleration effects. Moreover, since the static burning rate is related to the mean diameter of the oxidizer particles in such a manner that decreasing the mean diameter increases the static burning rate, it is seen that reducing the mean diameter of the oxidizer particles should be an effective way to reduce acceleration effects.

It should also be noted that the equations predict different burning rates for $\Phi = 0$, 90° , and 180° . Moreover, the burning rate for $\Phi = 0$ will be the greatest followed by that at $\Phi = 90^\circ$. The physical reasons for this have been discussed previously in the ANALYSIS.

It is interesting to note that the burning rate at $\Phi = 90^\circ$ is not dependent upon Re_0 and therefore, $(r_b)_{a=0}$.

The effect of acceleration on the pressure exponent will be examined next. However, the dependency of the Grashof and Reynolds numbers on pressure must be determined first.¹ The mass of a fuel vapor pocket is given by Eq. (87). Therefore, the Grashof and Reynolds numbers can be rewritten as

$$Gr_d \propto \frac{a \Delta \rho m}{\mu_g^2} \quad (149)$$

1. The Schmidt number Sc_g is not dependent upon pressure.

and

$$\text{Re}_o \propto \frac{(r_b)_{a=0} \rho_p^{m^{1/3}}}{u_g \rho_g^{1/3}} \quad (150)$$

Now both $\Delta\rho$ and ρ_g are directly proportional to pressure and the static burning rate at high pressure is proportional to $p^{1/3}$. However, the mass of the fuel vapor pocket, the acceleration, the dynamic viscosity, and the propellant density are independent of pressure. Therefore, the Grashof number Gr_d is proportional to pressure, but the static Reynolds number is independent of pressure. Thus, Eq. (143) becomes

$$\frac{r_b}{(r_b)_{a=0}} = C_6 p \cos \Phi + [(C_6 p \cos \Phi)^2 + C_7 p^{1/2} + 1]^{1/2} \quad (151)$$

Since the static burning rate is proportional to $p^{1/3}$, it is seen that the pressure exponent predicted by Eq. (151) is greater than unity ($n \sim 4/3$). The exception occurs when $\Phi = 90^\circ$ ($n \sim 7/12$).

This result implies that nonmetallized composite propellant could not be fired in a spinning rocket motor. Since the latter has occurred numerous times, a basic flaw must exist in Eq. (143). Examination of Eq. (134) shows that pressure dependency is largely controlled by the ratio Gr_d/C_d . Thus, the flaw could occur in connection with the relation assumed between C_d and Re_{rel} . Re-examination of the data of Redfield and Houghton shows that for $\text{Re}_{\text{rel}} > 10$, the drag coefficient becomes a function of the physical properties of the fluids as well as the size of the bubble. Moreover, in the analysis no specific account was made of the hot, reacted gases that must enclose the pocket of fuel vapor. Since the hot, reacted gases will flow counter to the direction of motion of the fuel vapor pocket relative to the oxidizer vapors, the relative velocity between the pocket and its immediate surroundings will be greater than the velocity of the pocket relative to the oxidizer vapors. This would increase the effective Re_{rel} . Furthermore, the system at hand is a gas-gas drop system while the empirical data being employed apply to liquid-liquid drop and liquid-gas drop systems. The lack of the stabilizing effect of surface tension combined with the small viscosities that exist in a gas system could greatly alter the drag characteristics as well as the mass transfer characteristics. Therefore, it appears plausible that the fault noted is connected with these factors.

The trends predicted by the theoretical results can be summarized as follows:

1. Burning rate in an acceleration field depends upon the orientation of the acceleration vector relative to the burning surface. The greatest change occurs when $\Phi = 0^\circ$. When $\Phi = 90^\circ$ or 180° , changes in burning rate should be small compared with the change when $\Phi = 0^\circ$.

2. The effect of acceleration on the burning rate ratio can be reduced when $\Phi \neq 90^\circ$ by the following: decreasing the particle size of the oxidizer, adding burning rate catalysts, and increasing the initial temperature of the propellant.
3. When the acceleration force is parallel to the burning surface ($\Phi = 90^\circ$), the burning rate ratio is not dependent upon either the catalyst content or the initial temperature of the propellant.

In addition to the above trends which were derived from Eqs. (134) and (143), a logical extension of the basic model to a situation where the acceleration vector is normal to and into the burning surface ($\Phi = 0$) and large shows that the flame loses its granular character and that there is an upper bound to acceleration induced changes in burning rate.

The trends shown by the experimental data have been summarized previously in the REVIEW OF THE LITERATURE. Comparison of the theoretical and experimental trends shows that the theory predicts the correct trend for the variation of burning rate with respect to the direction of the acceleration vector relative to the burning surface. In addition, the basic model predicts the observed upper bound in burning rate when the acceleration vector is normal to and into the burning surface. These results tend to confirm the analytical model.

The discussion above pertains to the general character of the analytical results and their agreement with the general trends shown by the available experimental results. However, Reference 37 has employed the theory to correlate acceleration-burning rate data under constant pressure conditions. Figure 30 presents the results of the comparison. The figure shows that the general trend of the data is well represented with the following important exception: (1) the theory predicts an immediate appreciable increase in burning rate while the data show that no increase in burning rate occurs until $a > 100 \text{ g}$, and (2) a negative $\Delta\rho$ is required to fit the data. Reference 37 has suggested that the first defect could be overcome by employing the concept of a critical acceleration. That is, for accelerations below the critical value $r_b/(r_b)_{a=0} = 1$ and for accelerations above the critical the theory is employed. The second consequence implies the largest acceleration effect will occur with this propellant when the acceleration force is away from the burning surface. Experiments with metallized composite propellants have shown that no appreciable change in burning rate occurs when the acceleration force vector is away from the surface⁽³¹⁾. Since particle burning effects cannot occur when the acceleration force is away from the surface, these results suggest that the corresponding effect on a nonmetallized propellant would also be negligible. Therefore, the negative $\Delta\rho$ required by the correlation is probably not in agreement with experiment. However, additional data are required for positive confirmation.

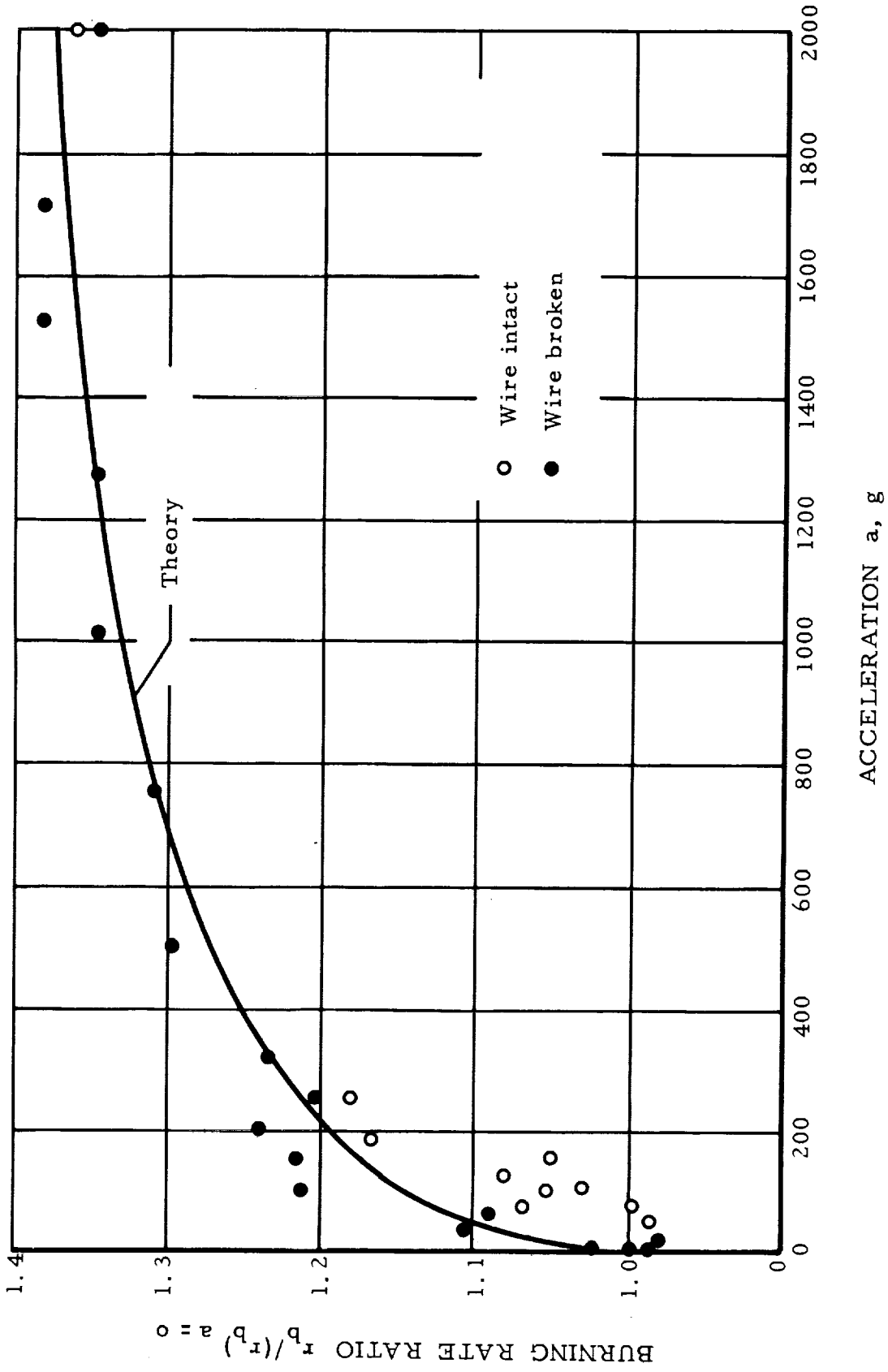


Figure 30. Comparison of Theory and Experiment for Nonmetallized Composite Propellant
(Reference 37)

CONCLUSIONS

The following conclusions may be drawn from the results of the present investigation.

PHASE I - INTERNAL GAS DYNAMICS

1. The major internal ballistics effects in single nozzle motors with CP grains possessing inhibited ends that are due to spin are connected with acceleration induced changes in burning rate and swirl effects in the nozzle.

PHASE II - EFFECT OF ACCELERATION ON BURNING RATE

Metallized Propellant

1. Acceleration induced burning rate changes can occur even though the metal additive is non-reactive.
2. Acceleration affects both the burning rate coefficient and the pressure exponent.
3. Acceleration effects can be reduced by reducing the particle size of the metal additive, the oxidizer particle size, and the metal content.
4. The effect of acceleration on burning rate is given by the equation

$$\frac{r_b}{(r_b)_{a=0}} = \left[\frac{1 - \Pi (G - 1)}{1 - \Pi [1 + (\beta_{\Phi=0} \cos \Phi - 1) G]} \right]^{1/2} \cos \Phi$$

where G is a function of the variables σ and $(a p / r_b) / (a p / r_b)_c$.

5. The theoretical model is in qualitative agreement with experiment with regards to the effect of acceleration on the pressure exponent and the burning rate coefficient and the effect of non-normal acceleration forces on burning rate.

Nonmetallized Propellants

1. The pressure exponent is not strongly dependent upon acceleration.
2. There is an upper bound on acceleration induced changes in burning rate.

3. Burning rate is insensitive to accelerations under 100 g.
4. The granular diffusion flame model predicts the following:
 - a. An upper bound on burning rate.
 - b. The burning rate ratio is independent of initial temperature and catalyst content when the acceleration force is parallel to the burning surface.
 - c. Acceleration effects can be reduced by adding burning rate catalysts, reducing the mean size of the oxidizer particles, and increasing the initial temperature of the propellant.
 - d. The burning rate ratio is given by the equation

$$\frac{r_b}{(r_b)_{a=0}} = C_1 \frac{Gr_d^{1/2} \cos \Phi}{C_d^{1/2} Re_o} + \left[C_1^2 \frac{Gr_d \cos^2 \Phi}{C_d Re_o^2} + \frac{Sh}{Sh_o} \right]^{1/2}$$

5. The effects of acceleration induced pressure differences across and mean flows in the gas phase reaction zone are negligible at accelerations under 1000 g.
6. The major effect of acceleration is derived from the effect of acceleration on the heterogeneous structure of the gas phase reaction zone.
7. The theory correlates the experimental data of Reference 37 for accelerations above 200 g.

RECOMMENDATIONS

The following recommendations are made.

1. Internal gas dynamics studies of motors with slotted tube grains (circumferential slots) and CP grains with uninhibited ends should be made because large swirl velocities can be achieved from radius changes; these swirl velocities can affect burning rate (erosive burning) and metal/metal oxide retention.
2. A theory for particle burning based solely on heat transfer (no metal combustion) should be developed.
3. The theory for metallized propellants developed herein should be examined to determine the effects of acceleration induced β changes.
4. A more general combustion model for the heterogeneous gas phase reaction zone should be formulated.
5. Experimental data for the thrust and discharge characteristics of nozzles with swirling flows should be obtained.
6. The effects of non-uniform burning rates on pressure and thrust-time histories should be determined.
7. Additional data concerning the effects of acceleration on the burning rate of both metallized and nonmetallized composite propellants should be obtained.

LIST OF REFERENCES

1. Lucy, M. H., Northam, G. B., and Swain, R. L., "Rocket Motor Spin Data Summary," NOTS TP 3770, U. S. Naval Ordnance Test Station, June 1965 (Confidential).
2. Dillinger, R. B., "Spin Effects - The Internal Ballistics of End-Burning Solid Propellant Rocket Motors," NOTS TP 3770, U. S. Naval Ordnance Test Station, June 1965 (Confidential).
3. Abernathy, C. W., "Fluorocarbon Propellant Performance in an Acceleration Field," NOTS TP 3770, U. S. Naval Ordnance Test Station, June 1965 (Confidential).
4. Barnard, C., "Spin Effects on Modified 4.5-Inch Army Barrage Rocket," NOTS TP 3770, U. S. Naval Ordnance Test Station, June 1965 (Confidential).
5. Barnard, R. and Karneskey, A. L., "Spin Effects on Rocket Motor Performance," NOTS TP 3770, U. S. Naval Ordnance Test Station, June 1965 (Confidential).
6. Harnett, S. J., "Effects of Spin on End-Burning Double-Base Propellant Grains," NOTS TP 3770, U. S. Naval Ordnance Test Station, June 1965 (Confidential).
7. Harnett, Stephen and Olstein, Myron, "The Effect of Spin on the Internal Ballistics of End Burning Rocket Propellants," Technical Memorandum Report No. 1555, Picatinny Arsenal, October 1964 (Confidential).
8. Lucy, M. H., Swain, R. L., and Foss, P. H., "Rocket Motor Spin-Test Apparatus," NASA-Langley Research Center, October 1964.
9. Lucy, M. H., Swain, R. L., and Hudson, J. L., Sr., "Variable Dynamic Force Vector Rocket Test Apparatus," NASA-Langley Research Center, October 1964.
10. Folsom, L. E., "Dynamic Spin Firing the BE-3-A4 ATHENA Motor," Bulletin 2nd Meeting Solid Propellant Rocket Static Test Working Group, October 1964, p. 201-212.
11. Torres, E. R., "Spinning Thrust Stand for a Five-Inch Rocket Engine," Bulletin 2nd Meeting Solid Propellant Rocket Static Test Working Group, October 1964, p. 27-42.
12. "Fourth-Stage Scout Rocket Motor Program Test Evaluation Report Component Development Static Firing Spin Test," UTC 2100-TER 1, Contract No. AF 04(695)-588, United Technology Center, August 1964.
13. "Fourth-Stage Scout Rocket Motor Program Test Evaluation Report Component Development Static Firing Spin Tests Fourth Test, Single-Segment TM-3A Motor," UTC 2100-TER 1 Supplement 1, Contract No. AF 04(695)-588, United Technology Center, November 1964.

14. Nelius, M. A. and White, D. W., "Results of Testing the HPC-ABL X-258 B-1 (S/N RH-47) Solid Propellant Rocket Motor Under the Combined Effects of Simulated Altitude and Rotational Spin," AEDC-TDR-64-41, Arnold Engineering Development Center, March 1964.
15. White, D. W. and Nelius, M. A., "Results of Testing Two HPC-ABL X-258 (S/N's RH-56 and RH-58) Solid-Propellant Rocket Motors Under the Combined Effects of Simulated Altitude and Rotational Spin," AEDC-TDR-64-97, Arnold Engineering Development Center, May 1964.
16. Allan, D. S., Bastress, E. K. and Kanption, D. A., "Interior Ballistics of Spinning Solid Propellant Rockets," Report C64868, A. D. Little.
17. Vecchio, R. and Harnett, S., "Static Spin Testing of Solid Propellants," Bulletin of the 1st Meeting, Working Group on Static Testing, October 1963.
18. Porter, M. G., et. al., "Fabrication and Testing of Javelin-Journeyman," ABL/QPR-18, Allegany Ballistics Laboratory, February 1960.
19. Goldshine, G. D., Goldstein, R. E., and Wenzel, R. F., Development of the Solid Propellant Gas Generator for the Tartar/Terrier Missile Auxiliary Power System," Bulletin of the Fifteenth Meeting of the JANAF Solid Propellant Group, June 1959.
20. Moody, G. H., Porter, M. G., and Helbert, W. B., Jr., "Jato X-248 Performance Data," ABL Dev. 1244, Allegany Ballistics Laboratory, 1959.
21. Butts, P. G. and Barr, C. J., "Developments in the Application of Rubber-Base Ammonium Nitrate Propellants to Solid Propellant Gas Generation," Bulletin of the Fifteenth Meeting of the JANAF Solid Propellant Group, June 1955 (Confidential).
22. Ordahl, P. D., "Some Problems Inherent in the Design and Development of Small Solid Propellant Auxiliary Power Units," Eleventh JANAF Solid Propellant Meeting, May 1955, p. 841-848 (Confidential).
23. Steifel, L. and Perkins, W. E., "A Review of Solid Propellant Gas Generators and Their Applications," Bulletin of the Fifteenth Meeting of the JANAF Solid Propellant Group, June 1959, p. 156 (Confidential).
24. Murphy, J. M. and Wall, R. H., "Effects of Grain Configuration Upon the Burning Rate of a Spinning Rocket Motor," J. Spacecraft and Rockets, Vol. 3, No. 2, 1966, p. 263-264.
25. Wall, R. H., "Interior Ballistic and Grain Design Studies of a Spin-Stabilized Gun-Boosted Rocket Using a Polysulfide-Perchlorate Propellant," Eleventh JANAF Solid Propellant Meeting, May 1955, p. 675-692 (Confidential).
26. Mager, A., "Approximate Solution of Isentropic Swirling Flow Through a Nozzle," ARS J., 31, 1961, 0. 1140-1148.

27. Rott, N. and Lewellen, W. S., General Research-Boundary Layers in Rotating Flows, Aerospace Corporation, Report No. ATN-64 (9227)-6 September 1964.
28. Crowe, C. T., et. al., "Investigation of Particle Growth and Ballistics Effects on Solid Propellant Rockets," UTC 2128-FR, United Technology Center, June 1966.
29. Shapino, A. H., The Dynamics and Thermodynamics of Compressible Fluid Flow, (Ronald Press Co., New York, New York, 1954) Vol. I.
30. Burington, R. S., Handbook of Mathematical Tables and Formulas, (Handbook Publishers, Inc., Sandusky, Ohio, 1956), p. 18.
31. Northam, G. B., "An Experimental Investigation of the Effects of Acceleration on the Combustion Characteristics of an Aluminized Composite Solid Propellant," MS Thesis, Virginia Polytechnic Institute, June 1965.
32. Summerfield, M., et. al., "Burning Mechanism of Ammonium Perchlorate Propellants," Progress in Astronautics and Rocketry, (Academic Press, Inc., New York, New York, 1960), Vol. I, p. 141-182.
33. Eckert, E. R. G. and Drake, R. M., Heat and Mass Transfer, McGraw-Hill Book Co., Inc., New York, New York, 1959.
34. Redfield, J. A. and Houghton, G., "Mass Transfer and Drag Coefficients for Single Bubbles at Reynolds Numbers of 0.02 - 5000," Chemical Engineering Science, Vol. 20, 1965, p. 131-139.
35. Horton, J. G., "Experimental Evaluation of Solid Propellant Rocket Motors Under Acceleration Loads," J. Spacecraft and Rockets, Vol. 1, No. 6, 1964, p. 673-675.
36. Landau, Z. H. and Gegielski, J. M., "The Ballistic Behavior of Solid Propellant Rocket Motor Grains in a High Acceleration Environment," AIAA Preprint No. 64-228, June 1964.
37. Anderson, J. B., "An Investigation of the Effect of Acceleration on the Burning Rate of Composite Propellants," Ph.D. Thesis, U. S. Naval Postgraduate School, August 1966.
38. Iwanciw, B. L., Lawrence, W. J. and Martins, J., "The Effect of Acceleration on Solid Composite Propellant Combustion," AIAA Preprint No. 64-227, June 1964.
39. DeDapper, J. W. and Drobot, W., "The Effect of Acceleration on the Burning Rates of Selected Propellants," CPIA Publication 83 (Classified Papers of 6th AIAA Solid Rocket Conference), August 1965, p. 101-127 (Confidential).

40. "Evaluation of Solid Propellant Motor Ballistic Properties Under High 'g' Environment," Report No. E93-63, Vol. I, Thiokol Chemical Corporation, Elkton Division, June 1963 (Confidential).
41. "An Investigation to Characterize the Effects of Acceleration on the Burning of Gun-Boosted Rocket Propellants," Report VML-14, Redel, Inc., March 1964 (Confidential).
42. "An Investigation of the Effects of Acceleration on the Burning Characteristics of Solid Propellants," Report No. KPR-5, Redel, Inc., February 1961 (Confidential).
43. Zelerznik, F. J. and Gordon, S., "A General IBM 704 or 7090 Computer Program for Computation of Chemical Equilibrium Composition, Rocket Performance, and Chapman-Jouget Detonation," NASA TN D-1454.
44. Sabadell, A. J., Wenograd, J. and Summerfield, M., "Measurement of Temperature Profiles through Solid Propellant Flames Using Fine Thermocouples," AIAA J., Vol. 3, No. 2, 1965, p. 1580-1584.
45. Bartz, D. R., "A Simple Equation for the Rapid Estimation of Rocket Nozzle Convective Heat Transfer Coefficients," Jet Propulsion, January 1957, p. 49-51.

APPENDIX A

EXPRESSIONS FOR $d\psi/\psi$ AND $d\phi/\phi$

Consider the function

$$g = \int_{\eta_c}^1 \left(1 - \frac{\eta_c}{1 - \eta_c}\right)^{\frac{1 - \eta}{\eta}} d\eta \quad (A-1)$$

where α is a constant. It is readily recognized that the function g has the same form as ψ and ϕ depending on the value of α . Application of Liebnitz Rule yields

$$\frac{dg}{d\eta_c} = - \frac{\alpha}{(1 - \eta_c)^2} \int_{\eta_c}^1 \left(1 - \frac{\eta_c}{1 - \eta_c}\right)^{\alpha - 1} \frac{1 - \eta}{\eta} d\eta \quad (A-2)$$

Thus

$$\frac{d\psi}{\psi} = - \frac{\eta_c}{\psi (1 - \eta_c)^2} \frac{1}{\gamma - 1} \int_{\eta_c}^1 \left(1 - \frac{\eta_c}{1 - \eta_c}\right)^{\frac{2 - \gamma}{\gamma - 1}} \frac{1 - \eta}{\eta} d\eta \frac{d\eta_c}{\eta_c} \quad (A-3)$$

$$\frac{d\phi}{\phi} = - \frac{\eta_c}{\phi (1 - \eta_c)^2} \frac{\gamma}{\gamma - 1} \int_{\eta_c}^1 \left(1 - \frac{\eta_c}{1 - \eta_c}\right)^{\frac{1}{\gamma - 1}} \frac{1 - \eta}{\eta} d\eta \frac{d\eta_c}{\eta_c} \quad (A-4)$$

However, from the definitions of η_c and M_θ

$$\frac{\eta_c}{(1 - \eta_c)^2} = \frac{\gamma - 1}{2} M_\theta^2 \left(1 + \frac{\gamma - 1}{2} M_\theta^2\right) \quad (A-5)$$

and

$$\frac{d\eta_c}{\eta_c} = \frac{1}{1 + \frac{\gamma - 1}{2} M_\theta^2} \frac{dM_\theta^2}{M_\theta^2} \quad (A-6)$$

Whence

$$\frac{d\psi}{\psi} = g_{\psi} \frac{dM_{\theta}^2}{M_{\theta}^2} \quad (A-7)$$

$$\frac{d\varphi}{\varphi} = g_{\varphi} \frac{dM_{\theta}^2}{M_{\theta}^2} \quad (A-8)$$

Where

$$g_{\psi} = - \frac{M_{\theta}^2}{2\psi} \int_{\eta_c}^1 \left(1 - \frac{\eta_c}{1-\eta_c} \frac{1-\eta}{\eta} \right)^{\frac{2-\gamma}{\gamma-1}} \frac{1-\eta}{\eta} d\eta \quad (A-9)$$

$$g_{\varphi} = - \frac{\gamma M_{\theta}^2}{2\varphi} \int_{\eta_c}^1 \left(1 - \frac{\eta_c}{1-\eta_c} \frac{1-\eta}{\eta} \right)^{\frac{1}{\gamma-1}} \frac{1-\eta}{\eta} d\eta \quad (A-10)$$

APPENDIX B

FLOW IN A CONICAL PIT

The steady, axisymmetric, and inviscid flow of an incompressible fluid in a conical pit was studied. Figure B-1 is a schematic diagram that illustrates the cone, coordinate system, and nomenclature. In addition to the assumptions mentioned above, it was also assumed that the combustion gases leave the surface of the cone along a normal at the velocity

$$V_{\theta}(r, \theta_c) = -r_b \rho_p / \rho_g \quad (B-1)$$

and that the cone is of infinite extent.

The axisymmetric assumption is based on the symmetry of the problem and the compressible assumption is based on the fact that the Mach numbers will be small since the acoustic speed is large. The assumption concerning the boundary condition is based on photographs of the flow in cones around fibers. The inviscid and infinite extent assumptions are made to simplify the problem.

With the assumptions above, the governing equations are

$$\frac{\partial}{\partial r}(r^2 V_r) + \frac{r}{\sin \theta} \frac{\partial}{\partial \theta}(V_{\theta} \sin \theta) = 0 \quad (B-2)$$

$$V_r \frac{\partial V_r}{\partial r} + \frac{V_{\theta}}{r} \frac{\partial V_r}{\partial \theta} - \frac{V_{\theta}^2}{r} = -\frac{1}{\rho} \frac{\partial p}{\partial r} \quad (B-3)$$

$$V_r \frac{\partial V_{\theta}}{\partial r} + \frac{V_{\theta}}{r} \frac{\partial V_{\theta}}{\partial \theta} + \frac{V_r V_{\theta}}{r} = -\frac{1}{\rho r} \frac{\partial p}{\partial \theta} \quad (B-4)$$

and the boundary conditions are Eq. (B-1) and

$$V_{\theta}(r, 0) = V_r(r, \theta_c) = 0 \quad (B-5)$$

The pressure terms in Eqs. (B-3) and (B-4) were eliminated by cross differentiation and then summation. The resulting equation and Eq. (B-2) were reduced to ordinary differential equations by assuming that the dependent variables were functions of theta alone.

This yielded

$$V_r = f(\theta); V_{\theta} = g(\theta)$$

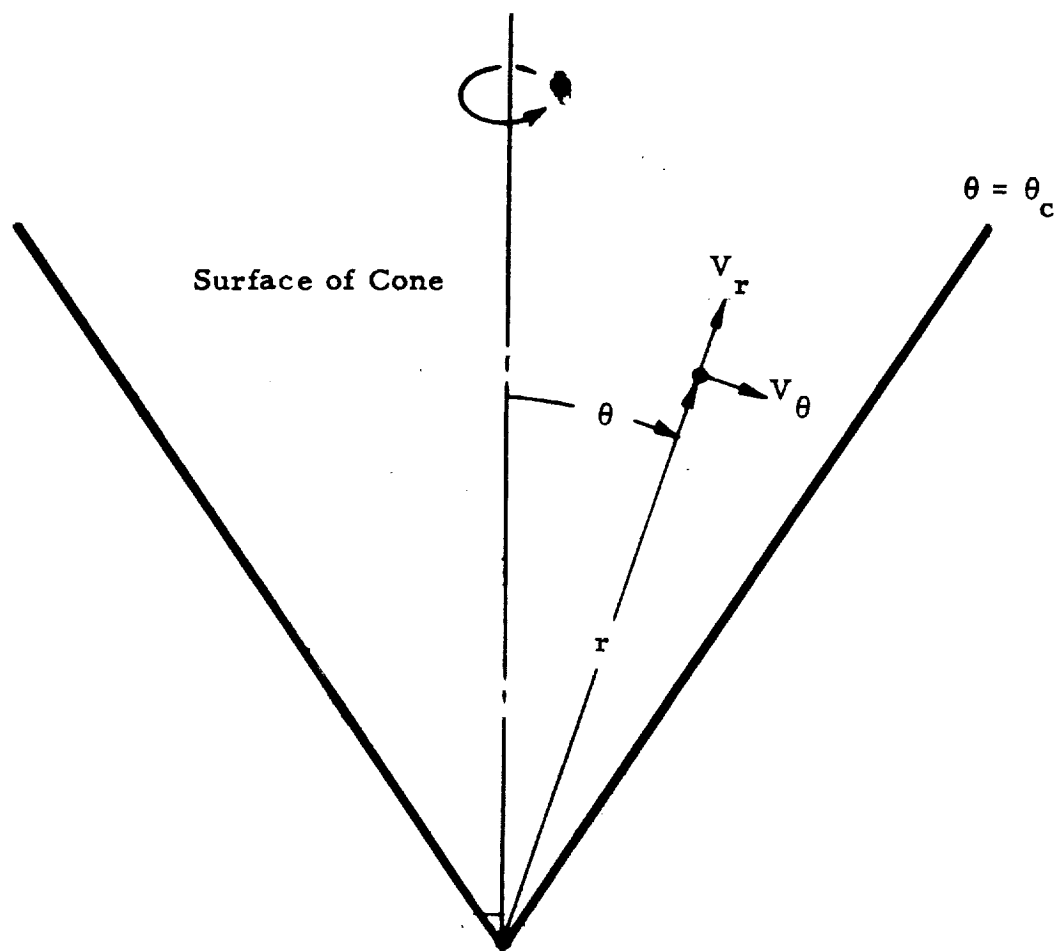


Figure B-1. Schematic Diagram Illustrating Cone and Coordinate System

$$2f + g' + g \cot \theta = 0 \quad (\text{B-6})$$

$$g f'' + f' g' = g g' = 0 \quad (\text{B-7})$$

The boundary conditions became

$$f(\theta_c) = g(0) = 0 \quad (\text{B-8})$$

$$g(\theta_c) = -r_b \rho_p / \rho_g \quad (\text{B-9})$$

A numerical technique employing the Runge-Kutta method to integrate from $\theta = \theta_c$ to $\theta = \Delta$ and a Taylor's series to extend the results to $\theta = 0$ was developed. The resulting computer program was partially debugged.

APPENDIX C

TYPICAL PROPERTIES OF NONMETALLIZED
COMPOSITE PROPELLANTS

An important portion of the analysis presented herein is concerned with the estimation of the order of magnitude of various effects. For these estimates, typical values for various thermo-physical properties are required. The objective of this appendix is to present typical values for the required properties.

Nonmetallized composite propellants essentially consist only of binder and oxidizer. The binder is usually based on a hydrocarbon material; the pertinent oxidizer here is ammonium perchlorate. The general characteristics of the propellant are selected in practice as a balance between energetic and physical property considerations. In most cases of interest, the weight fraction of binder ranges from 10 to 25 percent.

Figure C-1 presents the effect of the weight fraction of binder on the adiabatic flame temperature, molecular weight, and specific heat ratio of the products of combustion of the propellant at equilibrium at a pressure of 1000 psia. The results were calculated by the method of Reference 43 and employed JANAF thermophysical properties. The figures show that typical values for these variables are as follows: $T_f = 4500$ R, $\gamma = 1.22$, and $M = 22$.

Reference 44 has measured the surface temperature of nonmetallized composite propellants with ammonium perchlorate oxidizer and has found that the surface temperature ranges from 1500 to 1700 R. Thus, a typical value for the temperature of the burning surface is 1500 R.

The mean temperature of the gas in the gas phase reaction zone is the mean of the surface and flame temperatures. Therefore, a typical value for this temperature is 3000 R.

Figure C-2 presents the effect of temperature on the thermodynamic properties of the pyrolysis products of a typical binder at 1000 psia. The binder is the one employed in the previous calculations and the computational procedure employed is the same. The figure shows that typical values for the molecular weight and specific heat ratio at the mean temperature of the gas phase reaction zone are 19 and 1.12, respectively.

Figure C-3 presents the effect of temperature on the thermodynamic properties of the equilibrium decomposition products of ammonium perchlorate at 1000 psia. The computation procedure is the one employed previously. The figure shows that the molecular weight and specific heat ratio at the mean temperature of the gas phase reaction zone are 28 and 1.24, respectively.

It is important to note that the molecular weight and specific heat ratio of the fuel and oxidizer vapors are not widely different from those of the products of combustion. Therefore, these properties are relatively constant throughout the gas phase

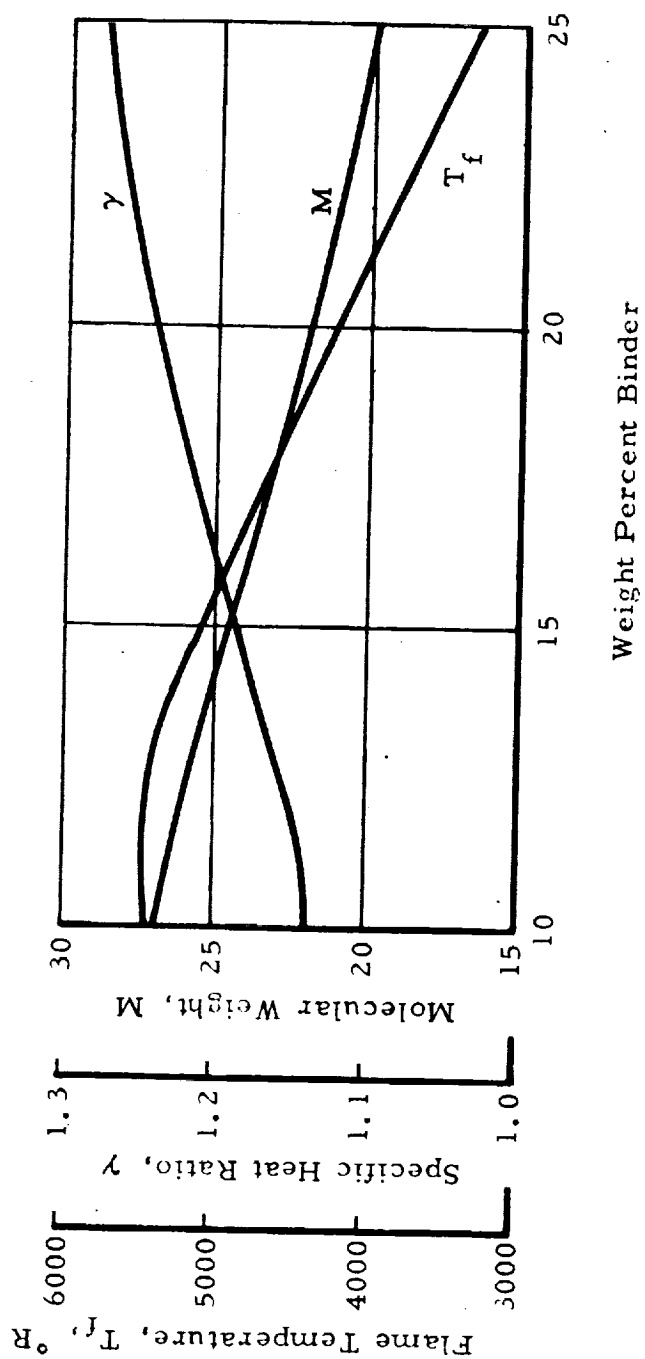


Figure C-1. Thermodynamic Properties of the Products of Combustion of a Typical Propellant at 1000 psia

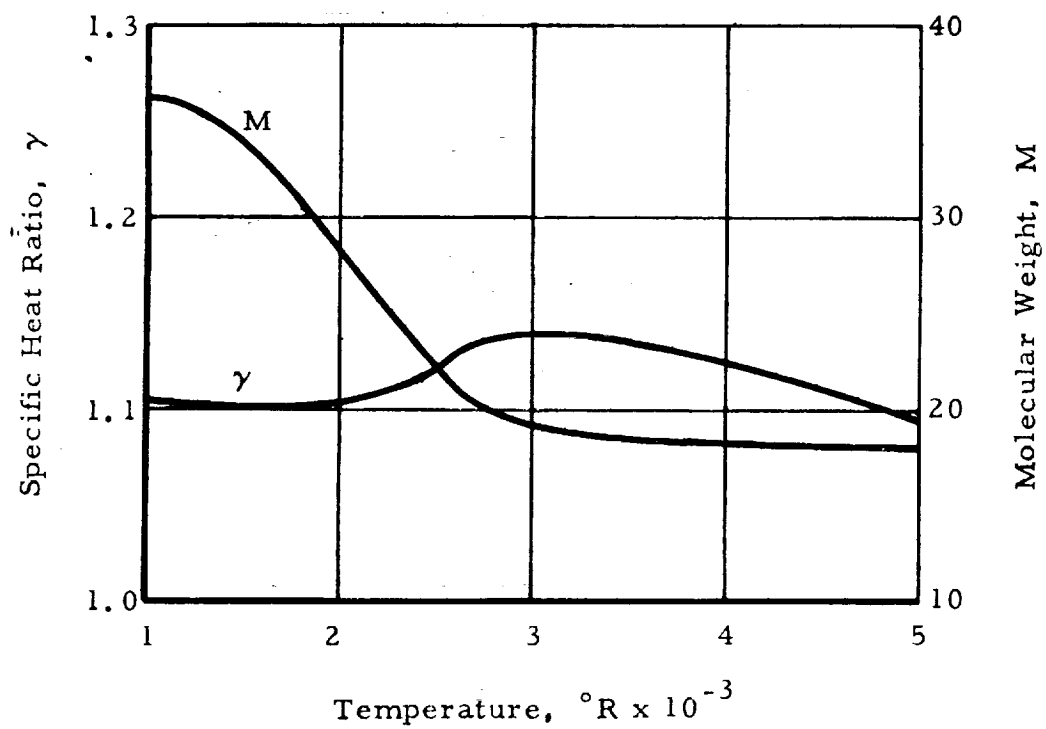


Figure C.-2. Thermodynamic Properties of Typical Fuel Vapors at 1000 psia

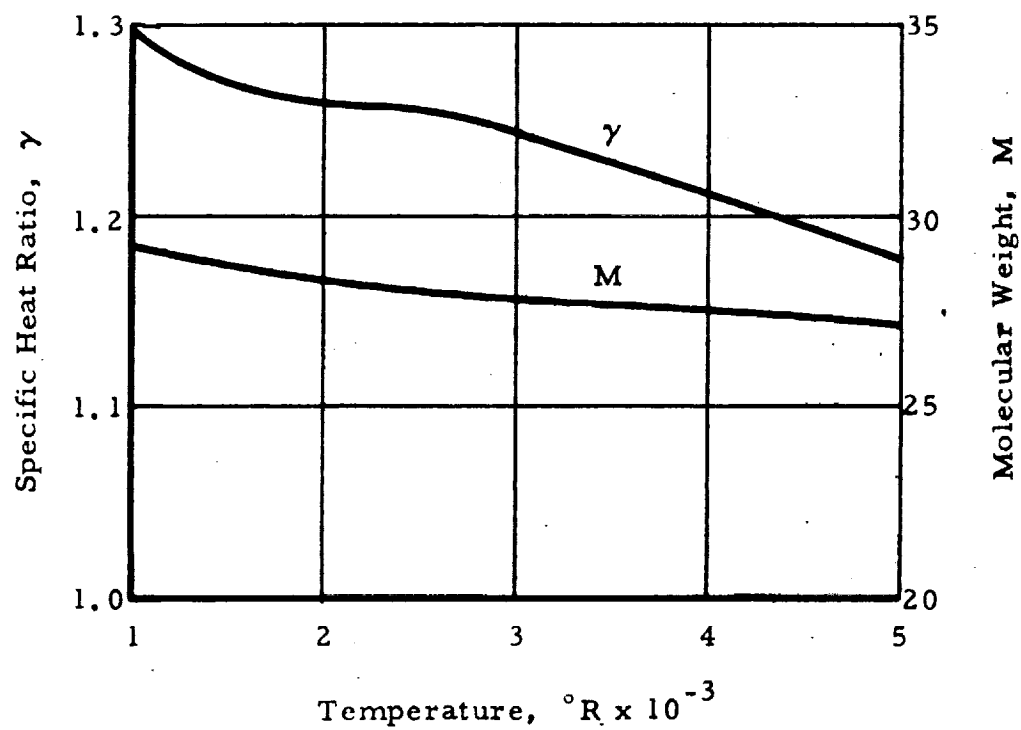


Figure C-3. Thermodynamic Properties of Oxidizer Vapors at 1000 psia

reaction zone. The values given previously for the products of combustion of the propellant will be employed as typical values.

Typical values for viscosity, Prandtl number, and thermal conductivity were computed from the previous typical values and the relationships presented by Bartz⁴⁵. Thus, $\mu_g = 1 \times 10^{-6}$ slug/ft-sec and $Pr_g = 0.82$.

The densities required were computed from the perfect gas law for the previous typical conditions ($p = 1000$ psia, $M = 22$, $T_f = 4500$ R, $t_s = 1500$ R, $t_g = 3000$ R). This yields $\rho_s = 0.042$ slug/cu. ft., $\rho_g = 0.021$ slug/cu. ft., and $\rho_f = 0.014$ slug/cu. ft.

The burning rate of nonmetallized composite propellants usually ranges from 0.2 to 2.0 in/sec. Therefore, a value of 1 in/sec was chosen as typical.

The density of nonaluminized composite propellants is around 0.060 lb_m/cu. in. This value will be employed herein.

The normal velocity of the gas at the burning surface can be computed from the continuity equation or

$$v_s = r_b \rho_p / \rho_s$$

Substitution of the pertinent typical values gives

$$v_s = 6.4 \text{ ft/sec}$$

Reference 32 has employed several different methods to measure the thickness of the gas phase reaction zone of a nonmetallized composite propellant with ammonium perchlorate oxidizer. All of these methods indicate that the zone is less than 100 microns thick at pressures above 200 psia. Therefore, it will be assumed that 100 microns is a typical value for the thickness of the gas phase reaction zone.

A typical value for the mean diameter of the oxidizer particles is 50 microns.

The typical values computed and assumed are presented in Table C -1.

TABLE C-I

TYPICAL VALUES FOR THERMOPHYSICAL PROPERTIES

p	$= 1000 \text{ psia}$	μ_g	$= 1 \times 10^{-6} \text{ slug/ft-sec}$
T_f	$= 4500 \text{ R}$	ρ_s	$= 4.2 \times 10^{-2} \text{ slug/ft}^3$
t_s	$= 1500 \text{ R}$	ρ_g	$= 2.1 \times 10^{-2} \text{ slug/ft}^3$
t_g	$= 3000 \text{ R}$	ρ_f	$= 1.4 \times 10^{-2} \text{ slug/ft}^3$
M	$= 22$	ρ_p	$= 3.2 \text{ slug/ft}^3$
γ	$= 1.22$	v_s	$= 6.4 \text{ ft/sec}$
Pr_g	$= 0.82$	v_f	$= 19.1 \text{ ft/sec}$
R	$= 2.27 \times 10^3 \text{ ft-lb}_f/\text{slug-R}$	r_b	$= 8.33 \times 10^{-2} \text{ ft/sec}$
d_{ox}	$= 1.64 \times 10^{-4} \text{ ft}$	δ_r	$= 3.28 \times 10^{-4} \text{ ft}$

DOCUMENT CONTROL DATA - R&D		
(Security classification of title, body of abstract and indexing annotation must be entered when the overall report is classified)		
1. ORIGINATING ACTIVITY (Corporate author) Huntsville Division Thiokol Chemical Corporation Huntsville, Alabama		2a. REPORT SECURITY CLASSIFICATION UNCLASSIFIED
		2b. GROUP
3. REPORT TITLE AN ANALYTICAL STUDY OF THE EFFECTS OF RADIAL ACCELERATION UPON THE COMBUSTION MECHANISM OF SOLID PROPELLANT		
4. DESCRIPTIVE NOTES (Type of report and inclusive dates) Final -- 19 August 1965 - 18 August 1966		
5. AUTHOR(S) (Last name, first name, initial) Glick, Robert L.		
6. REPORT DATE September 1966	7a. TOTAL NO. OF PAGES 102	7b. NO. OF REFS 45
8a. CONTRACT OR GRANT NO. NAS 7-406	9a. ORIGINATOR'S REPORT NUMBER(S) 42-66	
b. PROJECT NO.		
c.	9b. OTHER REPORT NO(S) (Any other numbers that may be assigned this report)	
d.	U-66-42A	
10. AVAILABILITY/LIMITATION NOTICES		
11. SUPPLEMENTARY NOTES	12. SPONSORING MILITARY ACTIVITY NASA Langley Research Center Hampton, Virginia	
13. ABSTRACT Analytical studies were made of the effects of spin on the internal ballistics at fixed time of rocket motors with axisymmetric grains and the effect of acceleration on the burning rate of metallized and nonmetallized composite propellants. In the internal ballistics studies influence coefficients were derived for one-dimensional vortex flow with mass addition and area change; an internal ballistics at fixed time computer program based on numerical integration of the influence coefficient equations was written. Limited numerical results suggest that motor spin effects result largely from nozzle effects and acceleration induced burning rate changes. In the burning rate studies a theoretical model based on particle burning was developed for metallized composite propellants; the granular diffusion flame model was extended to include acceleration effects for nonmetallized composite propellants. The unclassified data concerning the effect of acceleration on burning rate was reviewed and the theoretical results compared with the trends shown by the data. In general, the comparison validated the models. However, several important discrepancies were noted. Probable causes for these discrepancies are discussed.		

14	KEY WORDS	LINK A		LINK B		LINK C	
		ROLE	WT	ROLE	WT	ROLE	WT
Combustion Theory Solid Propellant Spin Effects Composite Propellants							

INSTRUCTIONS

1. **ORIGINATING ACTIVITY:** Enter the name and address of the contractor, subcontractor, grantee, Department of Defense activity or other organization (*corporate author*) issuing the report.

2a. **REPORT SECURITY CLASSIFICATION:** Enter the overall security classification of the report. Indicate whether "Restricted Data" is included. Marking is to be in accordance with appropriate security regulations.

2b. **GROUP:** Automatic downgrading is specified in DoD Directive 5200.10 and Armed Forces Industrial Manual. Enter the group number. Also, when applicable, show that optional markings have been used for Group 3 and Group 4 as authorized.

3. **REPORT TITLE:** Enter the complete report title in all capital letters. Titles in all cases should be unclassified. If a meaningful title cannot be selected without classification, show title classification in all capitals in parenthesis immediately following the title.

4. **DESCRIPTIVE NOTES:** If appropriate, enter the type of report, e.g., interim, progress, summary, annual, or final. Give the inclusive dates when a specific reporting period is covered.

5. **AUTHOR(S):** Enter the name(s) of author(s) as shown on or in the report. Enter last name, first name, middle initial. If military, show rank and branch of service. The name of the principal author is an absolute minimum requirement.

6. **REPORT DATE:** Enter the date of the report as day, month, year, or month, year. If more than one date appears on the report, use date of publication.

7a. **TOTAL NUMBER OF PAGES:** The total page count should follow normal pagination procedures, i.e., enter the number of pages containing information.

7b. **NUMBER OF REFERENCES:** Enter the total number of references cited in the report.

8a. **CONTRACT OR GRANT NUMBER:** If appropriate, enter the applicable number of the contract or grant under which the report was written.

8b, 8c, & 8d. **PROJECT NUMBER:** Enter the appropriate military department identification, such as project number, subproject number, system numbers, task number, etc.

9a. **ORIGINATOR'S REPORT NUMBER(S):** Enter the official report number by which the document will be identified and controlled by the originating activity. This number must be unique to this report.

9b. **OTHER REPORT NUMBER(S):** If the report has been assigned any other report numbers (*either by the originator or by the sponsor*), also enter this number(s).

10. **AVAILABILITY/LIMITATION NOTICES:** Enter any limitations on further dissemination of the report, other than those

imposed by security classification, using standard statements such as:

- (1) "Qualified requesters may obtain copies of this report from DDC."
- (2) "Foreign announcement and dissemination of this report by DDC is not authorized."
- (3) "U. S. Government agencies may obtain copies of this report directly from DDC. Other qualified DDC users shall request through _____."
- (4) "U. S. military agencies may obtain copies of this report directly from DDC. Other qualified users shall request through _____."
- (5) "All distribution of this report is controlled. Qualified DDC users shall request through _____."

• If the report has been furnished to the Office of Technical Services, Department of Commerce, for sale to the public, indicate this fact and enter the price, if known.

11. **SUPPLEMENTARY NOTES:** Use for additional explanatory notes.

12. **SPONSORING MILITARY ACTIVITY:** Enter the name of the departmental project office or laboratory sponsoring (paying for) the research and development. Include address.

13. **ABSTRACT:** Enter an abstract giving a brief and factual summary of the document indicative of the report, even though it may also appear elsewhere in the body of the technical report. If additional space is required, a continuation sheet shall be attached.

It is highly desirable that the abstract of classified reports be unclassified. Each paragraph of the abstract shall end with an indication of the military security classification of the information in the paragraph, represented as (TS), (S), (C), or (U).

There is no limitation on the length of the abstract. However, the suggested length is from 150 to 225 words.

14. **KEY WORDS:** Key words are technically meaningful terms or short phrases that characterize a report and may be used as index entries for cataloging the report. Key words must be selected so that no security classification is required. Identifiers, such as equipment model designation, trade name, military project code name, geographic location, may be used as key words but will be followed by an indication of technical context. The assignment of links, rules, and weights is optional.

INITIAL EXTERNAL DISTRIBUTION

(NASA CR-66218 Distribution List)

	<u>Copies</u>
NASA Langley Research Center	
Langley Station	
Hampton, Virginia 23365	
Attention: Dr. Andrew Saunders, Mail Stop 214	5
Mr. Robert L. Swain, Mail Stop 214	1
Chief, Propulsion Branch, Mail Stop 214	1
Library, Mail Stop 185	1
R. L. Zavasky, Mail Stop 117	1
 NASA Ames Research Center	
Moffett Field, California 94035	
Attention: Library	1
 NASA Flight Research Center	
P. O. Box 273	
Edwards, California 93523	
Attention: Library	1
 NASA Goddard Space Flight Center	
Greenbelt, Maryland 20771	
Attention: Library	1
 Jet Propulsion Laboratory	
4800 Oak Grove Drive	
Pasadena, California 91103	
Attention: Library	1
 NASA Manned Spacecraft Center	
Houston, Texas 77001	
Attention: Library	1
 NASA Marshall Space Flight Center	
Huntsville, Alabama 35812	
Attention: Library	1
Solid Propulsion Section, RP&VE-PPS	1
 NASA Western Operations	
150 Pico Boulevard	
Santa Monica, California 90406	
Attention: Library	1
 NASA Western Operations	
150 Pico Boulevard	
Santa Monica, California 90406	
Attention: Mr. J. S. Evans, Contracting Officer	10
Mr. Eugene F. Wyszpolsk	1

	<u>Copies</u>
NASA Wallops Station Wallops Island, Virginia 23337 Attention: Library	1
NASA Electronics Research Center 575 Technology Square Cambridge, Massachusetts 02139 Attention: Library	1
NASA Lewis Research Center 2100 Brookpark Road Cleveland, Ohio 44135 Attention: Mail Stop 3-7 Mr. James J. Kramer	1 1
NASA John F. Kennedy Space Center Kennedy Space Center, Florida 32899 Attention: Code ATS-132	1
NASA Michoud Assembly Facility P. O. Box 26078 New Orleans, Louisiana 70126 Attention: Mr. Henry Quintin, Code I-Mich-D	1
National Aeronautics and Space Administration Washington, D. C. 20546 Attention: Library, Code USS-10 Mr. Robert W. Ziem, Code RPS Mr. William Cohen, Code RPM	1 5 1
Chemical Propulsion Information Agency Applied Physics Laboratory 8621 Georgia Avenue Silver Spring, Maryland 20910	1
U. S. Naval Postgraduate School Department of Aeronautics Monterey, California 93940 Attention: Dr. Roy E. Reichenback	1
NASA Scientific and Technical Information Facility P. O. Box 33 College Park, Maryland 20740	58 plus reproducible